Fall 12-17-2022

ORBITAL ANGULAR MOMENTUM ORTHOGONALITY-BASED CROSSTALK REDUCTION: THEORY AND EXPERIMENT

Unaiza Tariq
utk1187@gmail.com

ORBITAL ANGULAR MOMENTUM ORTHOGONALITY-BASED CROSSTALK REDUCTION: THEORY AND EXPERIMENT

Approved by:

_____
Prof. Duncan L. MacFarlane
Professor of Electrical Engineering

_____
Prof. Dinesh Rajan
Professor of Electrical Engineering

_____
Prof. Gary Evans
Professor of Electrical Engineering

_____
Prof. Prasanna V Rangarajan
Assistant Professor of Electrical Engineering

_____
Prof. Rashaunda Henderson
Professor of Electrical Engineering

ORBITAL ANGULAR MOMENTUM ORTHOGONALITY-BASED CROSSTALK REDUCTION

A Dissertation Presented to the Graduate Faculty of the

Bobby B. Lyle School of Engineering

Southern Methodist University

in

Partial Fulfillment of the Requirements

for the degree of

Doctor of Philosophy

with a

Major in Electrical Engineering

by

Unaiza Tariq

BEE, Air University
MS Electrical Engineering, University of Texas at Dalas

December 17, 2022

ACKNOWLEDGMENTS

Doctoral research has been the most challenging and demanding journey for me. But my load has been lightened, and my ambitions have been encouraged by the support of many people.

This work could not have been possible without the wise guidance and continuous support of my PhD advisor and mentor Dr. Duncan Macfarlane. I would like to thank him for giving me the opportunity to begin this research, and the encouragement to continue. In all these years of working with him and learning from him, he has been highly supportive and considerate. He has known exactly when I needed a little push, or a kind word. He taught me that my PhD was not just about what I accomplish but about what I learn. He instilled in me the importance of good presentation and writing skills. I have thoroughly benefited from his diverse knowledge in the fields of electromagnetics, photonics, and signal processing, as well as his keen vision for future. I am deeply grateful for his invaluable support and advice.

I am indebted to my committee members Dr. Dinesh Rajan, Dr. Gary Evans, Dr. Prasanna V Rangarajan, and Dr. Rashaunda Henderson for taking out the time to be a part of my committee, and for providing me valuable advice regarding the project. I am particularly grateful to Dr. Rashaunda Henderson for sharing her knowledge and providing valuable guidance in this research.

I would take this opportunity to thank Dr. Solyman Ashrafi who was a champion of some of the geometries included in this work. His advice and insight was highly valuable in this research.

My sincere thanks goes out to my colleague Hiva Shahoei, who always made time to help and support me. She has been a valuable friend and teacher, who has always been ready to answer my questions. It has been a pleasure working with her.

For the various parts of this project, I have had to work in several labs and use different equipment. To the people in charge of these labs, I owe a debt of gratitude. Scot MacWilliams trained me in the use of the ProtoMat S103 board plotter for the fabrication of my antenna, in the biotechnology lab at Junkins. I am also thankful to Guang Yang for his help in taking measurements in the antenna chamber.

I welcome this opportunity to thank the friends and family who provided me the support and encouragement to undertake this journey. I will always be grateful to my parents who allowed and encouraged me to dream from a young age. Who supported me morally, physically and financially to achieve my dreams. I am also thankful to my grandparents for their continuous prayers, specially to my nana who was always interested in my studies and my plans. I would like to thank my niece Izzah Fatima, for her help during my PhD years, to Sarah Hummayun for proofreading my dissertation report, and my brother Muneeb Khawaja for helping me with the figures. I am grateful to my sister Mubashira Tariq, who shared with me knowledge that she had gained in her own PhD journey. And to my son who has seen me studying ever since he was born, and who has practically grown up on campus. I appreciate his patience while I have worked, and I hope to be an inspiration for him some day.

Last but not the least, my warmest thanks is due to my husband, without whom this work would not have been possible. I am thankful to him for his endless support, and for his help when I needed it. From helping me buy wood for my antenna stands to setting up the antennas in the chamber, to waiting for me outside campus whenever I needed, he has indeed been of immense help.

Tariq, Unaiza
B.E.E., Electrical Engineering, Air University, Pakistan
M.S., Electrical Engineering, University of Texas at Dallas

Orbital Angular Momentum Orthogonality based Crosstalk Reduction

Advisor: Professor Duncan L. Macfarlane
Doctor of Philosophy conferred December 17, 2022
Dissertation completed November 15, 2022

Full duplex communication systems allow a single channel to be used for simultaneous two-way communication, increasing spectral efficiency. However, full duplex communication systems suffer from the issue of self-interference between local transmitter and receiver antennas. Analog subtraction and signal processing methods have previously been used to reduce this problem. This dissertation proposes the use of waves carrying orbital angular momentum (OAM) to mitigate the problem of self-interference by offering a means of additional isolation between local antennas.

Orbital angular momentum has been widely studied both in the photonics and radio domain. The theoretically infinite orthogonal states of an OAM signal make it highly desirable in the field of communication. The application of OAM in a full duplex system, may be the answer to the problem of self-interference. This dissertation shows how the use of OAM waves may create an additional isolation between local antennas in a full duplex system. Motivated by the promise that OAM orthogonality holds, this dissertation explores the crosstalk reduction achieved through OAM. One of the main contributions of this dissertation is to provide insight into the nature of the effect. It motivates OAM orthogonality as a direction of research for use in future full duplex systems.

The effect of OAM on crosstalk must be studied experimentally and theoretically. To this effect, a patch array antenna was designed using the High Frequency Simulation

Software (HFSS), to generate OAM beams. The designed antennas are fabricated and characterized. This dissertation discusses the experiments carried out to determine the amount of crosstalk reduction achieved due to the OAM nature of the signal transmitted. The impact of the change in distance between the local transmitter and receiver antennas on crosstalk is also studied. The results obtained are verified through theoretical analysis using simulations in HFSS. This dissertation reports a maximum theoretical crosstalk reduction of 3.6dB, and a crosstalk reduction of 2.6 dB realized experimentally.

Building on these results, a compact, more practical antenna configuration was designed. This nested design yields more than 60dB crosstalk reduction and provides for a more elegant system realization. The dissertation includes the design of a parabolic dish antenna to build a complete system, which is also studied in this dissertation.

The symmetry of the nested antenna configuration allows for analytic theoretical study which is included herein. The study mathematically proves the orthogonality of OAM modes, and the isolation between two antennas with different OAM modes. A similar study is simulated in HFSS using coaxial based loop antennas, and the crosstalk in the nested design is investigated. The design offers a crosstalk isolation of more than 90dB, and further affirms the mathematical analysis.

This dissertation provides a detailed analysis of the isolation offered by OAM orthogonality in local antennas which can be useful in a full duplex system. The work consists of practical, simulated, and mathematical investigation, and considers various antenna configurations and designs. Additionally, it presents and analyses a design for a full duplex system.

TABLE OF CONTENTS

LIST OF FIGURES

For my children,

Harris and Hannah,

so that they know that

hard work and persistence pays off,

prayers get answered,

and dreams do come true.

Chapter 1

INTRODUCTION

Full duplex communication in wireless networks necessitates the transmitter and receiver working simultaneously at the same frequency. The use of a common channel for both transmission and reception increases the spectral efficiency. The main challenge in such a system is that the crosstalk from the local transmitter at one node may be much stronger than the signal emanating from a distant transmitter at a different node. This is called self-interference, and this crosstalk makes it impossible for information to be decoded from the received signal. For a full duplex communication system with a transmitter power of 65dBm [1], and a receiver with a noise floor of -120dB, more than 185 dB of self-interference must be cancelled out. If the interference is not completely negated, it must be ensured that the crosstalk signal is lower than the signal coming from the distant transmitter. This chapter describes the various techniques currently employed to lower the crosstalk signal, and then discusses in more detail how orbital angular angular momentum (Orbital Angular Momentum) can be used to create isolation between antennas in near proximity. The properties, methods of generaion, and advantages and disadvantages of OAM will also be detailed herein. This dissertation focuses on the use of OAM ortogonality to reduce crosstalk between local transmitter and receiver antennas, and through experimentation, simulations and mathematical analysis describes the amount of isolation between the antennas that can be achieved using this method.

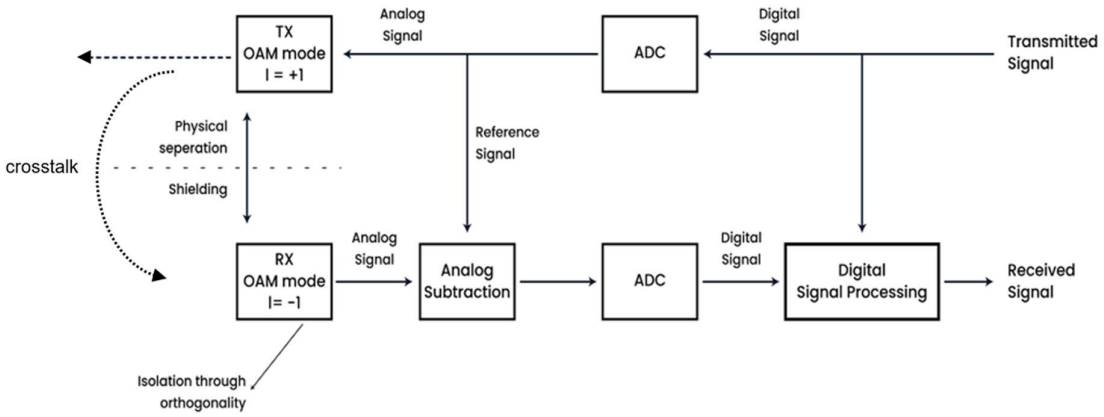

Figure 1.1 Techniques used to reduce crosstalk signal from local transmitter.

1.1 Crosstalk Cancellation Techniques

A digital signal is encoded into an analog signal, which is radiated by the transmitter antenna. Conversely, the analog signal captured by the receiver antenna is converted to digital form. Therefore, there can be three different stages at which the crosstalk signal may be canceled out, at the RF level, while the signal is in analog form, or while it is in digital form. Several techniques have previously been proposed and implemented to cancel or reduce crosstalk. These can generally be divided into 4 categories: (a) digital signal processing, (b) analog cancellation, (c) physical crosstalk reduction through shielding, and (d) orthogonality. The methods, and the various stages at which they apply, are illustrated in fig. 1.1. The first method acts on the digital form of the signal. The second category reduces crosstalk in the analog form of the signal. The last two methods use the antennas to cancel out crosstalk at the radio level.

1.1.1 Digital Cancelation

There are several techniques for digital cancelation [2]–[7] in full duplex and other systems. The most basic form of cancelation through digital signal processing involves subtracting the transmitted signal from the signal received by the local receiver. At the receiver end, both crosstalk and the signal from a distant transmitter are captured by the receiver antenna. This signal is in the analog form and is converted to digital form by an analog-to-digital converter (ADC). If the crosstalk signal is high, it may saturate the ADC, and the signal of interest may be lost in the process. The digital form of the transmitting signal is then subtracted from this digital form of the received signal. However, since this subtraction occurs after the digital conversion of the received signal, the weaker signal of interest may have already been lost before the subtraction of transmit signal occurs. This method alone is, therefore, insufficient for the cancelation of crosstalk. In reference [2] an isolation of 10dB was achieved using digital cancelation only, however many variations of digital cancelation exist, with different levels of isolation.

Analog Cancelation

Analog cancellation involves subtracting the radio's own transmitted signal from the receiver signal before it is converted to digital form. The transmitter signal, before it is digitized by the ADC, is taken as the reference signal. The reference signal is used by a vector modulator, which varies the amplitude and phase of the reference signal to model the effects of the transmission channel between the transmitter and receiver. The resulting signal can be used to cancel the crosstalk from the received signal. Several methods [2], [8], [9] can be used to alter the reference interference signal, and various noise cancelation chips/circuits can be used to perform this process. Varying levels of isolation are achieved by using different

analog cancelation methods, for example 30dB crosstalk reduction is seen in [10]. The details of these methods, however, are beyond the scope of this dissertation report.

Physical Crosstalk Reduction

Passive suppression is a method that significantly reduces crosstalk. This method uses the physical placement and orientation of the transmitting and receiving antennas to create isolation between them. Several factors can come into play, in this regard: the actual distance between the antennas [11]–[13] , directivity and direction of the antennas [12], [14]–[16], and absorptive shielding [17]. A similar method involves using multiple transmitter antennas at various distances such that their signals cancel out the crosstalk signal of the original transmitter antenna [2], [18]–[21]. Crosstalk suppression or cancelation using these methods occurs at the electromagnetic level. The problem is that it is not always feasible to use these methods due to the constraints imposed by the size of the antenna system, the directivity requirements of the antennas, and the accuracy of the antenna positions.

Orthogonality

Signals with a dot product of zero are considered orthogonal signals. These include sine cosine signals, even and odd signals, and signals with orthogonal polarizations, such as horizontally and vertically polarized signals. Orthogonal signals do not ideally interfere with each other. If orthogonal signals are used for transmission and reception, this would naturally create an isolation between the local transmitter and receiver antennas. Due to the advantages it conveys, the concept of orthogonality has long been used in communication design. For instance, orthogonality has been extensively used in multiplexing. Quadrature Amplitude Modulation (QAM), Phase Shift Keying (PSK), and Code Division Multiple Access (CDMA) are just some of the systems that rely on orthogonality. In full duplex applications, orthogonality is often achieved by way of polarization [22]–[28]. Although polarization

provides the means for interference cancelation, there can be only two orthogonal states, therefore it cannot provide isolation among multiple antennas. Moreover, the isolation obtained through this method is dependent on the purity of the antenna polarization. This cancelation scheme thus does not work well with array antennas which are common [29].

Waves carrying orbital angular momentum (OAM) can have multiple orthogonal states. Although the application of OAM orthogonality in communication has been extensively studied [30]–[36], most of the previous studies focus on achieving isolation between different modes for the purpose of multiplexing [30]–[36]. Few studies [37], [38] have explored the application of OAM in full duplex systems, and there has not been enough research on OAM orthogonality-based isolation between the local transmitter and receiver in a full duplex system. Reference [29] investigates the isolation between a transmitter and receiver created by using a sequentially rotated array of microstrip antennas to generate OAM. However, the isolation achieved in this case is not based purely on OAM, but is dependent on the sequentially rotated scheme. This dissertation performs a detailed investigation of the amount of isolation achieved as a result of the OAM nature of the signal transmitted between local transmitter and receiver antennas.

1.2 Orbital Angular Momentum (OAM)

A plane wave features a simple Poynting vector in the direction of propagation. Maxwell's theory asserts that electromagnetic radiation not only carries energy, but also momentum, and this momentum is also dependent on the Poynting vector. Changes in the Poynting vector **S** across the lateral extent of the wave gives rise to different types of momentum. In a plane wave, **S** is constant across the entire wavefront and it carries with it a constant momentum. A manifestation of this momentum is photon pressure. If the wavefront is curved, the momentum and hence photon pressure varies across the curvature of the phase-front because of the Poynting vector. OAM waves—with Poynting vectors that wrap around

themselves—are donut-shaped. These donut modes are extensions of Laguerre Gaussian modes, which is a formal solution of Maxwell's wave equations in cylindrical coordinates. However, the Laguerre Gaussian modes are only one example of waves that have orbital angular momentum [39]–[41]. There are other types of waves that carry OAM to some extent, such as the Bessel beams[42]. And not all donut-shaped modes carry orbital angular momentum [43], [44].

Angular momentum can be divided into two types, spin momentum and orbital momentum. Spin momentum determines polarization, whereas orbital angular momentum is associated with spatial distribution [39]. In 1992, Allen et al. showed that Laguerre Gaussian beams with an azimuthal phase dependence of $e^{jl\varphi}$ carry orbital angular momentum (OAM) [39], [45], where l is a positive or negative integer and φ is the angular coordinate. These waves may have multiple helical phasefronts, the number and direction of which is determined by the mode number l. Since the Poynting vector is normal to the phasefronts, the helical shape of the phasefronts results in an azimuthal component of the Poynting vector, and therefore an angular momentum can be said to exist.

The characteristics, properties, methods of generation, and applications of OAM waves have been extensively studied over the last three decades [45]–[54]. Although spin momentum can provide only two orthogonal polarization states, orbital momentum has the potential to provide a theoretically infinite number of orthogonal states. In terms of practical applications, up to 86 OAM modes with a high mode quality have been generated [55] in the optical domain. The property of inter-mode orthogonality makes OAM waves highly attractive to the field of electronic communication. Although much of the research on OAM was initially focused on the optical domain, there has also been significant amount of studies dedicated to examining radio OAM waves, and their applications in communication and

astronomy [45]. OAM radio waves are of special interest in radio communication links, as their orthogonality suggests a novel multiplexing scheme [34], [39], [56], [57].

1.3 OAM Waves in Radio Communication

The idea of exploiting OAM orthogonality in radio communication is not new. Countless published studies provide experimental evidence showing that more than one OAM mode can be successfully transmitted on the same frequency channel. In [56], Tamburini carried out an outdoor experiment to show that information transmitted using waves of the same frequency, with the OAM modes l=0, l=-1 and l=+1, was successfully received in the far field. Others, such as [29], have used OAM orthogonality in conjunction with polarization to create independent multiplexed channels. In [58], OAM multiplexing is combined with spatial multiplexing to increase system capacity.

Spectral efficiency is not the only advantage of implementing OAM in wireless communication, though. The following are among the three main advantages of OAM-based wireless communication :

1. Spectral efficiency. Since the orthogonality of the channels is based on the OAM modes, other resources, such as frequency, time ,and code domain, are conserved[59].
2. Greater user access. Traditionally, the power domain is used to distinguish multiple users. Utilizing OAM orthogonality mode division multiple access (MDMA) allows different users to access a wireless network [59], [60].
3. Anti-jamming. OAM-mode hopping might be the answer to the limitations faced by frequency-hopping techniques used in anti-jamming [59].

However, since the use of OAM in communication is still being researched, various challenges in this area nonetheless remain. Some disadvantages of the use of OAM are listed below:

1. Alignment between the transmitter and receiver. The application of OAM in line-of-sight communication requires careful alignment of the transmitter and receiver antennas [61].
2. The signal may undergo fading over the distance of propagation.
3. The divergence of an OAM signal as it travels a certain distance results in the signal at the receiver being much larger than its size when first transmitted. This requires the receiver antenna to be physically larger, which is not practical

1.4 Radio OAM wave Generation

There are several methods for generating OAM waves [57], [62]–[65]. Some of the methods for OAM radio wave generation include Spiral Phase Plate (SPP) antenna and Uniform Circular Array (UCA) antenna.

Spiral Phase Plate (SPP)

A spiral phase plate (SPP) is a dielectric plate with a height that varies in the azimuthal direction around the central axis of the plate, creating a spiral shape as shown in fig. 1.2.

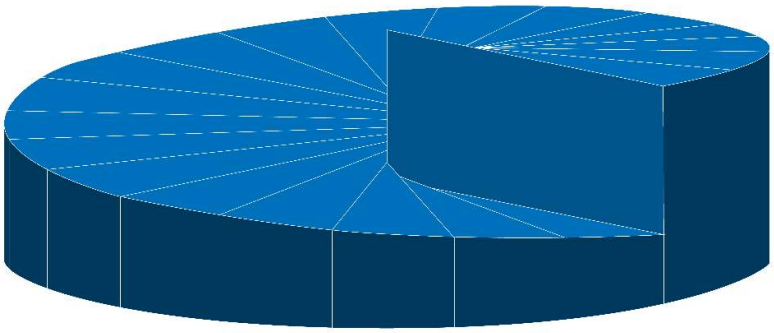

Figure 1.2 Spiral Phase Plate (SPP) used for OAM signal generation. The height of the dielectric changes along the azimuthal angle.

The height may increase over a finite number of equidistant steps. The variation in height causes a difference in phase-shifts between the signal passing through the thicker medium and that which passes through the thinner part of the dielectric. The velocity of a signal in air is given by the speed of light *c,* whereas the velocity in the dielectric is *c*/n, where n is the refractive index of the dielectric material. The phase-shift in the signal propagating a distance h through air, measured in radians, is given by

$$phase\ shift = \frac{2\pi}{\lambda_o} h$$

In this context, λ_o is the wavelength of the signal in air. The phase-shift through the dielectric of height h is given by the expression below, where λ_o/n is the wavelength of the signal in the dielectric medium:

$$phase\ shift = \frac{2\pi}{\lambda_o/n} h$$

Therefore, the difference in the total phase-shift as the height of the phase plate increases from 0 to 2π is given by $\frac{2\pi}{\lambda_o}(n-1)h$ radians.

As the planar wavefronts interacts with the plate of varying thickness, different parts of the wave experience different phase-shifts, resulting in a helical shape that is in accordance with the shape of the spiral phase plate. The emerging signal, therefore, has a component of angular momentum in the azimuthal direction by virtue of its helical wave shape, and is said to carry orbital angular momentum. The phase plate is designed such that over a complete rotation of the azimuthal angle φ, the maximum phase-shift in the signal is $2\pi l$, where l is defined as the mode number of the resulting OAM signal.

Other similar methods for transferring orbital angular momentum to plane waves involve amplitude encoded fork holograms, such as those used in optics. The radiation generated by

this antenna features low divergence, but high attenuation. However, it does not work for low frequencies, and cannot be used for simultaneous multi-mode generation [58], [59].

The spiral phase plate method has been used as a means of OAM generation in a number of works[49], [66]–[68]. Members of our group have previously used a structured phase plate to generate Hermite Gaussian radio waves, which are also in the orthogonal family of waves [69] and Ince-gaussian modes[70]. Similarly, a stepped spiral phase plate was used to generate OAM in the Terahertz region [67].

Uniform Circular Array (UCA)

Similar to the spiral phase plate, a uniform circular array (UCA) can create a phase difference in the signal along the azimuthal direction. However, in this case, the signal is generated at a different phase by antennas arranged in a circular array. In other words, in this case, the phase-shift of the radiated wave in the azimuth direction occurs because of the phase-shift in the signal feeding each antenna of the array. The phase delay between the signal feeding each adjacent antenna element is given by $2\pi l/N$, where l is the mode number and N is the number of array elements. The radiation from each antenna element combine to create the twisted phasefront of an OAM beam. Because of the phase shift between the signal feeding each antenna element, the uniform circular array can also be called a phased array antenna. The elements of a UCA may be dipoles or patch antennas. This method is low cost and easy to fabricate, and for this reason, it has been widely been used in various studies [48], [71]–[75]. However, a major problem with this approach is the high divergence of the beam generated [59], [76].

Loop Antennas

The concept of loop antennas can be designed to be similar to a spiral phase plate and phased arrays. It creates a phase difference in the signal in the azimuthal direction, resulting in

radiation with helical wavefronts. The signal is passed through a loop antenna, which may be a metal ring cavity as in [77] or a coaxial waveguide as in [78], using a traveling wave current excitation, such that the amplitude of the signal remains constant around the loop, but the phase changes with the azimuth angle to $l\varphi$, where l is the OAM mode. Therefore, for every one revolution around the loop, the signal makes l 2π phase- shifts. In general, slots are cut in the loop antenna to allow the radiation to emanate outwards. This method is easy to realize, and analyze. However, the OAM beams generated also have high divergence, which must be taken into account in a system design.

There may be other methods for OAM generation. However, the concept common to all methods is the introduction of a phase difference across the signal, in the azimuth direction, either before the signal is transmitted (as in phased arrays) or after (as in spiral phase plates). The choice of the method used depends on the application it is to be used for, and requirements such as ease of fabrication, flexibility etc.

1.5 Outline

This dissertation presents the orthogonality of different OAM modes as a method for increasing the isolation between antennas in near proximity. This is especially useful for mitigating the self-interference or crosstalk that occurs in full duplex systems. The rest of this dissertation examines in greater depth the antennas used and the experiment design required to determine the effect of OAM on crosstalk reduction.

Chapter 2 explores the design of an OAM antenna using phased arrays. It discusses the design and fabrication process, and the theoretical and practical characterization of the antenna. Chapter 3 describes the experimental setup and procedure needed to determine the differential crosstalk reduction due to OAM. It also presents the results of an experiment. To verify the results theoretically, the modeling is carried out using HFSS, as described in

chapter 4. Chapter 5 describes a practical and compact topology for antenna placement, one that involves constructing the transmitter and receiver antennas in a nested setup on the same substrate. A detailed theoretical analysis to determine the isolation between the antennas in this nested configuration is described within this chapter, as well. Chapter 6 is divided into two sections. The first section provides a mathematical derivation of the voltage induced in a receiver OAM antenna due to crosstalk, in the nested antenna design. The second section analyzes the nested antenna setup created using loop antennas in HFSS—which models the antennas using loops of wire—as a way to verify the mathematical derivation of crosstalk-induced voltage.

1.6 Contributions

The purpose of this dissertation is to determine the crosstalk reduction that takes place between antennas in near proximity by way of OAM waves. The major contributions of this dissertation are:

- It explores the effect of OAM orthogonality on crosstalk between antennas in near proximity and provides a deeper understanding of the nature of this effect.
- It introduces techniques developed to filter out deterministic numerical noise, inherently present in calculations made by HFSS.
- It promotes the development of a compact nested design, and offers a theoretical model for understanding how best to achieve crosstalk reduction in nested antennas.

1.6.1 Effect of OAM on Differential Crosstalk

This work's first contribution pertains to the experimental study of isolation created by leveraging the OAM orthogonality. OAM modes l=+1 and l=-1 were used for the study. The OAM antennas were placed adjacent to each other. The experiment also studied the variation of isolation in relation to distance. The trend shown by the isolation with variation in distance

is, in fact, one of the biggest contributions of this research. The sinusoidal behavior of differential crosstalk gives insight into the nature of the effect. Such a study has not been conducted before.

This dissertation introduces the term *differential crosstalk*, to refer to the difference in crosstalk between two different cases. This ensures that only the effect of the parameter under study is calculated, and the effect of all other factors are cancelled out. Since the parameter of interest in this work is OAM mode, the crosstalk was calculated with a mode for the receiver antenna of l=+1, and then with a mode of l=-1. The difference in crosstalk between the two cases was calculated to obtain the differential crosstalk ΔS_{12}. In performing the subtraction between the two crosstalk values, the effect of all other unchanged factors is cancelled out. These factors include the distance between the two antennas, the direction of the antennas, the shielding between antennas, etc. Therefore, differential crosstalk provides the change in crosstalk value that is exclusively attributable to the OAM nature of the antennas.

1.6.2 Crosstalk Calculations through Simulations

To verify the experimental results, the setup was also simulated using the popular RF design program, High Frequency Simulation Software (HFSS). The experimental procedure was repeated using simulated antennas, and the theoretical results were therein obtained. More importantly, it was seen that due to the degree of precision of HFSS, the theoretical results obtained carried an inherently high deterministic numerical noise. Since the received signal readings were low values, the addition of this noise caused useful information to be lost. To overcome this problem, a moving average filter was used for the first time, to filter out the noise from the data. The resulting signal demonstrates good agreement with the experimental data. This is an important step in the process of determining differential crosstalk between two antennas through simulation. What is more is that the techniques described in this

dissertation for obtaining theoretical crosstalk values may be generally applied to other antennas, and are not restricted to OAM antennas.

1.6.3 Crosstalk Reduction in Nested Antennas

The promising results of the experiment and its agreement with theory, encourage us to look at other antenna configurations for improved OAM-based isolation. One such setup has been analyzed theoretically in this dissertation. Nested antennas are designed for the realization of a more compact and practical implementation of full duplex systems, by accommodating both antennas within the same space. This dissertation provides a detailed theoretical analysis of the crosstalk reduction that occurs due to OAM, between local antennas in such a setup. This is an important step towards the practical realization of OAM-based isolation in full duplex systems, as it provides a realistic design for transmitter and receiver antennas placement in such a system.

The setup consists of OAM antennas placed concentrically. The mode of the inner antenna is fixed at +1, whereas the mode of the outer OAM antenna is varied. A high OAM-based isolation was achieved through this antenna placement. It was noted that a higher isolation is provided by even OAM modes, compared to odd modes, which suggests a higher orthogonality between even-odd pairs. Chapter 5 details the complete design of a practical full duplex system, using ray matrices and HFSS simulations. To mitigate the problem of OAM beam divergence, a single parabolic dish antenna at each end of the system is employed to collimate the signal. Chapter 5 also provides the link budget calculation of an example of a system based on nested antennas.

This dissertation report provides mathematical proof of the isolation between local OAM antennas with different OAM modes in a nested design by deriving the voltage induced in the outer loop antenna as a result of the field generated by the inner antenna. This

derivation is further verified by the HFSS analysis of a nested design created using loop antennas. Findings from the simulation also allow for a comparison between the nested design using phased arrays and one that uses loop antennas. In this way, through practical, simulated and mathematical investigations, this dissertation serves as a detailed study of the crosstalk between local OAM antennas.

Chapter 2

OAM ANTENNA DESIGN, FABRICATION AND ANALYSIS

Although there are several methods for OAM generation in the radio domain [57], [62]–[65], the method employed in this work uses phased array antennas. A phased array antenna consists of an array of single antenna elements. The array changes the shape of the radiation pattern or steers the beam electronically by providing different phase shifts to each element of the array. In this research, rectangular patch antennas are used as the elements of the phased array. The rectangular patch antenna is a well-studied and easy to build antenna. Therefore, it proved to be a good choice to use in these experiments. The antenna construction is comprised of two parts; theoretical antenna design using calculations and HFSS, and practical antenna fabrication. The OAM antenna was tested both theoretically and practically.

2.1 Rectangular patch antenna

Microstrip antennas or patch antennas are easy to fabricate, are low cost and are highly versatile. Therefore, they are widely used, and are well studied. A patch antenna consists of a high conductivity metal patch and ground plane separated by a dielectric material called the substrate. The substrate has a relative dielectric constant ε_r and thickness h which is much smaller than the wavelength. The metal patch has a length L and a width W as shown in fig. 2.1, where L is the dimension of the longer side.

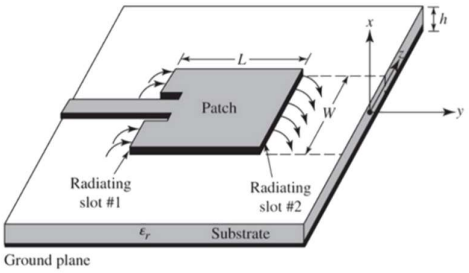

Figure 2.1 The rectangular patch antenna[78]

The most popular methods [79]–[87] (fig. 2.2) for feeding the patch are the microstrip line, and coaxial probe. Other methods include aperture coupling, and proximity coupling. The microstrip line method consists of a thin metal strip on a substrate and ground, feeding the patch. The impedance of the strip can easily be matched with the antenna impedance by creating an inset around the strip where it meets the patch. This method is easy to construct, but has a limited bandwidth, and there may be unwanted radiation from the strip. The probe feed method uses a coaxial transmission line feeding the patch from either below the ground (as shown in fig. 6.2), or from the edge of the patch, also called edge feed method. The edge feed design is easy to fabricate, does not have unwanted radiation from the coaxial probe, and easy to ensure impedance matching, but it also has a narrow bandwidth. The aperture coupling method consists of two substrates separated by a ground plane. There is a microstrip line at the bottom of the lower substrate, and a metal patch on top of the upper substrate. The signal from the stripline is coupled into the patch through a slot in the ground. However, this method is difficult and more expensive to fabricate and also has a narrow bandwidth. Similarly, the proximity coupled method also uses coupling between the stripline and the patch which are not in direct contact. This method has the largest bandwidth but because of the precision involved, is difficult to fabricate.

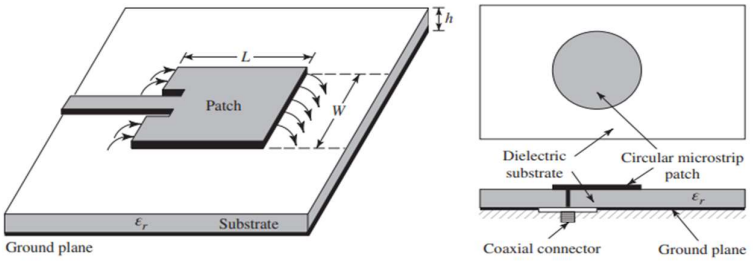

Figure 2.2 Commonly used feeding methods for patch antennas: microstrip line feed (left) probe feed (right) [22]

The frequency of operation of the patch antenna, and its impedance matching with the feed is determined by the patch dimensions. Considering the patch antenna as a transmission line, the edge of the patch acts as an open circuit since the current does not have a path to flow. Therefore, the current is zero at the edges and maximum at the center of the patch. The voltage, which is 90° shifted from the current, is maximum at the far end, and minimum at the other end of the patch. This means that positive charges are accumulated at one end of the patch and negative at the other, resulting in a flow of electric field lines between the patch and the ground, as shown in fig. 2.3. Some of the radiation escapes into the air causing a fringing effect at the edges of the patch, as depicted in the figure. The fringing electric fields add in phase, causing the antenna to radiate. The amount of fringing is a function of the patch dimensions and the height of the substrate. The permittivity of a material is its ability to concentrate electric field lines through it. A substrate with a higher permittivity would tend to focus the field lines through it, and less field lines would go through a substrate with a lower permittivity. The lower the permittivity of the substrate, the more the field would tend to escape into the air, which causes fringing in the case of a patch antenna. .

The fringing effect causes the electrical length of the patch to appear effectively greater than the physical length, as shown in fig. 2.3. This in turn affects the resonance frequency of the patch. The effective length is denoted here by L_{eff}, and the resulting resonance frequency is denoted by f_{rc}. Moreover, since the field lines travel through both air and substrate as shown in fig. 2.3, it is not correct to use the dielectric constant of the substrate only. Therefore, the term effective dielectric constant ε_{reff} is introduced, to include the effect of the permittivity of both the air and the substrate. It is the effective dielectric constant that governs the amount of fringing, the dielectric constant of the substrate, and the height of the substrate[79].

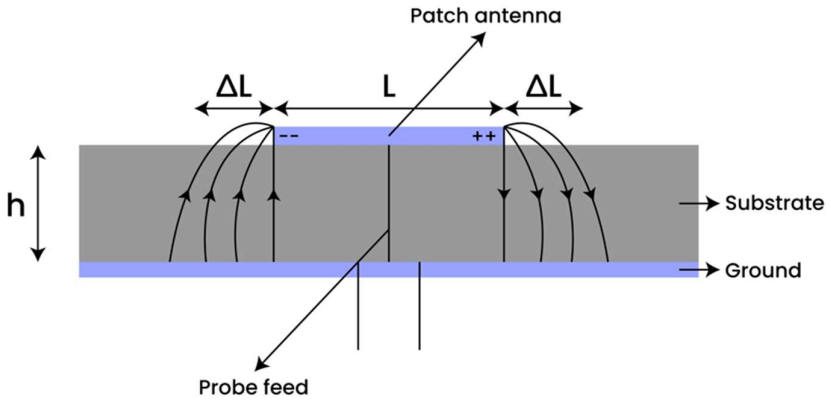

Figure 2.3 The fringing effect of electric field lines as they travel from the patch to the ground causes radiation. The effective length of patch is greater than its physical length

The design process of the patch antenna consists of calculating the patch dimensions to provide the desired resonance frequency f_r. The width W, of the patch is tuned to get the desired impedance of the antenna. It is given by [79]

$$W = \frac{v_o}{2f_r}\sqrt{\frac{2}{\varepsilon_r + 1}} \qquad (1)$$

Where v_o is the speed of light in free space, and ε_r is the relative permittivity or dielectric constant of the substrate.

From fig. 2.3, the effective length of the patch may be written as [79]

$$L_{eff} = L + 2\Delta L \qquad (2)$$

The length of the patch is taken as half of the wavelength of operation. Therefore, the length of the patch is selected to obtain the desired resonance frequency of the patch antenna, and this can be written as [79]

$$f_r = \frac{v_o}{2L\sqrt{\varepsilon_r}} \qquad (3)$$

Considering fringing effect, the equation may be rewritten as [79]

$$f_{rc} = \frac{v_o}{2(L + 2\Delta L)\sqrt{\varepsilon_{reff}}} \qquad (4)$$

Several approximations [79], [88]–[90] have been proposed to determine the values of effective dielectric constant, and effective length. Of these, the most popular was given by Hammerstad in 1975 [90]. The approximation expressions are used to determine the value of effective dielectric constant ε_{reff} , and the extension in length $2\Delta L$. ΔL, along with the desired resonance frequency f_{rc} is used to find the effective length, and therefore the physical length of the patch.

It is important to note that the values calculated through the approximate expressions provide a reliable initial estimate of the patch dimensions. However, further fine tuning is required using a simulation software such as HFSS, to achieve the exact value of the desired

frequency of operation. Increasing the length of the patch decreases the resonance frequency. Increasing the width W of the patch decreases the input impedance.

2.2 Patch antenna array for OAM generation

Fig. 2.4 shows the radiation pattern of a patch antenna. It consists of a single lobe above the patch, and exhibits low back radiation. When multiple patch antennas are used in an array, their radiation patterns add in phase and amplitude, to create a combined radiation. If the signal to each patch is phase shifted, the radiation of the patches may add up constructively in some areas and destructively in others. The phase difference between the patches can be varied to create helical phase fronts, hence generating OAM waves.

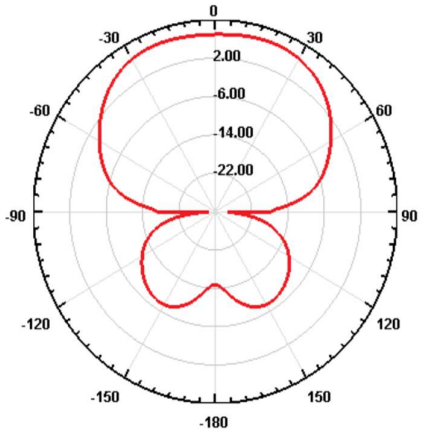

Figure 2.4 The Radiation pattern of a rectangular patch antenna

The concept of phased arrays is not new as it has been numerically explored in previous research[46], [48], [91]–[93] . In [72], Bai et al., for the first time presented a practical method for OAM generation using circular phased arrays at 10GHz. A circular phased arrayThe antenna consists of a circular array of N patch antennas. To generate an OAM wave of mode l, the signal to each patch is phase shifted by $2\pi l/N$ radians from the adjacent patch, such that

there is a total phase change of $2\pi l$ radians in one complete rotation around the array axis [72]. Previous research on the appropriate number of array elements suggests that the number of elements N must satisfy the condition $N > 2|l| + 1$ to avoid under-sampling [57]. Therefore, to generate an OAM beam with mode 1, the number of elements *N* must be greater than 3. The study showed that although a phase singularity is achieved with 4 patches, a well-defined donut shaped OAM with mode 1 is observed using *N*=8, with an inter-element phase difference of π/4 radians [57]. The array used in [72] to generate an OAM mode *l*=-1 at 10 GHz is shown in fig. 2.5. It has been presented here as an example of the phased array based OAM antennas constructed in previous research. It consists of 8 patch antennas with a phase difference of π/4 rad between the feeds, and has been designed using the conditions described above.

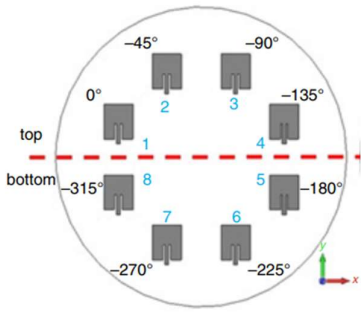

Figure 2.5 Phased array used to generate OAM mode *l*=-1 [72]

2.3 Patch Array Design at 5.64GHz

2.3.1 Single patch antenna

Based on the ideas discussed in the previous section, an OAM antenna was designed to operate at a frequency of 5.64 GHz. This frequency was used, as it is a popular Wi-Fi band and is accessible to the WARP signal processing boards which may be used in any future

studies. WARP boards have also previously been used in crosstalk reduction studies [12], [94].

The ANSYS High Frequency Simulation Software (HFSS) is employed in the design process of the antenna array. A single patch is designed first, to determine the dimensions of the patch that would allow it to resonate at 5.64GHz. Equations (1-7) are first used to estimate the values of the length (L), and width (W) of the patch. For a substrate with dielectric constant ε_r=3.66 and height $h = 0.762mm$, the values of L, W and ε_{reff} calculated mathematically are $L = 13.64mm, W = 17.4mm$, and $\varepsilon_{reff} = 3.41$. The calculated dimensions are used to create a patch antenna in HFSS, and to run a frequency analysis for it.

Fig. 2.6 shows the model of patch antenna in HFSS. The copper patch is placed on a dielectric substrate RO4350B material with dielectric constant $\varepsilon_r = 3.66$. A lumped port with 50 Ω impedance is used to provide the input feed. The length of the patch determines the resonance frequency, whereas changing the width effects the impedance matching, and thereby the value of reflection coefficient. A lower reflection coefficient means the impedance is well matched and the reflections from the input port are less. A reflection coefficient of less than -10dB is generally considered appreciable.

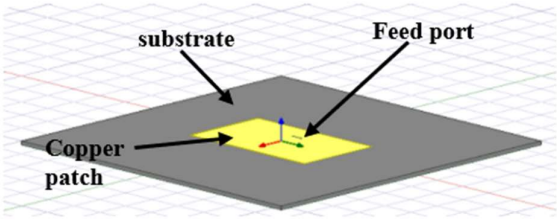

Figure 2.6 Model of a rectangular patch antenna in HFSS

The results obtained for the reflection coefficient of the patch constructed using dimensions calculated mathematically, are plotted in fig. 2.7. A dip in reflection coefficient can be seen at 5.45GHz. This means that the resonance frequency of the antenna is 5.45GHz, instead of the required 5.64GHz. The value of reflection coefficient at this frequency is -11dB. The value of W may be further manipulated to achieve a lower reflection coefficient.

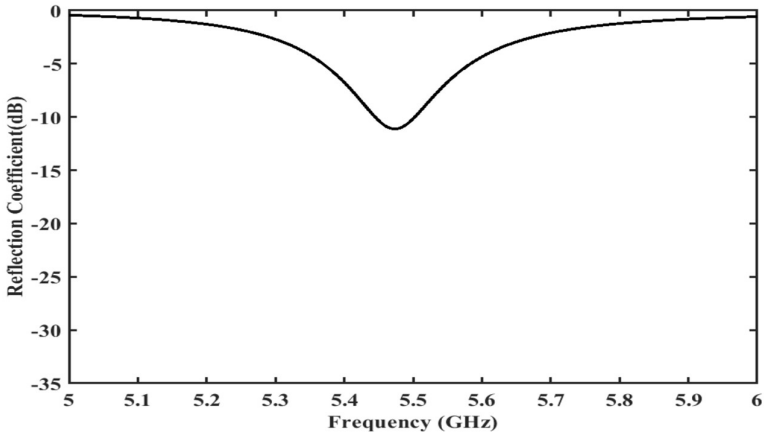

Figure 2.7 Reflection coefficient plot of a single patch antenna constructed using dimensions calculated mathematically

To determine the exact dimensions of L at which the resonance frequency is at the desired value of 5.64GHz, the value of L is varied from 13mm to 14mm in steps of 0.02mm, and the plot of reflection coefficient S_{11} against frequency is observed. By increasing L, the resonating frequency would decrease. The value of L at which the frequency of resonance is 5.64GHz is selected. The value of L is then fixed to the selected value, and the value of W is varied from 17mm to 22mm in a parametric analysis. The plots of S_{11} obtained for each value of W are compared to determine the value of W with the minimum reflection coefficient. Parametric analyses in HFSS, sweeping the length and width of the patch, show that

resonance with minimum reflections, occurs at 5.64 GHz frequency when patch dimensions are L= 13.12mm and W= 22mm. The frequency analysis of the patch antenna with these dimensions, is shown in fig. 2.8. The reflection coefficient of less than -30dB at 5.64GHz shows good impedance matching at this frequency.

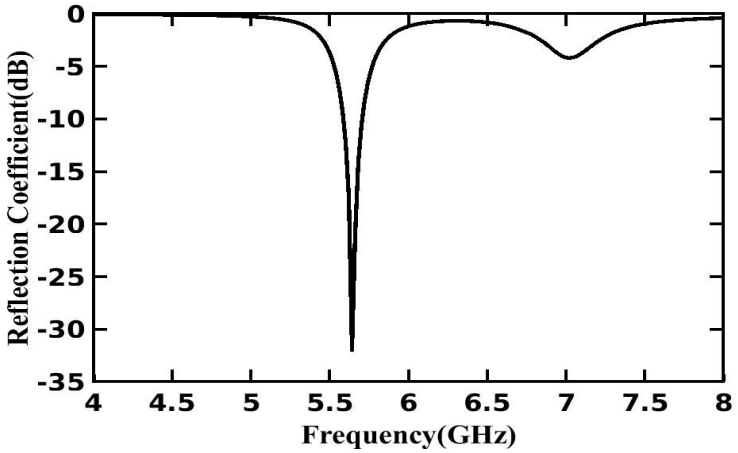

Figure 2.8 Frequency analysis of a single patch antenna

2.3.2 Patch antenna array

The optimized patch dimensions are then used to design a circular array of patch antennas for OAM generation at 5.64 GHz (shown in fig. 2.9). As mentioned in the previous section, N=8 patches generate a well-defined OAM beam of mode 1. Therefore, an array of 8 identical rectangular patch antennas each with a length L of 13.12mm and width W of 22mm, is created. There is a physical angle of 45° between each patch to create a uniform array. There is also a phase shift of 45° between the signal to each adjacent patch, required to generate an OAM mode 1.

The next step is to select the radius of the circular array. A parametric analysis is carried out to determine the optimum value of array radius, by varying the radius of the array from 32mm to 38mm in steps of 2mm, and observing the radiation pattern obtained in each case. The results of the parametric analysis are shown in fig. 2.10. At each array radius, the radiation pattern shows the required null in the center, however each radiation pattern has sidelobes with different gains. A higher gain of the side lobes means more power is being lost. The side lobes are minimum for the arrays with a radius of 32mm, and 34mm. Of these, the radiation pattern for the array with a radius 34mm, has a lower gain at null, and has a more symmetrical OAM shape. Therefore, the optimum radius is 34mm.

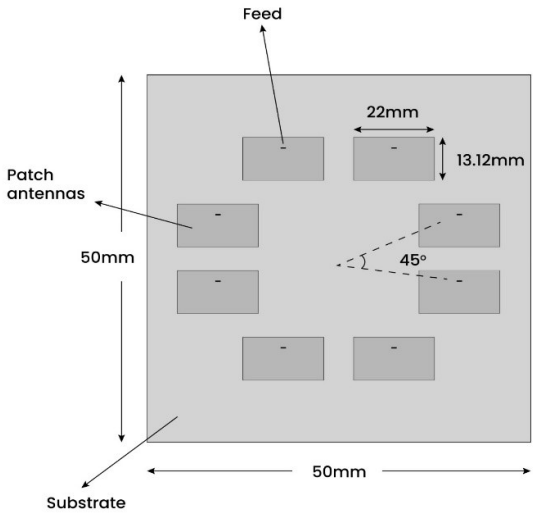

Figure 2.9 The schematic shows the design of the antenna for OAM generation at 5.64GHz. The 45 degrees angle is both the physical measurement, and also the temporal phase measurement difference between patches excitations.

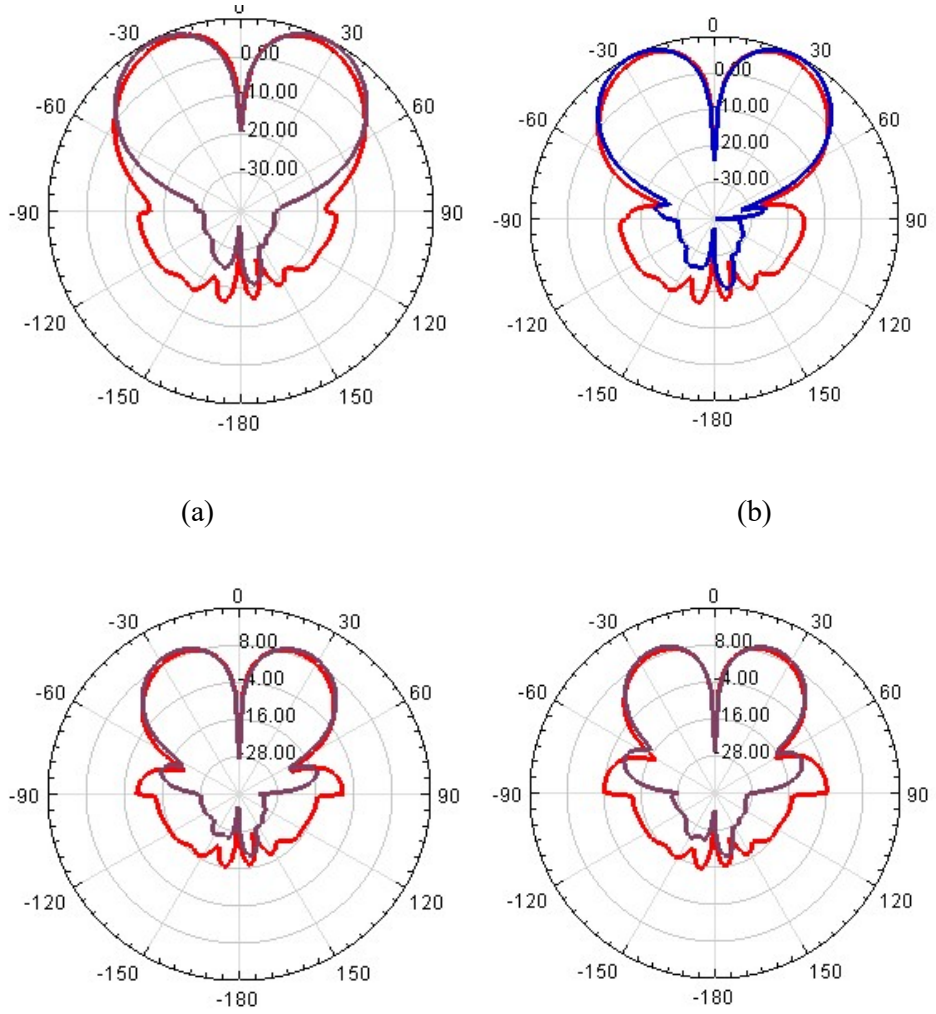

(a) (b)

Figure 2.10 The radiation patterns obtained in HFSS for OAM antennas with array radius (a) 32mm (b) 34mm (c) 36mm (d) 38mm. The radiation patterns are plotted with respect to the angle θ, and are drawn for φ=0(red) and φ=90(purple)

2.3.1 Antenna Characterization in HFSS

The optimized antenna design was simulated and analyzed using ANSYS HFSS. The magnitude of the electric field distribution of the array is calculated and plotted on a rectangular plane 60mm away from the antenna. It is seen to be a donut shape with a null in the center (Fig. 2.11). This null is characteristic of the shape of a field with OAM.

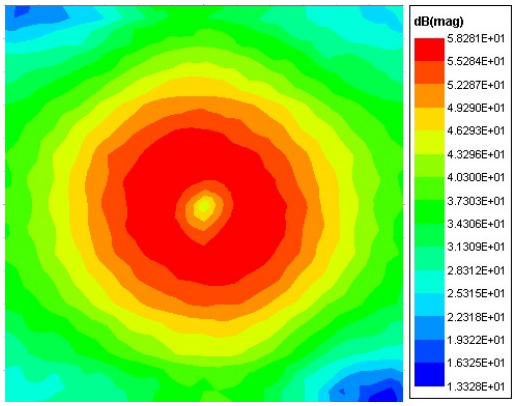

Figure 2.11 Magnitude plot of the electric field of the OAM wave calculated using HFSS, on a plane 60 mm away from the antenna

The radiation pattern calculated by HFSS is plotted in fig. 2.12 for φ=0, and 90 degrees. The radiation pattern confirms a good OAM signal with a marked central null of -22dB. There are minimal side lobes in the radiation pattern. OAM waves are defined by helical phase fronts. Therefore, the characteristic phase pattern of an OAM is a rotating spiral shape. The rotation of the spiral phase front is determined by the OAM mode number and its polarity. The clockwise rotation of the phase of the Electric field, shown in Fig. 2.13 is obtained for OAM mode l=+1. The mode can be changed to l=-l by reversing the direction of the sequence in which phase shifts to the patches increases.

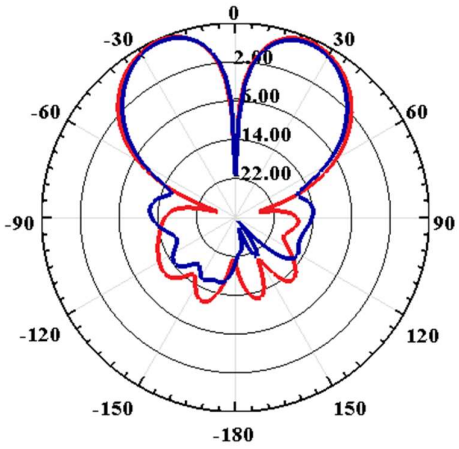

Figure 2.12 The simulated radiation pattern of the OAM antenna is obtained for the planes ϕ=0 and ϕ=90. The red line represents the radiation pattern on the ϕ=0 plane, and the blue line represents the radiation pattern on the ϕ=90 plane

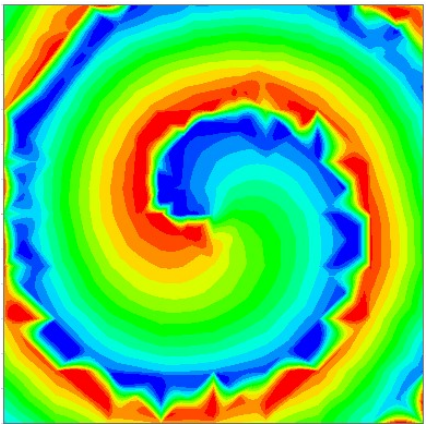

Figure 2.13 Simulated results for the phase pattern of the OAM antenna in the far field. The darkest shade represents 360 degrees and goes down to 0 degrees for the lightest shade blue

2.4 Antenna Fabrication and Assembly

2.4.1 Fabrication

The OAM antenna designed in HFSS was fabricated in lab. The antennas were fabricated on Rogers RO4350B substrate material. The RO4350B has low loss and a low fabrication cost. The RO4350B substrate has a dielectric constant of 3.66, which is suitable for this design. The board has a thickness of 0.762mm, and has a copper layer on the top and bottom sides. The antenna was fabricated using the Lyle school's ProtoMat S103 circuit board plotter. The fabricated antenna is shown in fig. 2.14, and consists of 8 copper patches on top of the substrate, and a copper layer below the substrate to act as ground. SMA connectors are soldered at the back of the board to connect input supply to each patch.

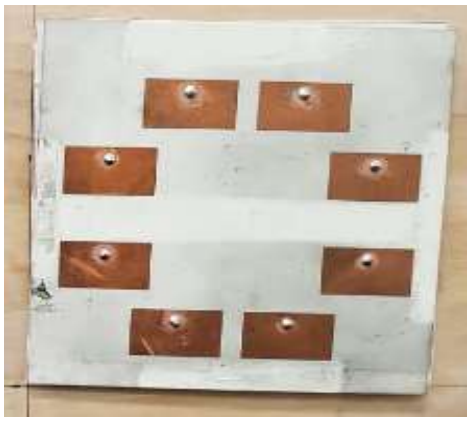

Figure 2.14 The patch antenna array fabricated for OAM generation. 8 copper patches can be seen on the substrate

2.4.2 Antenna Assembly

The antenna designed and fabricated is a uniform circular array. For it to generate helical wave fronts it must be phased. For N=8, the signal to each patch must be phase shifted by $\pi/4$ to generate mode l=1. A feeding network was constructed for this purpose. The transmitter network was assembled as shown in the block diagram of fig. 2.15. The signal

was provided by the RF out pin of the network analyzer, amplified and then split by a power divider into 8 signals with equal amplitude and phase. Each of these 8 signals were used to feed the 8 patches of the transmitter antenna via coaxial cables of varying length. The different lengths of the cables, provided different phase shifts to the signals feeding the patches. The lengths of the coaxial cables were varied to create a difference in electrical length of $\pi/4$ between each adjacent cable. The receiver network worked in essentially the same manner, but in the reverse direction, and feeding the received signal into the network analyzer. Each part of the transmitter network is discussed in more detail below.

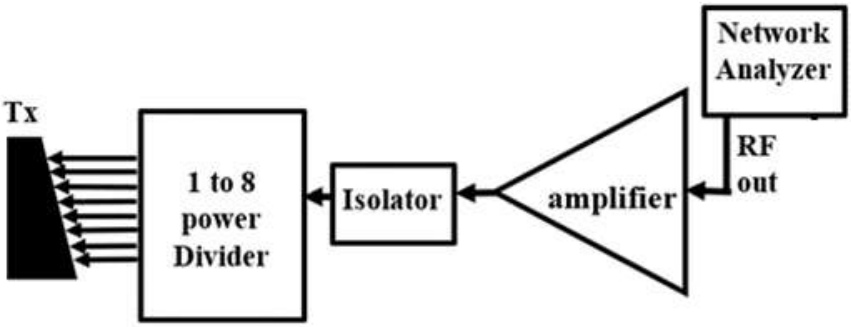

Figure 2.15 Block diagram showing transmitter network

Phase Shift

Each patch antenna was fed using a coaxial cable connected using 50Ω SMA female connectors. To generate OAM, the patches must be fired sequentially over the course of the RF cycle. This phase shift is achieved through a relative true time delay implemented in the 8 SMA cable lengths that feed the patches. Thus, in this case, the same signal was sent to each cable, but the length of the coaxial cable connected to each patch was varied to create a different phase shift in the signal reaching each patch. The difference in electrical length of

each consecutive cable was $\pi/4$. Hence the phase shift in the signal went from 0 (in the first patch) to $7\pi/4$(in the last patch). Similarly, the order of the cables can be reversed to change the phase shift in the opposite direction from $7\pi/4$ to 0, and this reverses the mode of the OAM signal. The lengths of the cables are accurate up to 0.1 radians (or 6 degrees). At 5.64 GHz the required time delay between adjacent patches is 22.16ps, corresponding to a cable length difference of 4.388mm. The cables were custom made by San Tron. A similar set of cables were also used to configure the mode of the receiver.

Power Division

The signal being fed to each phase shifter has the same amplitude and phase. The equal signals are created from a single input using a power divider. A single signal was split among the cables using an 8-way Wilkinson power divider (SP13856) from SigaTek, shown in fig. 2.16. The power divider has a nominal impedance of 50 Ω. It has SMA female connectors at input and output ports. The power divider can be reversed to work as a power combiner if the input signals are fed through the 8 output ports, giving a combined output at the input port. For this study, the combiner configuration was used with the receiver antenna, where the signal received by the 8 patch antennas was combined into a single signal. The power divider/combiner has a nominal-theoretical loss of 9.03dB. This causes the signal to be significantly attenuated in case of a transmitter and makes the receiver signal hardly perceptible.

Figure 2.16 An 8-way Wilkinson power divider

Amplification

An amplifier was connected before the Wilkinson divider to compensate for system losses. In the case of transmitter, a medium power GaAs amplifier PE15A4019 (fig. 2.17) from Pasternack was used. It has a gain of 36dB, and P1dB of 29dBm. The amplifier has a constant gain over a frequency range of 60MHz to 6Ghz. Three important precautions were taken in using the amplifier. 1. It is an ESD (electrostatic device) sensitive material, it was therefore handled only on approved ESD workstations. 2. Heat sinks were employed to control the temperature of the amplifier, by cooling through conduction. 3. The amplifier was matched for 50Ω loads and is a one-way device. Any impedance mismatch could cause reflected waves which can potentially damage the output stage of the amplifier. To avoid this, an RF isolator (fig. 2.17) with an 18dB isolation was connected at the output of the amplifier, to absorb any reflections.

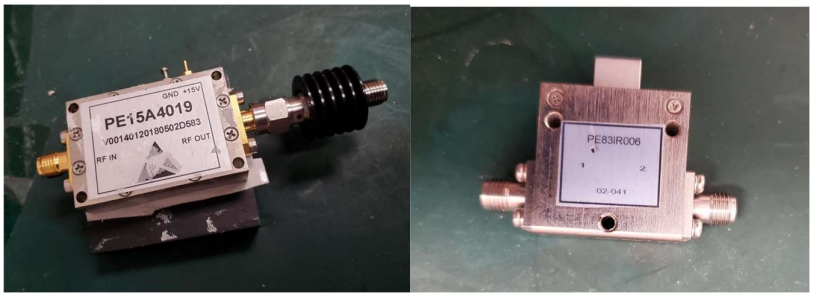

Figure 2.17 Medium power GaAs amplifier PE15A4019 is used in the transmitter network (left) RF isolator used to prevent back reflections (right)

In the receiver network, the signal collected by the receiver antenna was weak. To amplify the signal the PAM-6000 high gain, benchtop preamplifier was used. It has a gain of 30dB in the frequency range of 1 to 6GHz. The maximum RF input is 2dBm. The output of the Wilkinson combiner was directly connected to the input port of the PAM-6000 amplifier using a coaxial cable. The amplified signal from the output port is sent to the RF input port of the network analyzer.

2.5 Antenna Characterization

The constructed antenna was tested, and the antenna characteristics were verified in a full anechoic chamber (fig. 2.18) at the Southern Methodist University, using the NFH007 Allwave antenna test system. The radiation pattern in the $\varphi=0$ and $\varphi=90°$ was determined to characterize the antenna. To further observe the phase pattern of the OAM beam, a 5.64 GHz waveguide probe receiver was moved in the x-y plane, at a distance of 86 inches in front of the OAM antenna. The OAM antenna was given an input signal from the network analyzer and was used to transmit an OAM mode 1 signal. The phase pattern of the received signal was measured by the network analyzer and plotted by the Allwave software of the antenna test system. The phase pattern obtained, shown in Fig. 2.19 is distinctly a rotating phase-

front, which is in good agreement with the simulated phase pattern of fig. 2.13, which also featured a clockwise spiral. The clockwise rotation of the single spiral signifies a mode -1.

In the radiation pattern measurement of the antenna, the OAM antenna serves as a receiver. A test signal was emitted by a waveguide probe antenna at 5.64GHz. The signal captured by the OAM antenna was used to plot the radiation pattern of the antenna. The radiation pattern measured by the network analyzer in the chamber, is plotted in Fig. 2.20, for φ=0, and 90 degrees. The pattern shows a marked central null, showing an OAM singularity. Comparison to the radiation pattern in fig. 2.10 shows a good conformance between the results. Moreover, the central null obtained experimentally goes down to approximately -30 dB compared to the -22 dB obtained theoretically.

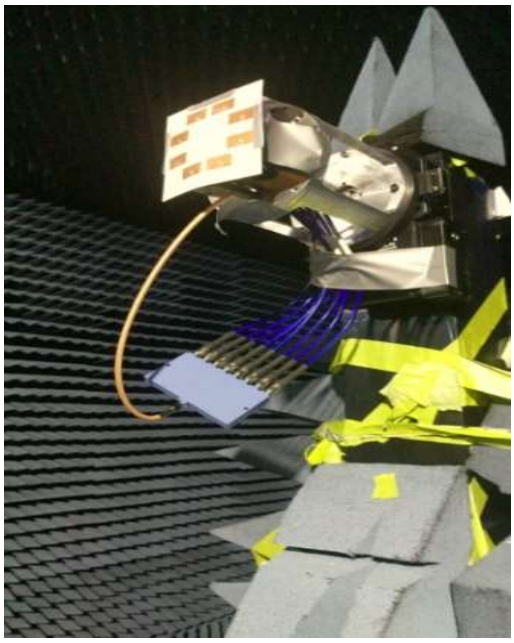

Figure 2.18 The OAM antenna is characterized in the anechoic chamber using the NFH007 Allwave antenna test system

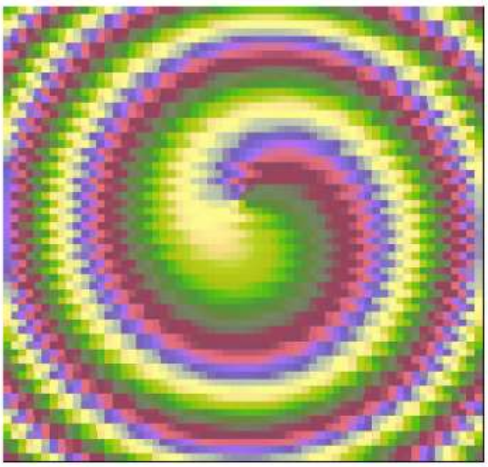

Figure 2.19 The phase pattern of the OAM antenna measured and plotted by the Allwave antenna testing system. The darkest shade represents 360 degrees and goes down to 0 degrees for the lightest shade

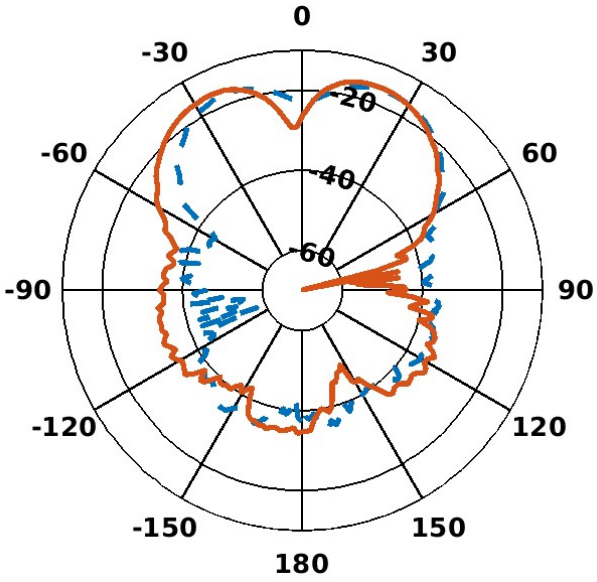

Figure 2.20 The radiation pattern of the OAM antenna measured in an anechoic chamber. The red line represents the radiation pattern on the ϕ=0 plane, and the blue line represents the radiation pattern on the ϕ=90 plane

2.6 Conclusion

The OAM antenna was constructed using the concept of phased arrays, as an array of 8 rectangular patch antennas. The mathematical calculations for the design of the patch antenna, are presented in this chapter. The dimensions of the patches were further fine-tuned based on design analysis carried out in HFSS. The optimal array radius was determined to ensure minimum side lobes gain. The OAM antenna was analyzed in HFSS. The antenna was also fabricated and tested in an anechoic chamber. The electric field magnitude and phase patterns, and the radiation patterns obtained, both experimentally and theoretically showed a distinct OAM signal being produced at the required frequency of 5.64 GHz. The radiation pattern obtained through simulations shows a central null of -22 dB, whereas the measured radiation pattern has a central null going down to approximately -30 dB. Hence, a measured value better than the simulated value has been achieved. An OAM antenna based on phased arrays was successfully designed and fabricated and is suitable for use in experiments to determine crosstalk reduction.

Chapter 3

CROSSTALK REDUCTION EXPERIMENTS

A full duplex system consists of both uplink and downlink data being transmitted simultaneously on the same channel. Therefore, there is a transmitter and receiver pair on both ends of the system. When the local transmitter and receiver are placed adjacently on one end of a full duplex system working at the same frequency, power from the transmitter leaks to the receiver as crosstalk (fig. 3.1). This obscures the already weak received signal, and results in loss of information. Since an OAM signal can have theoretically infinite orthogonal modes, the use of mismatching OAM modes may benefit the system by creating an added isolation. Although OAM orthogonality has previously been applied in multiplexing, the crosstalk between two local OAM antennas has not been studied. This chapter studies the isolation due to OAM orthogonality, between two local OAM antennas placed adjacently on a horizontal plane.

Using the OAM antenna designed in the previous chapter, an experiment was designed to determine the amount of crosstalk reduction due to OAM. The experiment also studied the variation of the isolation with distance between the antennas, to determine the ideal distance between the antennas for maximum isolation. This chapter describes the assembly of the transmitter and receiver networks. It illustrates a detailed description of the experiment carried out to determine the crosstalk between two OAM antennas, and presents the results of the investigation.

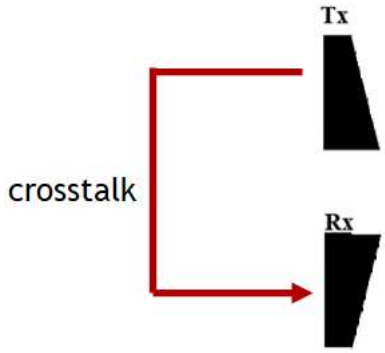

Figure 3.1 Power from the transmitter leaks to the adjacent receiver

3.1 Experimental Setup

The block diagram in fig. 3.2 shows the setup for the experiment. It consists of the transmitter and receiver networks connected to the network analyzer. The transmitter network amplifies the signal provided by the network analyzer, and then divides it into 8 equal signals as discussed in the previous chapters. The signals are then fed to the 8 patches of the transmitter array via coaxial cables of varying lengths. The signal emitted by the transmitter leaks to the receiver antenna. The signal collected by each patch of the receiver array is passed through coaxial cables of varying lengths. Each cable provides a different relative phase shift to the signal due to the variation in length. The signals are combined by a Wilkinson power combiner, in a manner similar to the transmitter network, discussed in chapter 2. The signal captured by the receiver antenna is similarly combined, amplified and fed back into the RF input port of the network analyzer.

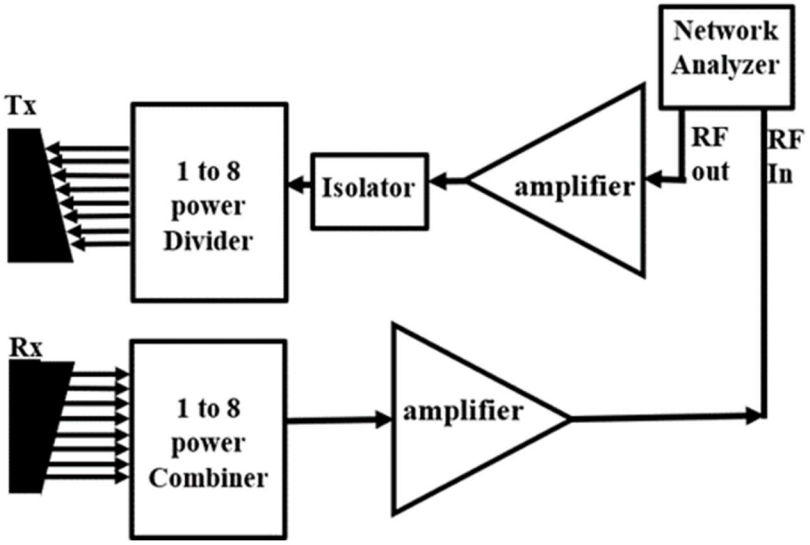

Figure 3.2 Block diagram of the setup for transmitter and receiver

All connections between the different parts of the RF system are made using coaxial cables. During experimentation, moving or bending the coaxial cables, significantly altered the readings. To obtain accurate measurements, it is important not only for the performance of the antennas to be satisfactory, but also for the cables to be efficient. For this reason, ATC-PS test cable assemblies from Newark were employed. These low loss 50Ω coaxial cables are amplitude and phase stable over a frequency range of 0 to 20 GHz. The phase stability (with bending) of the cables was 5° (0.09 radians), while the maximum amplitude stability was 0.16dB.

The 8752C Network analyzer was used for the measurements. This network analyzer is operable over a frequency range of 300KHz to 6GHz. The network analyzer sends in a test signal to the transmitter network. The receiver network is connected to the input port of the network analyzer, to feed the received signal back into the network analyzer. The frequency range of the

network analyzer is set from 2GHz to 6GHz. The network analyzer is used to measure the log magnitude of the signal transferred from the transmitter to the receiver, thereby providing the S_{12} value.

3.2 Experiment

The purpose of the experiment is to determine the crosstalk between two adjacent OAM antennas. The transmitter and receiver antennas were held by wooden frames that are placed side by side as shown in Fig. 3.3. The distance between the antennas was measured from the edge of the transmitter array to the edge of the receiver array. When the antennas are placed adjacent to each other in this way, the log magnitude of the signal detected by the network analyzer is essentially the crosstalk measurement S_{12} between the transmitter and receiver. The experiment was carried out in a full anechoic chamber to exclude the effects of any reflected radiation, and to enhance the accuracy of the experiment. The horizontal distance between the two antennas varied from 5.7 cm to 9.7 cm, in increments of 1 mm. For every value of distance, the S_{12} crosstalk measurement on the network analyzer was noted for the frequency of 5.64GHz.

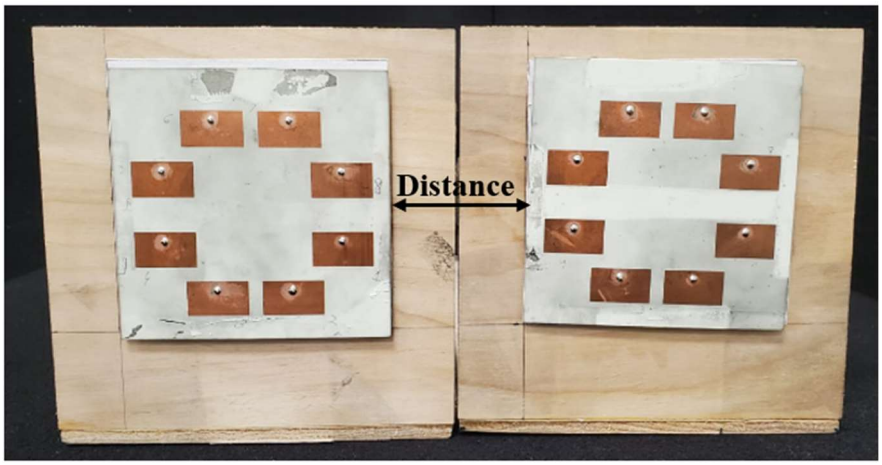

Figure 3.3 The transmitter and receiver antennas placed side by side

Increasing the horizontal distance between the adjacent transmitter and receiver antennas would naturally vary the crosstalk value S_{12}. However, the objective of the experiment is to determine the additional crosstalk created due to the orthogonality of OAM modes, and to observe its variation with distance. Therefore, we must consider the difference between the S_{12} values when both antennas have the same OAM modes, and when both antennas have opposite OAM modes, and calculate the difference between the crosstalk value to determine the differential or additional crosstalk that exists due to the OAM nature of the waves. In taking the difference between the two crosstalk values, the effect of other factors such as distance between the antennas gets cancelled out, as it is the same for both cases. The mode of the receiver is switched from +l to -l by reversing the sequence of the cables connected to the patches, which reverses the direction in which the phase shift increases around the array. The experiment is repeated for the opposite mode, and S_{12} values are again noted. Therefore, two cases have been studied (as illustrated in fig. 3.4)

i) transmitter mode l_{Tx}=1, and receiver mode l_{Rx}=1

ii) transmitter mode l_{Tx}=1, and receiver mode l_{Rx}= -1

To see the effect of the mode of the OAM signal on isolation, the difference between S_{12} values for the case of l_{Rx}=1, l_{Tx}=1 and the case l_{Rx}=-1, l_{Tx}=1, must be calculated. This value is the differential crosstalk ΔS_{12}.

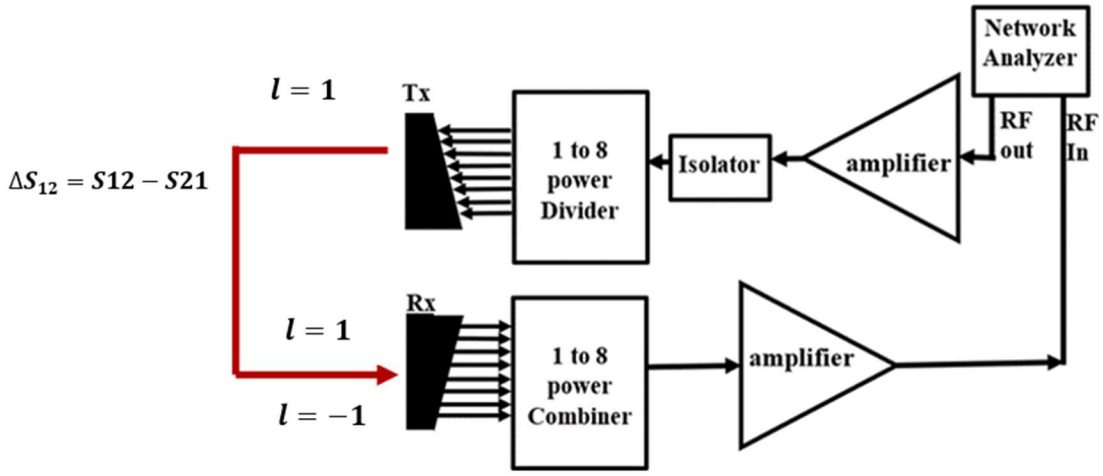

Figure 3.4 Two cases are considered in the experiment, when receiver mode is *l*=1 and when it is *l*=-1. Transmitter mode is fixed at *l*=+1 for both cases

3.3 Experimental Results

The readings obtained from the experiment, are the S_{12} readings for the two cases where receiver mode is *l*=+1, and where the receiver mode is *l*=-1. The example of a network analyzer reading is shown in fig. 3.5. It shows the plot of S_{12} against frequency, and maximum signal is received at 5.64GHz which is the resonance frequency of the antennas.

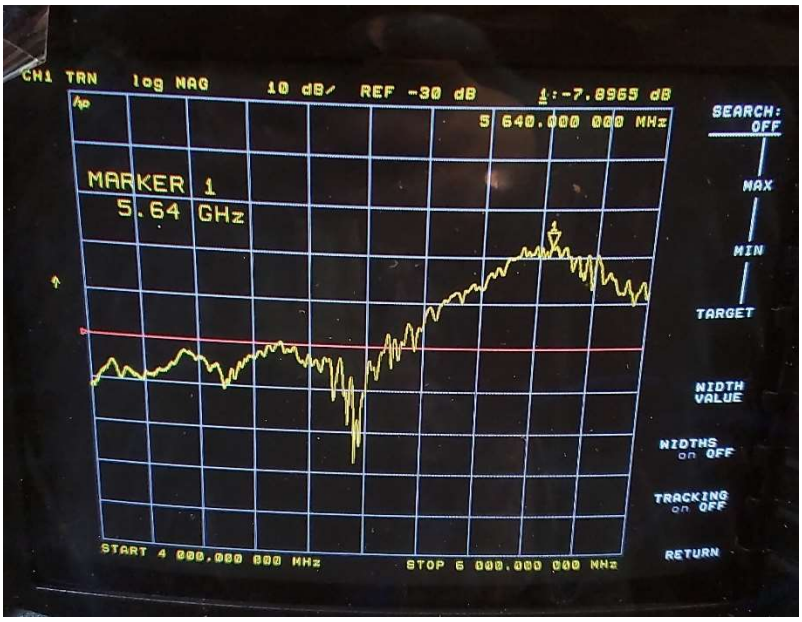

Figure 3.5 An example of the S_{12} readings measured by the network analyzer during the experiment

The S_{12} values are noted for each distance, and the results are plotted against the distance between the two antennas, as shown in fig. 3.6. The graph of fig. 3.6 displays the effect of the receiver OAM mode on the crosstalk, and the variation of crosstalk with distance for each case. Although both curves have an oscillatory behavior with distance, there is a distinct difference between the results for both modes. This is because as the receiver phase shifts act upon the crosstalk signal, they may add constructively or destructively with the phase shifts of the transmitter. Since this depends on the mode of the receiver, different results are obtained for both cases. The difference of the two plots provides the differential crosstalk ΔS_{12}. This excludes the effect on isolation due to the physical distance between the antennas, and is the real measure of crosstalk reduction due to the OAM nature of the waves.

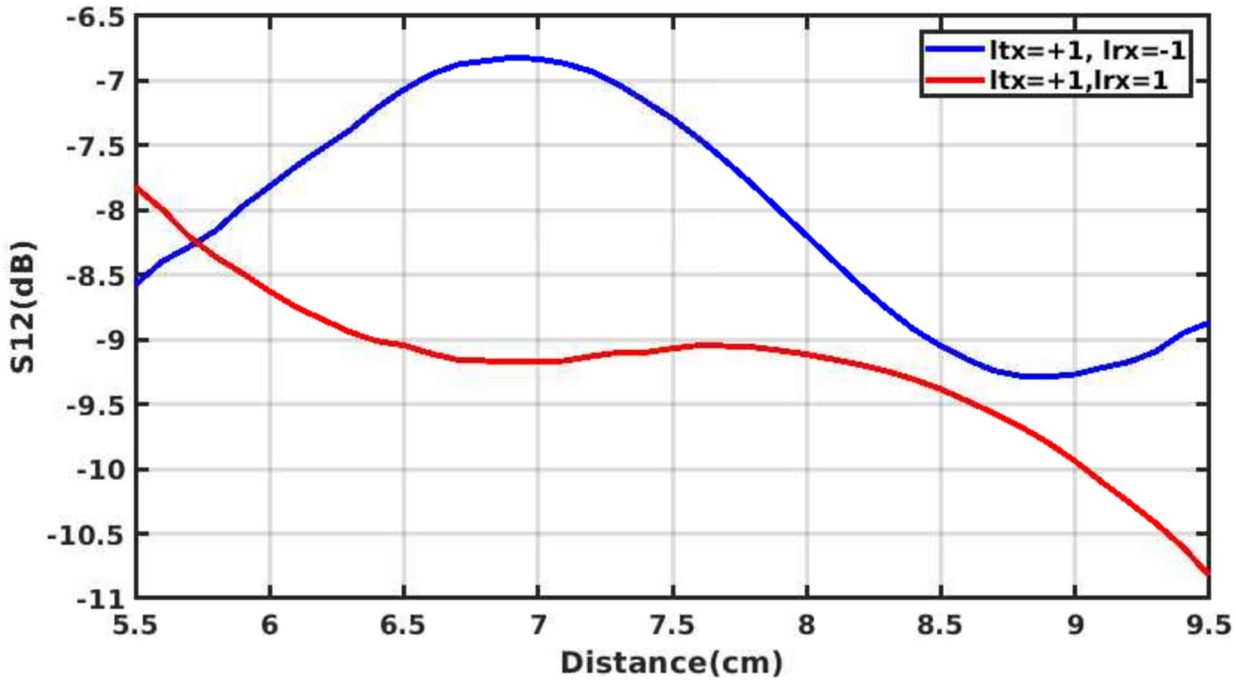

Figure 3.6 The S12 readings for case l_Tx=+1, l_Rx=+1 (blue), and l_Tx=+1, l_Rx=-1 (red) are plotted against distance between the transmitter and receiver antennas

Differential crosstalk, ΔS_{12} is plotted against the horizontal distance between the transmitting and receiving antennas. The graph shows an oscillatory behavior of differential crosstalk ΔS_{12} with distance (Fig. 3.7). It can be seen from the graph that the maximum ΔS_{12} achieved experimentally is 2.6 dB. The sinusoidal variation of the differential crosstalk with distance, indicates that there is a phase change in the signal with distance as it travels through the air from the transmitter to the receiver. This phase shift created due to the propagation delay of the signal, adds to the phase shifts of the transmitter network. Although the distance travelled by the signal from each transmitter patch is different, it can be approximated as d for every patch. At the receiver end, the phase shifts may add constructively or destructively with the phase shifts

of the receiver network, resulting in the variation of the S12 values that leads to the oscillatory behavior.

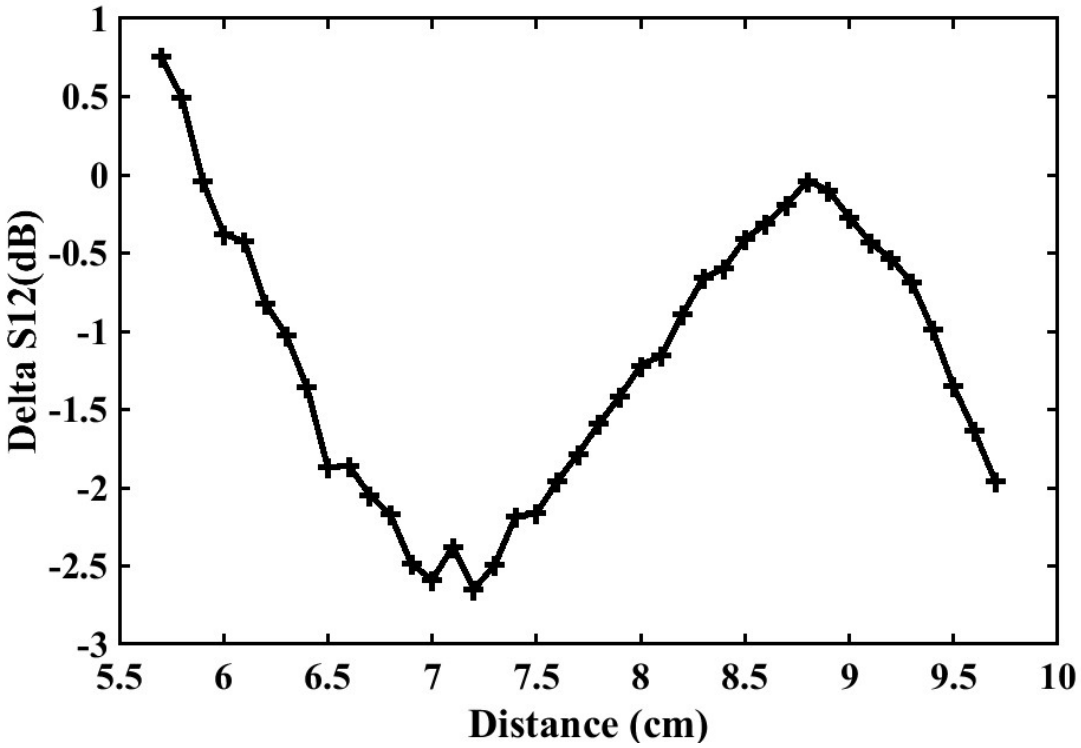

Figure 3.7 Variation of differential crosstalk ΔS12 with distance between the antennas at 5.64GHz

3.4 Conclusion

An experiment was carried out to determine the effect of OAM on crosstalk reduction, and the variation of differential crosstalk with distance between two adjacent OAM antennas. The experiment was carried out in a full anechoic chamber using phase stable and amplitude stable cables, to ensure high accuracy. The experiment considered the S_{12} values between transmitter and receiver for the case when the transmitter and receiver both have the same OAM modes, and when both have opposite modes. The difference between the two measurements was calculated as the differential crosstalk. A maximum differential crosstalk of 2.6 dB was obtained experimentally.

The variation of differential crosstalk with distance shows an oscillatory trend, signifying the variation of phase of the signal as it travels through the distance. The phase shift of the signal with propagation distance causes the signal to add constructively with the phase shifts at the receiver for some distances, and destructively for others. Therefore, the plot of differential crosstalk shows an oscillatory trend. This data is especially useful in selecting the distance between the antennas to achieve maximum isolation.

Chapter 4
SIMULATION OF CROSSTALK REDUCTION EXPERIMENT

In chapter 2, the theoretical analysis and characterization of the OAM antenna using HFSS, was described. Chapter 3 detailed an experiment that used the OAM antennas to investigate the effect of the OAM modes of two local antennas, on the crosstalk between them. This chapter explores the simulation of the experiment in HFSS, to verify the results that were obtained experimentally.

4.1 Antenna design in HFSS

The design of the antenna in HFSS is shown in fig. 4.1. The antenna is surrounded by an airbox (not shown), which is assigned as a FE-BI (Finite Element Boundary Integral) boundary. The use of FE-BI boundary, in this case, allows for smaller simulation volume and shorter simulation time while providing high accuracy. In this model, lumped ports are used to provide excitation to the patch antennas. The magnitudes and phases of the excitation voltage sources can be set to create a 45-degree phase shift between adjacent patches, for a transmitter array. The antenna can be used to generate OAM mode +1 or mode -1 as seen in chapter 2. Modal solution type is used for the analysis.

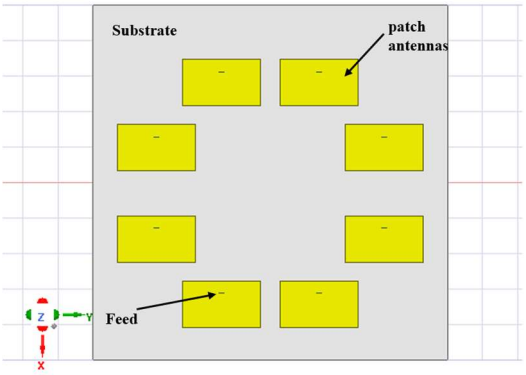

Figure 4.1 Design of the patch array in HFSS

The experiment for the coupling measurement consists of two antenna arrays, a transmitter and a receiver placed adjacently in the same horizontal plane. An HFSS model with two copies of the array as components, is created. The two arrays were placed in HFSS as shown in fig. 4.2.

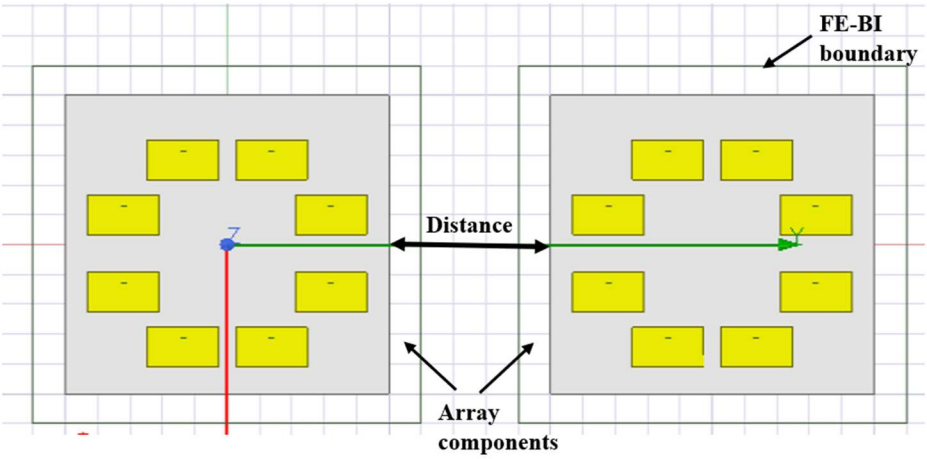

Figure 4.2 Model of the transmitter and receiver antenna arrays in HFSS

4.2 ANSYS Circuit

Like HFSS, ANSYS Circuit is a part of the ANSYS electronics simulation environment. It can be used to create high frequency circuit schematics, and can be used in conjunction with ANSYS HFSS. To provide the phase-shifted excitations to the array elements, ANSYS Circuit was employed. In the same project, a new circuit file is added. The HFSS design file was copied and pasted into the circuit file. This created a component in the Circuit design file, which symbolizes the HFSS model. The component or subcircuit model was dynamically linked to the HFSS design file. The subcircuit model had 16 pins, 8 of which were linked to the 8 lumped ports of the transmitter array and 8 to those of the receiver array. An input port is inserted, and a voltage source is added to it. The port was then connected to a 1 to 8 power divider to split the signal into 8 equal signals. After that, each pin of the power divider was connected to a phase shifter, for which the phase shift was set to the desired value. The phase-shifted signals were connected to the first 8 pins of the antenna component, to provide input to the elements of the transmitter array. Similarly, the remaining 8 pins were connected to the receiving network, which comprises of phase shifters and an 8 to 1 power combiner. The receiving network terminated in an output port. The complete schematic is shown in fig. 4.3. The measurement of the S_{12} parameter between the input and output ports is essentially the crosstalk coupling between the transmitter and receiver array.

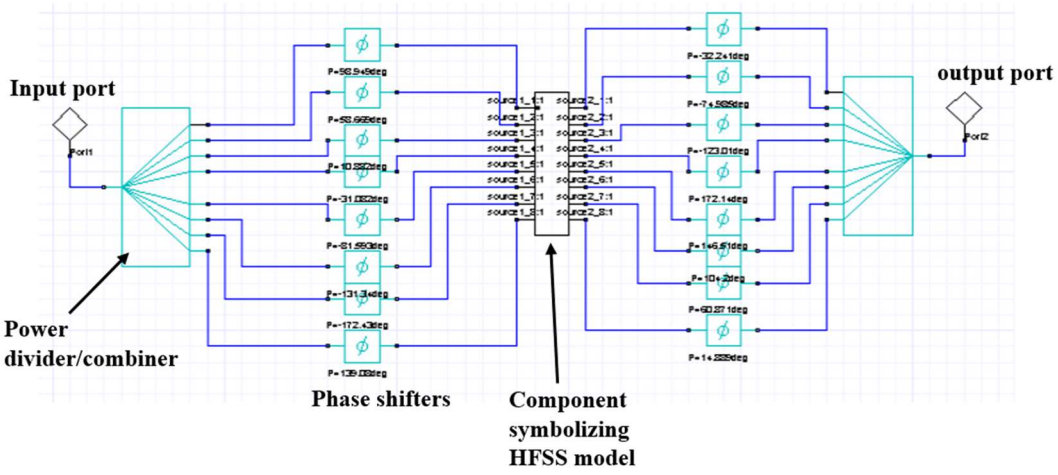

Figure 4.3 The circuit schematic in ANSYS Circuit. The feeding network consists of a power divider for splitting/ combining the signal and 8 phase shifters to shift the phase of the signal in each branch. The signal in each branch of the feeding network connects to a pin of the HFSS model component

A parametric analysis was also run in HFSS, to vary the distance between the two arrays. The linked data was used to run a parametric analysis in ANSYS circuit for the distance parameter. The OAM mode of the antennas could be changed by reversing the direction in which the phase shift increases, i.e. from 0 to 315 degrees, or from 315 degrees to 0 degrees. The experiment was repeated for both mode +1 and -1 of the receiver, with transmitter mode fixed at +1. The crosstalk S_{12} was measured in ANSYS Circuit for both cases.

4.3 Filtering the Results

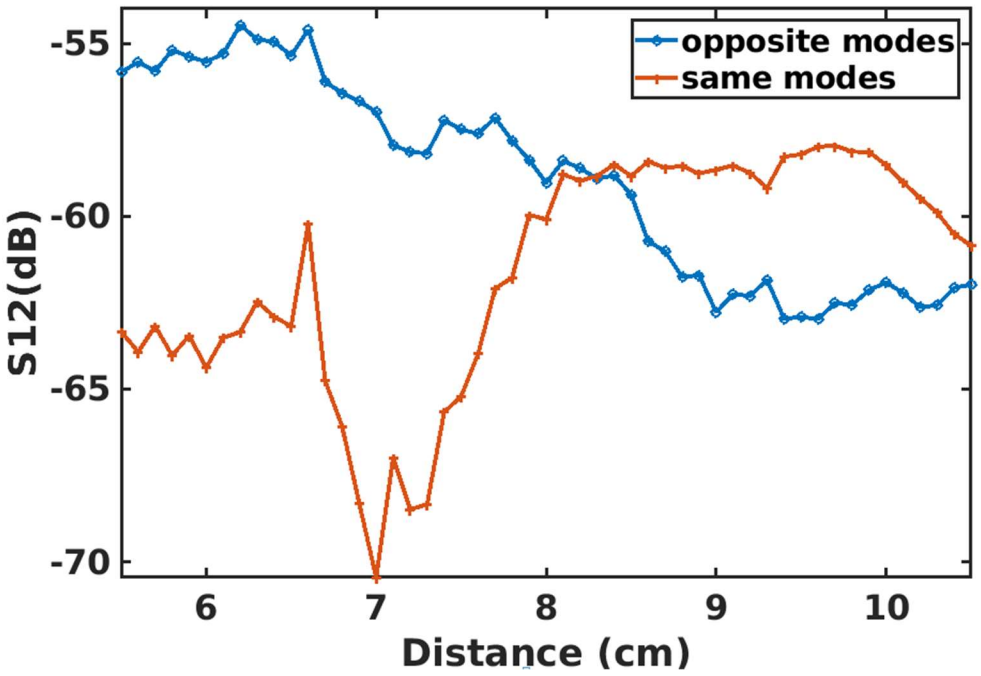

Figure 4.4 The results obtained for S_{12} against the distance between the arrays, for the transmitter and receiver having the same OAM modes and opposite OAM modes

The results obtained for S_{12} were plotted against the distance between the two antennas and are shown in fig. 4.4. The plots have a significant amount of noise. However, increasing the accuracy by reducing the value of maximum delta S, does not help in reducing the noise, and the high noise in such a weak signal makes the information obtained unreliable. This is especially true where we need to obtain the difference between the two cases: opposite modes and same modes, to calculate the differential S_{12}, which is already a small value.

To extract reliable information from the data obtained through HFSS, we propose a method of filtering out the noise. A code written in MATLAB was used to create a moving

average filter using the smooth command, to filter out the noise and obtain the information embedded in the S_{12} against distance plot. The filtered signal is shown in fig. 4.5. Although there was a hint of the oscillatory trend of S_{12} with distance in fig. 4.4, the variation is much more pronounced in fig. 4.5. Thus, a very simple and easy-to-use method for filtering the noise, was employed to extract useful information out of the otherwise unusable data obtained from HFSS. Furthermore, as discussed above, a moving average of multiple runs was taken to ensure the accuracy of the results.

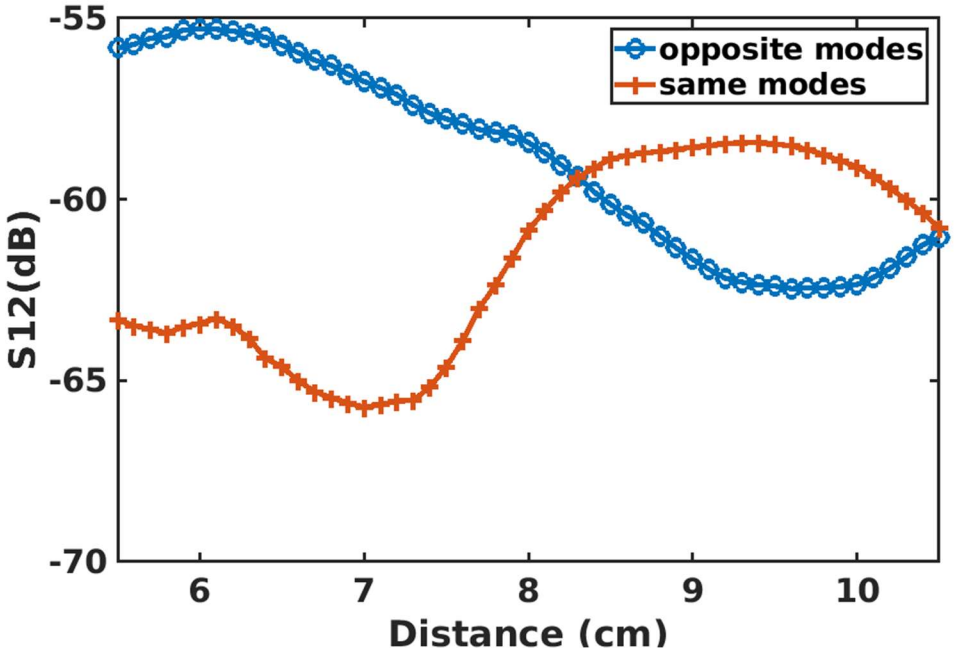

Figure 4.5 The results obtained for S_{12} against the distance between the arrays, after passing through a moving average filter

4.4 Comparison between Theoretical and Experimental Results

As was previously done in the practical experiment, the difference between S_{12} values for both cases: opposite modes and same modes, was calculated to obtain the differential crosstalk ΔS_{12}.

This value shows the amount of isolation achieved due to the OAM nature of the waves. ΔS_{12} was then plotted against the horizontal distance between the two antennas, to observe the effect of distance on the differential crosstalk. The plot is shown in fig. 4.6 along with the plot obtained from experimental results.

The values of differential crosstalk ΔS_{12} are plotted against distance, and compared with the plot obtained through practical measurements, in Fig. 4.6. The simulation shows an isolation of 3.6 dB, whereas experimental results give a maximum isolation of 2.6 dB. The sinusoidal variation of differential crosstalk ΔS_{12} with distance, is evident from both plots. The half wavelength of a 5.64 GHz signal can be calculated as 2.7 cm, and it can be seen from the figure that the half wavelength of the simulated curve is 3 cm. This result is in good agreement with the half wavelength of a 5.64 GHz signal.

Despite differences between theory and experiment, a good match can be seen between the behavior of the experimental and simulated plots. All connections and components in the simulation are considered lossless. The simulation also uses ideal phase shifters to model the coaxial cables which have been used to provide phase shift to the patch antennas. In practice there is a ±6-degree (0.1 radians) error present in the phase shift provided by these cables. Moreover, the manual translation of the receiver away from the transmitter contributes human error to the experiment.

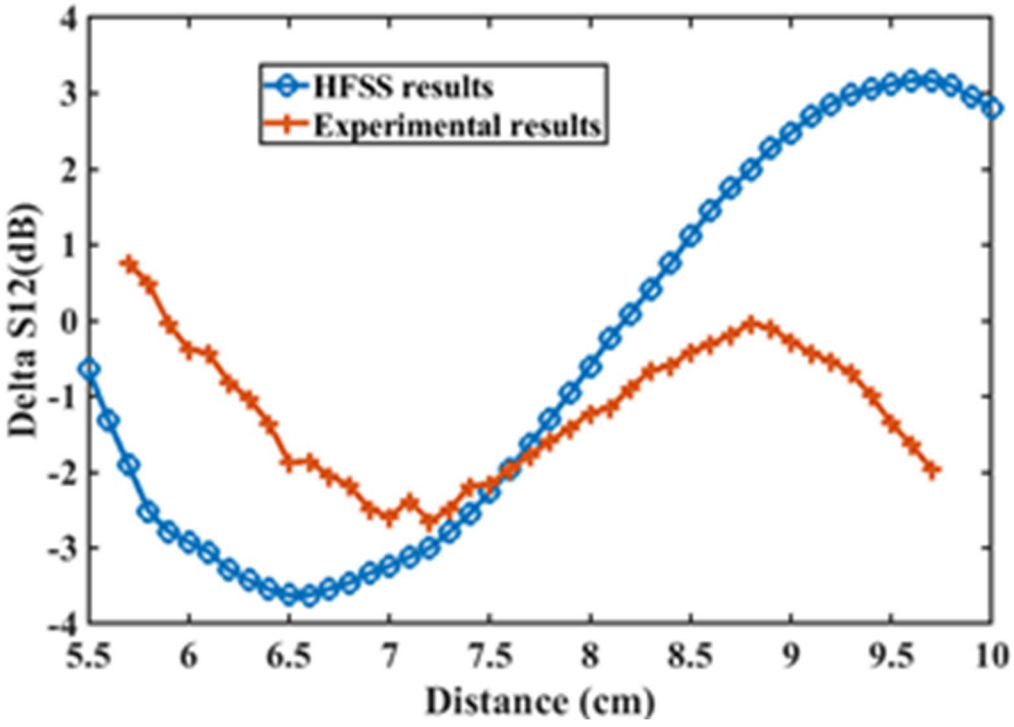

Figure 4.6 Simulated and experimental results for ΔS_{12} as a function of horizontal distance between transmitter and receiver

4.5 Conclusion

High Frequency Simulation Software (HFSS) is a powerful tool for the simulation of electromagnetic problems. The software was used to design and analyze the OAM antennas used in this research. It was also employed to simulate the experiment to determine the relationship between crosstalk reduction and the distance between the transmitter and receiver antennas. ANSYS Circuit was used to create the feeding networks of the transmitter and receiver antennas. The results obtained had a high level of noise. A moving average filter was used to filter out the noise. The theoretical results obtained from HFSS are found to be in good agreement with the experimental results.

The theoretical results obtained from the simulation, showed a maximum differential crosstalk of 3.6 dB. Like the experimental results, a sinusoidal variation of differential crosstalk is seen, with distance between adjacent antennas. The variation is because of a phase shift being added to the signal due to its propagation over the distance between the transmitter and receiver. This causes the signal to add constructively with the receiver phase shifts at some distances, and destructively at others.

Chapter 5

CROSSTALK REDUCTION IN CONCENTRICALLY PLACED ANTENNAS

Chapters 3 and 4 have established that the crosstalk between two adjacent OAM antennas is affected by the OAM nature of the signal being transmitted. The isolation due to OAM, achieved theoretically, was 3.6 dB, and was experimentally measured to be 2.6 dB. Such findings encourage the exploration of other topologies that may provide higher values of isolation due to OAM. The configuration studied in this chapter consists of two concentric OAM antennas on the same substrate, being used as a local transmitter and receiver. This nested setup is more compact and practical for OAM implementation in full duplex systems, as it allows both antennas to use the same space. Moreover, it is difficult to design focusing dishes for antennas placed side by side. This chapter explores the amount of isolation achievable through this geometry, and the effect of the OAM mode of the outer array on the crosstalk between the two antennas.

5.1 Antenna Design

The setup consists of two OAM antennas built on a common substrate and placed concentrically in relation to each other. The transmitter and receiver antennas are designed as circular arrays of patch antennas, as used previously in chapter 2. Since the frequency of operation remains the same at 5.64 GHz, the same patch dimensions as before are used as designed in chapter 2. The two parameters that are altered in this experiment are the placement of the arrays, and the OAM mode of the arrays.

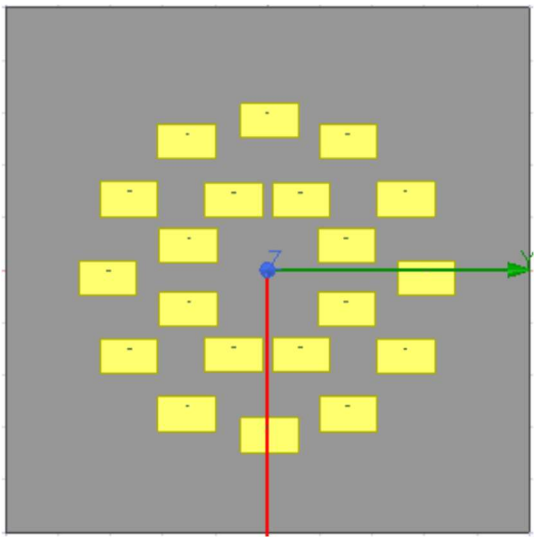

Figure 5.1 Transmitter and receiver antennas are, arranged concentrically on the same substrate

The arrays are placed concentrically in relation to each other (fig. 5.1). Therefore, the ideal array radius determined in section 2.3 cannot be used for the two arrays. The inner array radius is reduced to 32 mm, to allow space for the outer array. At this radius, the radiation pattern still forms a distinct OAM shape, as shown in fig. 5.2. The OAM mode of the inner array is fixed at mode l=+1, and the number of patch antennas in the inner array is kept at 8.

To ensure that the outer array does not overlap with the inner array, the radius of the outer array is increased from the ideal radius of 34mm, which was determined in section 2.3. The minimum radius at which the arrays do not overlap was found to be 60mm. With the greater radius, it is important to ensure that the signal is not under-sampled, and that a sufficient number of patch antennas is selected. Moreover, the outer array is required to produce OAM modes ranging from mode -5 to +5, and must be configured for higher order modes, as well. Therefore, the number of patch antennas in the array must satisfy the condition $N>2|l|+1$ [46], [57]. To

allow for the possibility of a higher order mode l=5 being induced in the outer receiver array, and for the sake of symmetry and continuity, N>11, i.e., 12 patch antennas are used in the outer array. Therefore, the number of patch antennas in the outer array is selected as 12, due to the geometrical constraints that result from having to avoid overlap between the patches, while also avoiding under-sampling of the phase distribution. For N=12 patches, the inter-patch phase shift in the outer array, creating mode l=1 may be accomplished using the following calculation:

$$phase\ shift = \left(\frac{360l}{N}\right) = 30°$$

Similarly, to create mode l=2 and mode l=3, an inter-patch phase shift is selected at 60° and 90,° respectively.

The radiation pattern of the inner arrays is shown in fig. 5.2 and the pattern for the outer array is shown in fig. 5.3, on the Φ=0 and Φ=90 planes. For both arrays, there is a marked dip in the center for both the Φ=0 and Φ=90 planes, which is characteristic of an OAM. In fig. 5.2, the field in the center reduces to approximately -30dB, signifying a good vortex beam. In fig. 5.3, for the outer array, the beam center dips to -28dB for mode l=1, and up to approximately -20dB for modes l=2 and l=3. The radiation patterns for the outer array exhibit significant side lobe gains, since the array radius used is not the optimum radius determined in section 2.3.

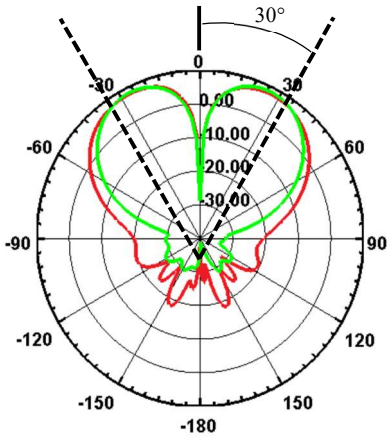

Figure 5.2 Radiation pattern of inner array with an array radius of 32mm, and an OAM mode *l*=1 in the Φ=0 (red) and Φ=90 planes

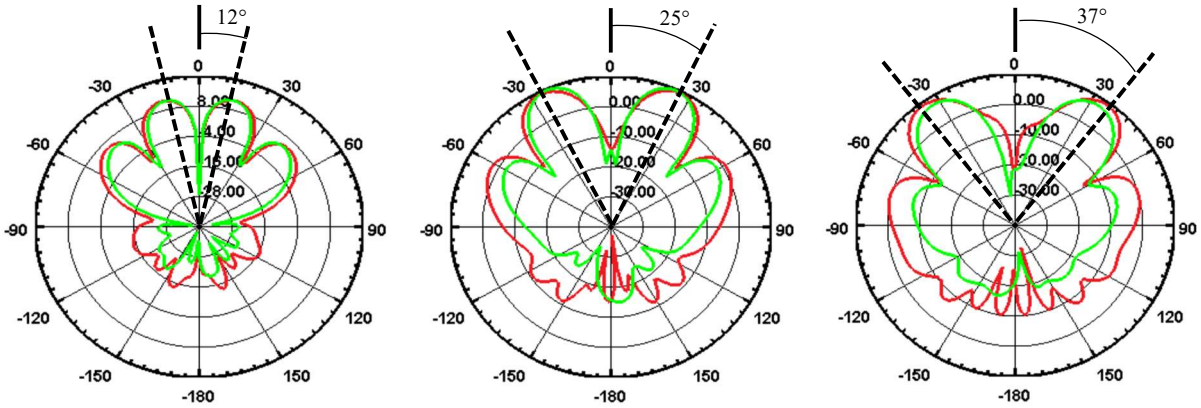

(a) (b) (c)

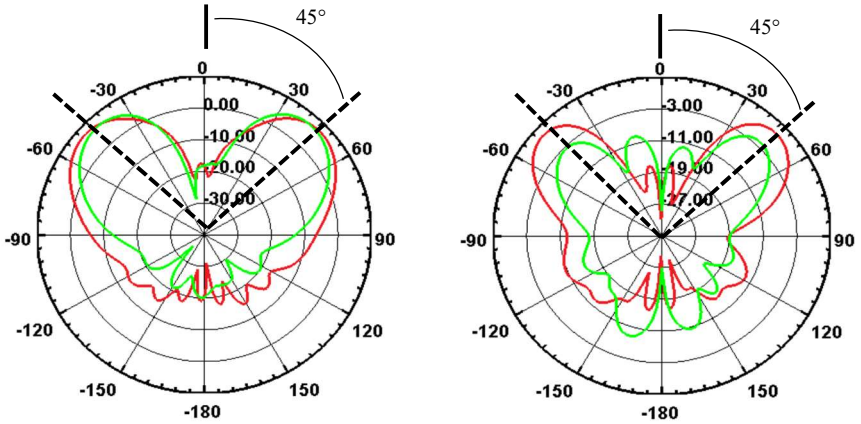

(d) (e)

Figure 5.3 Radiation pattern of an outer array with a radius of 60mm, and OAM modes (a)1 (b) 2 and (c) 3 (d) 4 (e) 5 in the Φ=0 (red) and Φ=90 (green) planes

5.2 Collimation Using Dish Antennas

It is important to note that the radiation patterns featured in fig. 5.3 also illustrate the angular direction in which the beams propagate. OAM beams tend to diverge as they propagate, and the divergence is greater for higher order modes. From fig. 5.3, one can observe that, for the inner array, the beam divergence is 30° from the normal to the center of one lobe. For the outer array, the beam divergence is 12° for mode 1, 25° for mode 2, and 37° for mode 3. This means that after travelling a distance from the transmitter to a distant receiver, the size of the beam would be much larger than the receiver array. This means that the receiver patches would not be able to collect all of the signal transmitted. One solution to this problem is the use of parabolic dish antennas to collimate the signal.

By virtue of the parabolic shape of the dish reflector, and the fact that the reflected angle is always equal to the transmitted angle, every signal emanating from the focal point of a parabolic dish would be reflected by the dish in a direction parallel to the horizontal axis (as shown in fig. 5.4). This causes the beam to collimate. Conversely, any beam parallel to the horizontal axis incident on the parabolic dish would be focused on the focal point. The latter of these two concepts will be used to reproduce the beam at the receiving end.

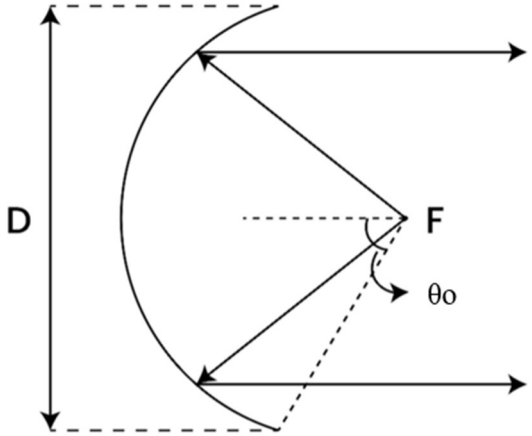

Figure 5.4 A ray diagram showing that any signal emanating from the focal point would be reflected by the dish in a direction parallel to the horizontal axis

A parabolic dish antenna can be described by two parameters, the focal point F, and the diameter D of the dish, both of which are illustrated in fig. 5.4. The focal point is a point equidistant to every point on the parabola. The ratio F/D, which determines the curvature θ_o of the dish, is defined in terms of the curvature of the antenna by the following:

$$\frac{F}{D} = \frac{1}{4 \tan \frac{\theta_o}{2}} \qquad (1)$$

Further, the gain G and beam width Ψ of the dish may be calculated using equations (2) and (3), respectively.

$$G = 10 \log_{10} k \left(\frac{\pi D}{\lambda}\right)^2 \qquad (2)$$

In the above equation, k represents the beam's efficiency factor, which is generally 50-60%. D is the diameter of the dish in meters, and λ is the wavelength of the signal in meters, which is 53mm, in this case.

$$Beam\ width\ \Psi = \frac{70\lambda}{D} \quad (3)$$

Beam width is the angle (in degrees) on the radiation pattern of the dish where the beam power has reduced to half of the maximum (i.e., -3dB).

Consider the OAM signal generated by the inner array to be feeding a parabolic dish. From fig. 5.2, it can be observed that the beam would diverge by a 30° angle. If the array is placed at the focal point F of a parabolic dish, then the beam radius after travelling a distance F is given by $d = F \tan 30 = 0.57F$. To ensure that the incident beam is not extending outside of the surface of the dish, the radius of the dish must be greater than the beam radius of the incident beam. Therefore, the dish diameter must satisfy $D > 2d = 1.14F$. And

$$\frac{F}{D} < 0.866m \quad (3)$$

Taking the example of a parabolic dish with beam width Ψ =3.5, D can be calculated using (3) as D=1m. And from (3), selecting $\frac{F}{D} = 0.7$, the focal distance can be calculated as F=0.7m. This means that while traveling a distance of 0.7m, the beam radius of the OAM signal would increase d=0.404m. This confirms that the beam would be within the diameter of the dish antenna and that the selected parameters are appropriate for collimation.

Similarly, the dish may be designed to collimate the different modes of the outer array. However, since the outer and inner arrays are coplanar, and the position of the array would be

fixed at the same location for all modes of the outer array, the focal point F of the dish must be the same for the signals of both the inner and outer arrays and for all OAM modes required. Therefore, the design of the dish diameter may be accounted for while simultaneously keeping the value of the focal point fixed.

For OAM mode l=1 of the outer array, the angle of divergence is 12 ° (see fig. 5.3). Therefore, the beam radius d, after traveling a horizontal distance F is, $d = F\tan 12 = 0.213F$. And to ensure that the beam does not diverge from the dish, a diameter $D > 2d = 0.425F$ is used. For F=0.7m (which was calculated for the inner array), **D>0.298m**. For the outer array mode l=2, the angle of divergence is 25° (see fig. 5.3). The beam radius after traveling a distance F is then $d = F\tan 25 = 0.466F$. This means that the required dish diameter is $D > 2d = 0.933F$. For F=0.7m, **D>0.653m.** Along these same lines, the required dish diameter for OAM mode l=3 of the outer array is calculated as **D>1.05m.** It is evident that a dish antenna with a diameter of 1m would be suitable for the inner array, and modes l=1 and l=2 of the outer array, but not for mode 3 of the outer array. It would be wiser to select the focal length F according to mode l=5 of the outer array, and use the value of F to determine the corresponding required dish diameters for the other OAM modes feeding the dish. Without repeating the details of the calculations, the results are stated below.

Take the example of a dish with a diameter of D=1m, and a beam width of Ψ =3.5. For the outer array mode l=5, the angle of divergence is 45° (see fig. 5.3). The beam radius after traveling a distance F is then $d = F\tan 45 = F$. This means that the required dish diameter is $D > 2d = 2F$. For D=1m, the condition F<0.5m must be satisfied; therefore, F is selected as 0.4m.

For OAM mode l=4 of the outer array, the angle of divergence is 45°. D>2($F\tan 45$) must be satisfied. For F=0.4m calculated for mode 5, D>0.8 is satisfied by a dish of diameter 1m.

For OAM mode l=3 of the outer array, D>0.6m must be satisfied.

For OAM mode l=2 of the outer array, D>0.4m must be satisfied.

For OAM mode l=1 of the outer array, D> 0.17m must be satisfied.

For OAM mode l=1 of the inner array, D> 0.46m must be satisfied.

Therefore, at a focal length of 0.4m, a dish diameter of 1m would be appropriate for both the inner and outer arrays feeding the dish, and for all modes of the outer array. Using (2), the gain of the dish antenna with a diameter of 1m can be calculated as 23dB. If the diameter is increased to 2m, the gain is then 30dB.

5.3 System Design

5.3.1 Full Duplex System Using Ray Matrices

The full duplex system is comprised of a transmitter and receiver at the east end and an identical transmitter and receiver at the west end. To mitigate the problem of beam divergence, parabolic reflector antennas are employed on both the East and West sides. The transmitter antenna is used as a feed for the dish, and the dish collimates the signal. Therefore, the collimated signal can travel a longer distance without diverging. On the West dish, the signal is converged to the West receiver array. Ray tracing and ABCD matrices can be used to numerically represent the system design. Fig. 5.5 depicts a ray diagram for the full duplex system. Here, one can note the ray emerging from the focal point of the East transmitter and travelling to the West transmitter with the aid of two parabolic reflectors.

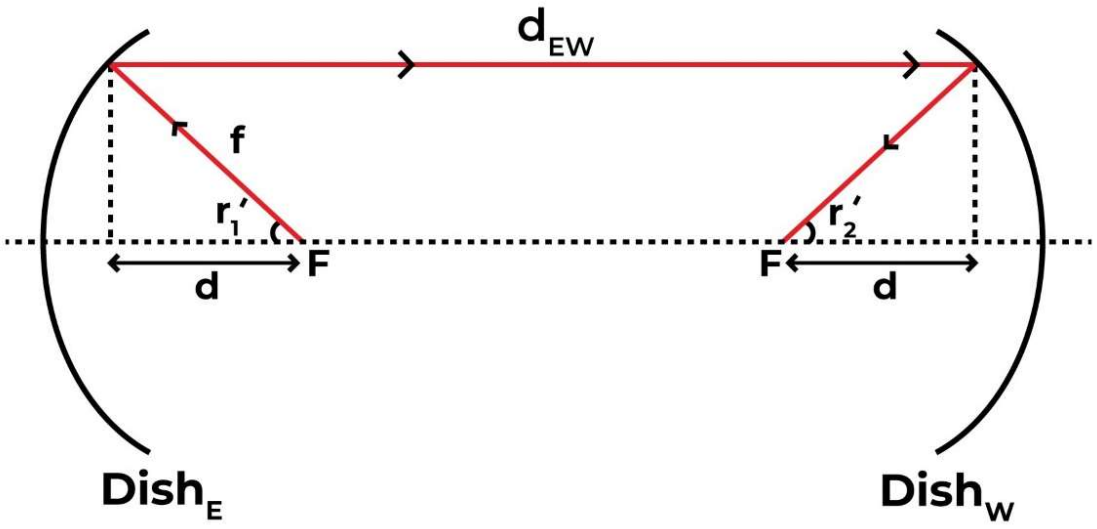

Figure 5.5 Ray diagram for a full duplex system, with a transmitter at the focal point of the East dish and the corresponding receiver at the focal point of the West dish

Consider the incident ray to be $\begin{bmatrix} r_1 \\ r_1' \end{bmatrix}$, where r_1 is the distance of the ray above the horizontal axis, and r_1' is the angle of the ray with respect to the horizontal axis, in radians; a ray emerging from the focal point is $\begin{bmatrix} r_1 \\ r_1' \end{bmatrix}=\begin{bmatrix} 0 \\ r_1' \end{bmatrix}$. For a ray travelling a horizontal distance d in a homogeneous medium towards the parabolic reflector East, the ray matrix is given by

$$\begin{bmatrix} 1 & d \\ 0 & 1 \end{bmatrix}$$

Referring to the above, the distance d=$f \cos r_1'$. The matrix for a parabolic reflector with focal length F is given by

$$\begin{bmatrix} 1 & 0 \\ -1/f & 1 \end{bmatrix}$$

The ray reflected by the parabolic reflector travels a distance d_{EW} to the west antenna. The ray matrix is given by

$$\begin{bmatrix} 1 & d_{EW} \\ 0 & 1 \end{bmatrix}$$

And the ray then hits the West parabolic reflector. The ray matrix for the complete system can be written as (4).

$$\begin{bmatrix} 1 & d \\ 0 & 1 \end{bmatrix} \begin{bmatrix} 1 & 0 \\ -1/f & 1 \end{bmatrix} \begin{bmatrix} 1 & d_{EW} \\ 0 & 1 \end{bmatrix} \begin{bmatrix} 1 & 0 \\ -1/f & 1 \end{bmatrix} \begin{bmatrix} 1 & d \\ 0 & 1 \end{bmatrix} \begin{bmatrix} r_1 \\ r_1' \end{bmatrix} = \begin{bmatrix} r_2 \\ r_2' \end{bmatrix} \quad (4)$$

Matrix multiplication results in

$$r_2 = r_1' \left(d - d_{EW} - d \left(\frac{d}{f} + 1 - \frac{1}{f} \left(d - d \frac{d_{EW}}{f} + d_{EW} \right) \right) \right) \quad (5)$$

And

$$r_2' = r_1' \left(-\frac{d}{f} + 1 - \frac{1}{f} \left(d - d_{EW} \frac{d}{f} + d_{EW} \right) \right) \quad (6)$$

Using $f = 0.5m$, r_1'=0.5 rad (30°), and d_{EW}=10m as an example, from (5) and (6) r_2 =0, and r_2'=-0.5 rad are obtained. This means that the beam converges back at the focal point of the receiving dish. Since the signal at the focal point of receiving dish is the same size as it was when transmitted by the East transmitter, the receiver array must be placed at the focal point of the receiving dish. Although the distance between each parabolic reflector d_{EW} has been determined to be 10m here, this is true for any distance between the reflectors, and for any input angle r_1' less than the curvature angle θ_o of the dish.

5.3.2 Full Duplex System Simulation in HFSS

The system is constructed and simulated using HFSS (shown in fig. 5.6) to verify that the antennas and signal collimation do, in fact, work. The parabolic dish antenna design described in the previous section was constructed in HFSS, with f=0.4m and D=1m. The antenna arrays are placed at the focal point of the East dish antenna, and the received signal is observed at the focal point of the West dish, where the receiver array must be positioned. The inner and outer arrays are independently excited, to determine the collimation of both. Both instances in which the

signal is received at the focal point of the West antenna are presented in fig. 5.7 and fig. 5.8. The results show that the OAM beam is recreated at approximately the same as its original size, at the focal point of the West antenna, as predicted by the ray tracing method. The same scale is used for both plots, with the red color denoting the highest field strength and the blue color representing the lowest. A donut shape is observed in both cases. However, the signal received is more oval in shape than circular. These slight aberrations in the shape and intensity of the received signal are observed as compared to those of the transmitted signal. This may be because the beam converges at a position offset from the theoretical focal point of the West dish. Moreover, the signal undergoes attenuation as it travels the propagation distance between the two parabolic reflectors. It is also important to note the difference between the received signals when the inner and outer arrays are excited. A more well-defined donut shape is observed in the output when the outer array is excited, compared to the shape observed in the output when the inner array is excited. One explanation for this is that the dish was designed according to the divergent angle of mode 5 of the outer array and may not produce the same output for all arrays and all modes with varying divergent angles. However, a distinct OAM shape is recovered at the receiver for all modes.

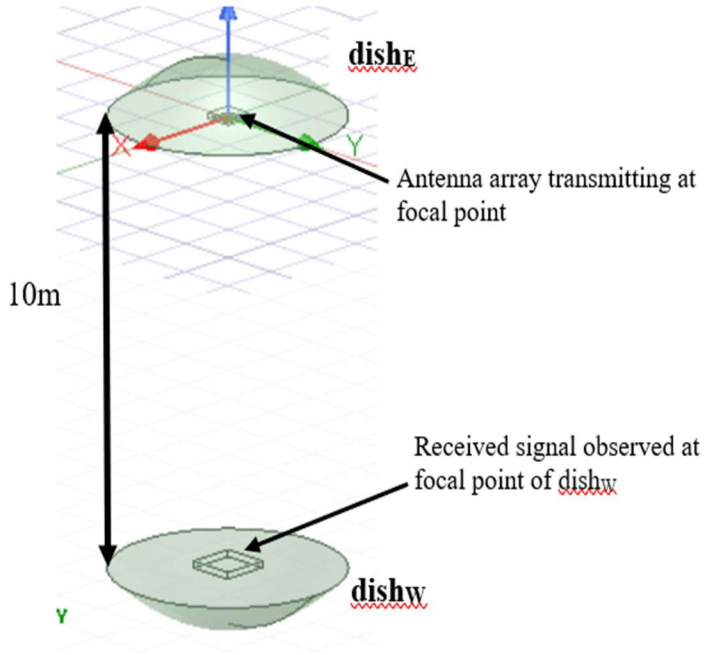

Figure 5.6 HFSS setup showing the antenna system created using the antenna arrays at the East and West ends, with parabolic antennas used at each end to collimate the signals

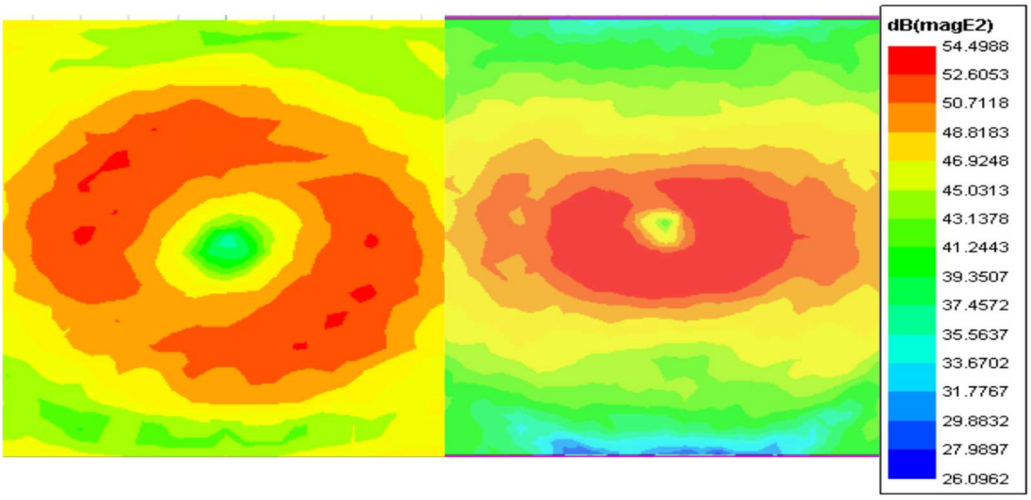

Figure 5.7 The signal transmitted by the inner array mode *l*=1 (left), and the signal at the focal point of the West dish antenna (right).

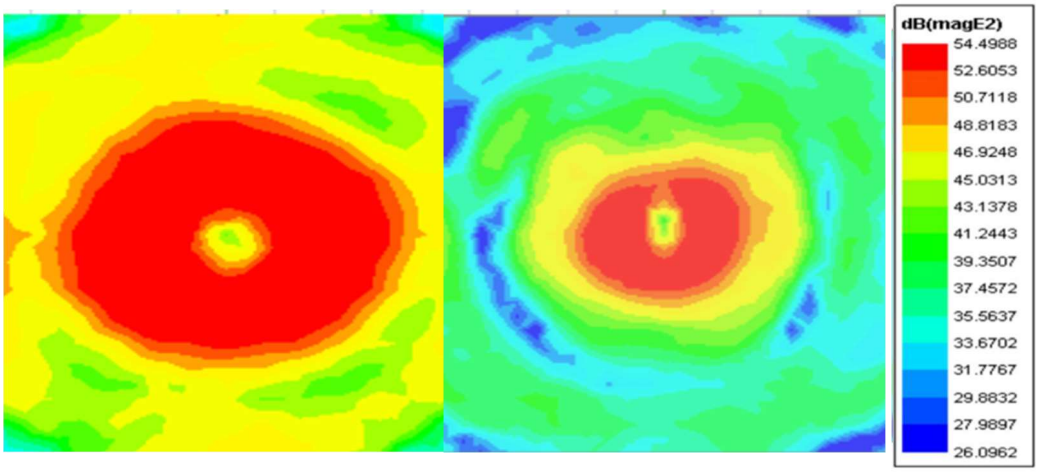

Figure 5.8 The signal transmitted by the outer array mode *l*=1 (left), and the signal at the focal point of the West dish antenna (right).

5.4 Received Power Measurement

A theoretical study is carried out to establish the relationship between the coupling between the East and West antennas and the OAM mode of the receiver, in the full duplex system presented in fig. 5.6. The purpose of this study is to demonstrate the general trend of the coupling between two antennas with different OAM modes, when one is used as a transmitter and the other as a receiver. The results of this study offer a better understanding of the crosstalk calculations used for the local transmitter and receiver arrays, which will be examined in the next section.

The system design featured in fig. 5.6 is simulated in HFSS, with a receiver array placed at the focal point of the West dish antenna. In this study, the outer array at the East end is used to transmit an OAM mode l=+1, and the outer array at the West end is used as a receiver antenna. The OAM mode of the receiver array is varied from -5 to +5, while the transmitter mode remains fixed at l=+1.

It is important to note that the OAM mode polarity of an antenna is defined with respect to the direction of propagation of the antenna's signal. With the direction of propagation pointing outwards, if the phase of the input signal is increasing clockwise around the azimuth, then the OAM wave generated is a mode l=-1, and if it is increasing in a counterclockwise direction, then the mode of the OAM wave generated is l=+1. In the case of the full duplex system, the two transmitter and receiver arrays at the East and West ends are facing in opposite directions and therefore have opposite directions of propagation. Consequently, using the direction of propagation of one antenna as a point of reference would supply the incorrect polarity for the other array. To avoid confusion, in this study, the polarity of the OAM mode of each antenna is defined with respect to the direction of propagation of the antenna of interest. Therefore, the

OAM polarity of the East antenna is determined using the +z direction as reference, whereas the OAM polarity of the West antenna is determined using the -z direction as reference.

Since the purpose of the study is to observe the effect of receiver mode on power coupling between the East and West antennas, the distance between the antennas is not a contributing factor in the investigation and is kept at a fixed value of 10m. ANSYS Circuit is employed to construct the feeding network, which configures the mode of the antenna arrays. The circuit schematic is depicted in Fig. 5.9 below.

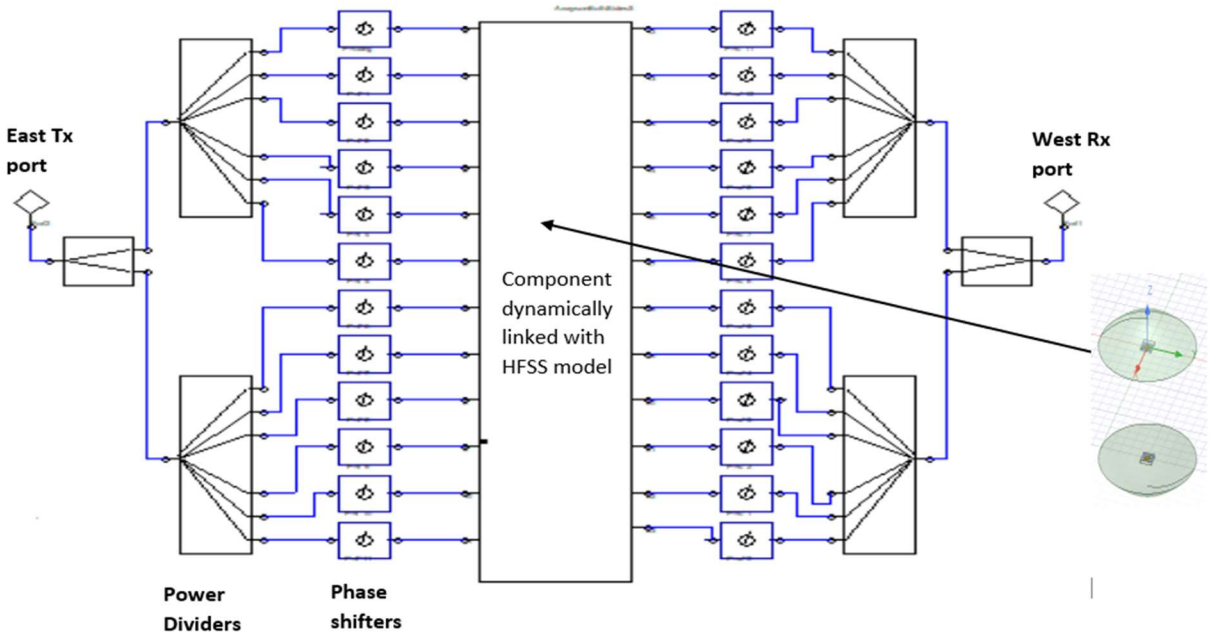

Figure 5.9 Circuit schematic used to determine the coupling between the East and West antennas for different modes of the West receiver

Fig. 5.10 presents the results obtained for the power coupling $S12_{E\text{-}W}$ between the East and West antennas against the mode of the receiver antenna. The graph confirms that the

coupling is at its maximum (-21dB) when the receiver has the same OAM mode as the transmitter, i.e., l=+1. Furthermore, the values of S_{12} for negative modes are lower than the values for positive modes, indicating that coupling is lower when the transmitter and receiver have mismatched OAM polarity. The graph also shows that the coupling gradually decreases as the positive OAM modes are increased. However, for negative OAM modes, the coupling is relatively higher for odd modes as compared to even receiver modes. Specifically, the coupling is -42dB for l=-3, and -49dB and -51dB for modes l=-2 and l=-4, respectively. This anomalous trend may be indicative of a higher orthogonality between transmitter mode +1 and negative even OAM modes, as compared to negative odd modes. It may also be contributed by noise.

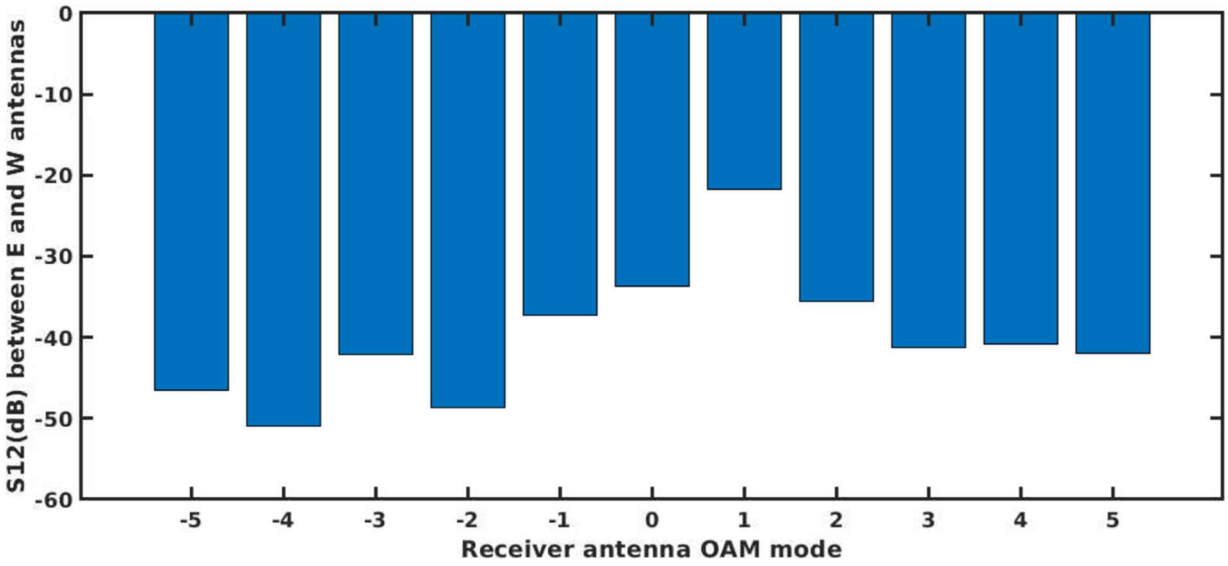

Figure 5.10 Coupling between the outer arrays of East and West antennas, separated by a distance of 10m, is determined as $S12_{E\text{-}W}$ in HFSS

5.5 Crosstalk Measurement

The results of the previous section verified that when the transmitter and receiver modes are mismatched, a low power output is received at the West end. Therefore, it can be inferred that in the antenna system exhibited in fig. 5.1, where the local antennas are in close proximity to one another, there is low coupling between the local antennas when they have non-equal OAM modes. However, it must be ensured that the crosstalk power leaking from the transmitter to the local receiver is lower than the power received from the transmitter at the other end. A low crosstalk would allow the inner and outer arrays to operate simultaneously, one as a receiver and the other as a transmitter, thereby making this configuration useful in full duplex systems.

To determine the crosstalk between the inner and outer arrays, the antenna setup in fig. 5.1 is modelled in HFSS, with both antennas being placed on a common substrate. The HFSS model is included as a component in ANSYS Circuit. The inner array consisting of 8 patches is connected to the transmitter network in the ANSYS Circuit, as described before. Since there are 8 patches, a 45° phase shift between the signals feeding adjacent patches is required for the array to transmit a mode of l=+1. The transmit signal is divided into 8 equal signals by a power-divider, and the phase shifts are provided by the 8 phase-shifters in the transmitter network. The circuit schematic is shown in fig. 5.11. The first 12 pins of the component representing the HFSS model symbolize the connections to the 12 ports of the outer array. The signal collected by each patch antenna in the outer receiver array is sent to the receiver network, which consists of 12 phase-shifters and a power-divider. Each phase-shifter increases the phase of the signal, in the clockwise or counterclockwise direction, so as to create a total phase shift of 360° over the entire array. Therefore, the phase-shifters are used to configure the mode of the OAM antenna. The mode of the outer array is varied from l=-5 to l=+5 by altering the receiver phase shifts. The 12

phase-shifted signals are then combined using a power- combiner, and the resulting signal is obtained at the receiver port. The S_{12} value between the transmitter and receiver ports indicates the ratio of the transmitted signal when coupled to the local receiver. The value of $S12_{local}$ is determined for each mode of the receiver. This is the crosstalk between the inner and outer arrays.

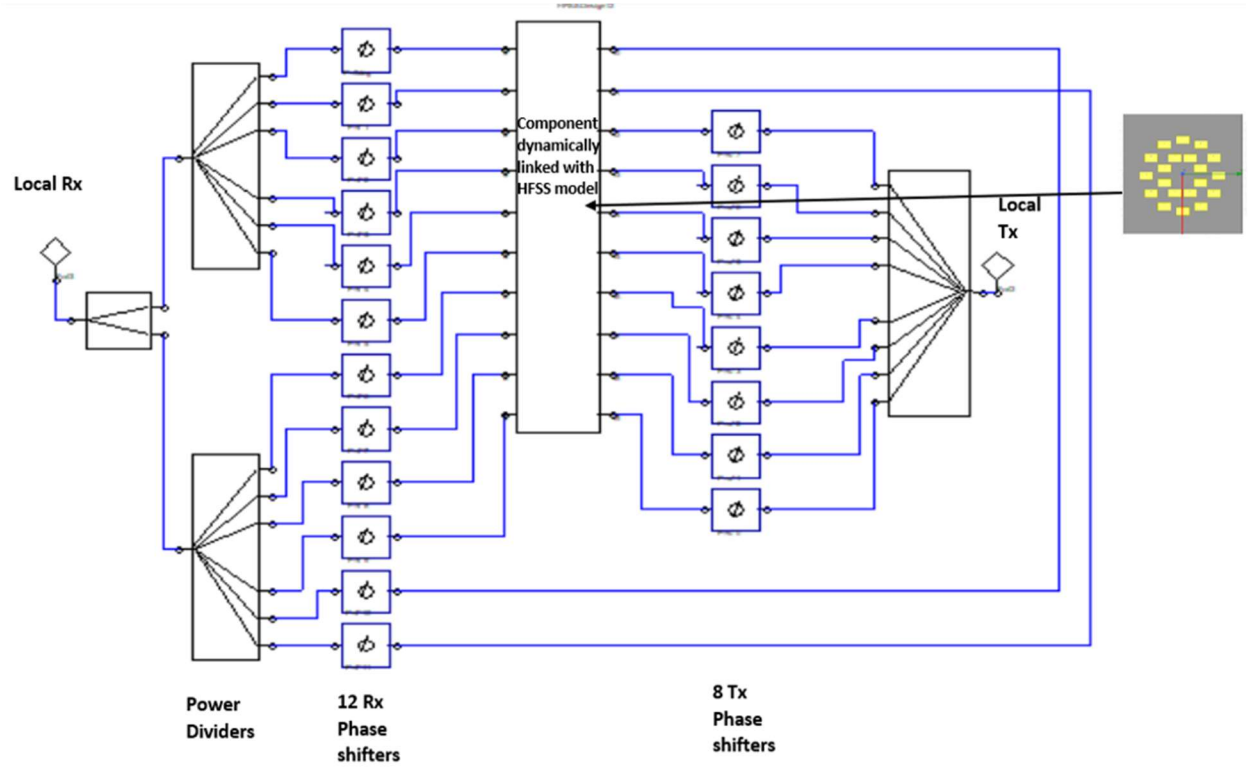

Figure 5.11 Circuit schematic created in ANSYS Circuit to determine the crosstalk S_{12} between the inner and outer OAM antennas

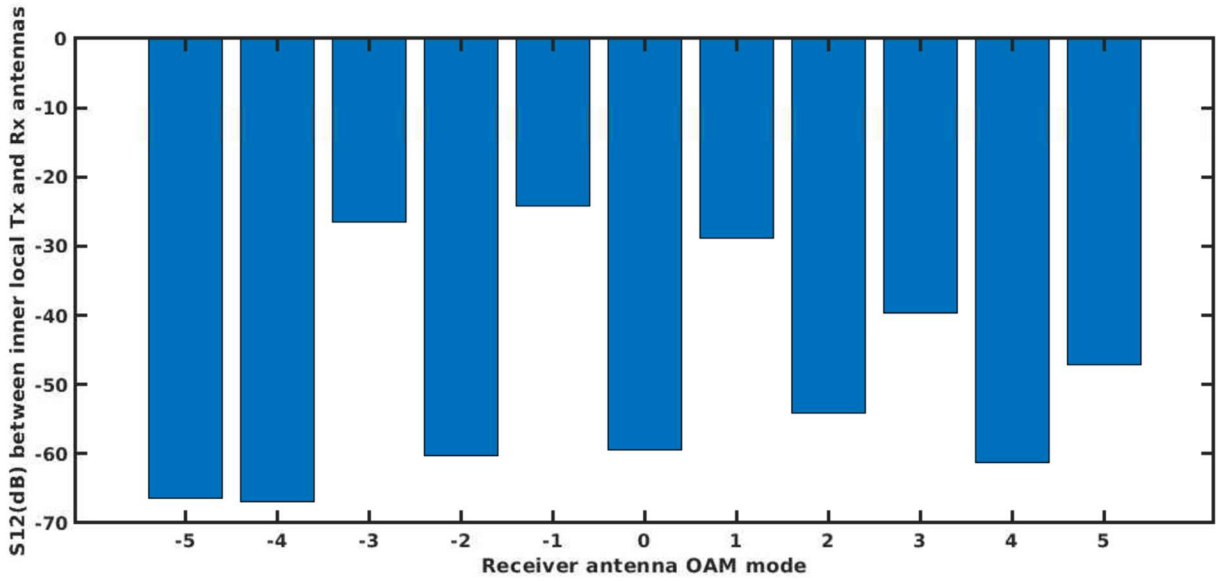

Figure 5.12 Crosstalk coupling $S12_{local}$ between local transmitter and receiver antennas in a nested design modelled in HFSS

The results showing the variation in crosstalk $S12_{local}$ between local transmitter and receiver and OAM mode of the receiver are graphed in fig. 5.12. In this study, both antennas have the same direction of propagation, so the polarity of the OAM mode is determined with respect to the same propagation direction. Therefore, as expected, the maximum crosstalk power of -24dB is obtained for receiver mode l=-1. Additionally, a high crosstalk is observed for l=-3, specifically -26.5dB. And the crosstalk for mode l=+1 is also noteworthy, at -29dB. While the crosstalk for all other modes is less than -30dB, it is essential to note a prominent trend in the crosstalk values for odd and even receiver modes. The crosstalk is significantly higher for odd modes compared to even modes; note the $S12_{local}$ = -60dB for l=-2 and $S12_{local}$ = -26.5dB for l=-3. Although a similar trend was noted in fig. 5.10 for the power coupling between East and West antennas, such behavior is more pronounced in the case of local antennas, possibly due to the

local antennas being in closer proximity. The graph is suggestive of a lower crosstalk and a higher orthogonality between even-odd OAM pairs, which is a significant finding and a useful factor to consider when selecting the modes for the inner and outer arrays.

5.6 Link Budget

The results of crosstalk measurement show that the antenna setup in fig. 5.1 provides appreciable isolation between local transmitter and receiver antennas, especially when the outer receiver array has an even mode. This makes it a good choice for use in a full duplex system. For reference, the link budget of such a full duplex system may be plotted for both odd and even receiver modes. The link budget provides a good estimate of the propagation distance the signal may travel before the signal strength falls below the power of the local transmitter.

Consider the example of a full duplex system consisting of nested antenna systems on the East and West sides, separated by a distance. If the outer array has a mode l=-2, and the inner array has a mode l=+1, the isolation between the arrays is -60dB (see fig. 5.12). The full duplex system has a launch power Pt of 85dBm, and a receiver sensitivity of -120dB. As discussed in the previous section, an OAM signal diverges as it propagates. Therefore, to collimate the OAM signal, a dish antenna is used at each end. The ray diagram of such a system is illustrated in fig. 5.5. The dish antenna has a gain of 30dB, which is included in the 85dBm launch power. The crosstalk coding isolation provided by digital signal processing and analog cancellation is estimated to be 90dB [95]. OAM isolation of 60dB between outer antennas with a mode of -2 and inner antennas with a mode of +1 reduces the crosstalk to -95B. The crosstalk signal, when the receiver mode is -2, is represented in red in the graph featured in fig. 5.13 and is independent of the distance travelled by the wave, since it is the power transfer between the local transmitter and receiver antennas. If the mode of the outer array is instead selected as l=-3, the isolation

between the arrays is -27dB (refer to fig. 5.12), and the crosstalk transmitted to the receiver is reduced to -62dB (represented in green in fig. 5.13), after accounting for the isolation provided by OAM orthogonality, and the crosstalk coding methods.

For the receiver antenna to successfully collect the signal transmitted by a distant antenna, the signal power at the receiver must be higher than the crosstalk from the local transmitter. Since the power of the signal attenuates due to free space loss as it travels through the air, the distance between the two antennas in a full duplex system is limited by the crosstalk power at the receiver. The power of the signal from a distant transmitter, arriving at the receiver, is calculated using (1)[96].

$$\frac{P_r}{P_t} = N g_t \left(\frac{4\pi(\pi {R_t}^2)}{\lambda^2}\right) N g_r \left(\frac{4\pi(\pi {R_r}^2)}{\lambda^2}\right) \left(\frac{\lambda}{4\pi D}\right)^4 \qquad (1)[96]$$

In the above equation, N is the number of elements in the antenna arrays; gt and gr are the antenna gains of each patch and are taken as 1; Rt and Rr are the array radii of the transmitter and receiver, respectively, and are taken as 60mm for the outer arrays; λ is the wavelength 53mm; and D is the distance between the antennas. The distance D is varied to determine the power of the signal as it propagates. The received power against the distance is plotted in blue in fig. 5.13 for the outer array as a function of the distance D. At the receiver, a dish antenna gain of 30 dB is added to the signal power . A comparison of the plot for the received power (blue) and the plots for the two instances of crosstalk (red and green) illustrates the distance the signal can travel before it falls below the crosstalk value. For an outer array with an OAM mode of l=-3, there is a significant margin of received power over crosstalk—for a distance up to 2km. For an outer array with a mode of l=-2, the distance is up to 10km. Therefore, an extra 8km of communication distance can be achieved by configuring the outer array with a mode of l=-2.

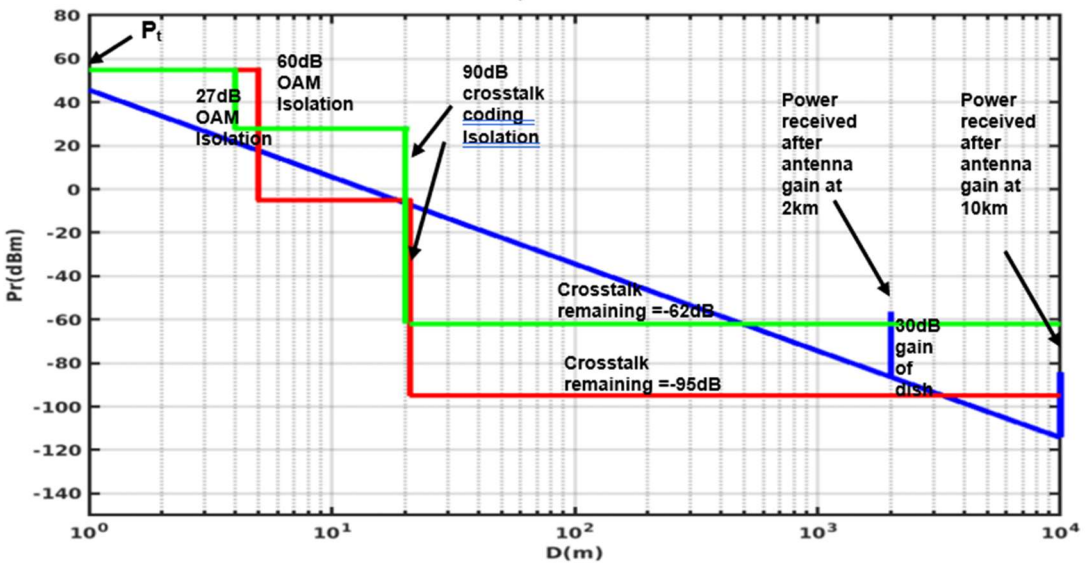

Figure 5.13 The strength of the signal transmitted by the outer array as it propagates a distance D (blue), and crosstalk values for receiver mode *l*=-2 (red) and receiver mode *l*=-3 (green), both of which are independent of distance

5.7 Conclusion

This chapter explored the mechanics behind a nested antenna design, as well as the benefits associated with it. The antenna setup consists of transmitter and receiver arrays placed concentrically on the same substrate. The array radii for the inner and outer antennas were selected so as to accommodate both arrays on the same substrate. The nested design is compact and practical, particularly for use in a full duplex system, as both the transmitter and receiver arrays utilize the same space. Moreover, both local antennas can use the same dish antenna, unlike the design with adjacent antennas. The present chapter examined this setup in terms of OAM orthogonality and crosstalk reduction, in particular. An OAM signal diverges as it propagates; therefore, for the two antenna systems to communicate in a full duplex system, parabolic dish antennas are employed to collimate the signal. The dish antenna design parameters

were also discussed, and the selection of these parameters with regard to the angles of divergence for the OAM signals was described. The communication between two distant antennas on the East and West side in a full duplex setup was studied through two methods, ray matrices and HFSS simulation. A study was simulated in HFSS to model the communication between two distant antennas on the East and West side, by fixing the mode of the transmitting array on the East end to +1, and by the varying the OAM mode of the receiving array on the West end. It was shown that the highest power is received when both the transmitting and receiving arrays have the same OAM mode, and in general, the power decreases as the mode of the receiver increases.

Another study was carried out to determine the crosstalk between the inner and outer arrays in a nested antenna design. The antenna arrays were modelled in HFSS, and the crosstalk was studied by fixing the OAM mode of the inner array to +1, and by varying the mode of the outer array. Results showed a high crosstalk when the receiver array has an odd OAM mode. The results indicate a higher orthogonality of odd-even OAM pairs.

The numerical calculations confirm that an even OAM mode would be a good choice for the outer array. Link budget calculations show that an appreciable distance of 2km can be achieved for signal propagation when the outer array is an odd mode, and a communication distance that is further 8km can be achieved by selecting an even OAM mode for the receiver.

Chapter 6

CROSSTALK-INDUCED VOLTAGE IN NESTED RING ANTENNAS

The previous chapter demonstrated the high isolation provided by the nested antenna design, which is both compact and practical. Previous analysis of the geometry was carried out using phased array antennas, in HFSS. The purpose of this chapter is to analyze the antenna system to derive a mathematical expression for the voltage induced in the outer receiver due to the crosstalk signal generated by the inner transmitter. This chapter is divided into two parts. In the first part, the mathematical expression is numerically derived to calculate crosstalk. In the second part, the results are verified through HFSS simulation of two concentric loop antennas configured to operate as OAM antennas.

6.1 Mathematical Derivation from Analytical Modeling

The antennas presented in fig. 5.1 are modeled analytically to study their operation mathematically. Fig. 5.1 shows two concentric OAM antennas, each consisting of a circular array of patch antennas. The signal to each patch of the antenna array is phase-shifted from the adjacent patch to generate the required OAM mode. In the analytical model presented in this chapter, each circular array is modelled by a circular loop antenna excited by a short pulse of current that travels around the loop. In a manner similar to the phased array, the phase of the current varies along the loop, resulting in radiation of fields carrying OAM. In general, the current distribution on the inner loop antenna will induce a voltage on the outer loop, and this induced voltage may be interpreted as crosstalk.

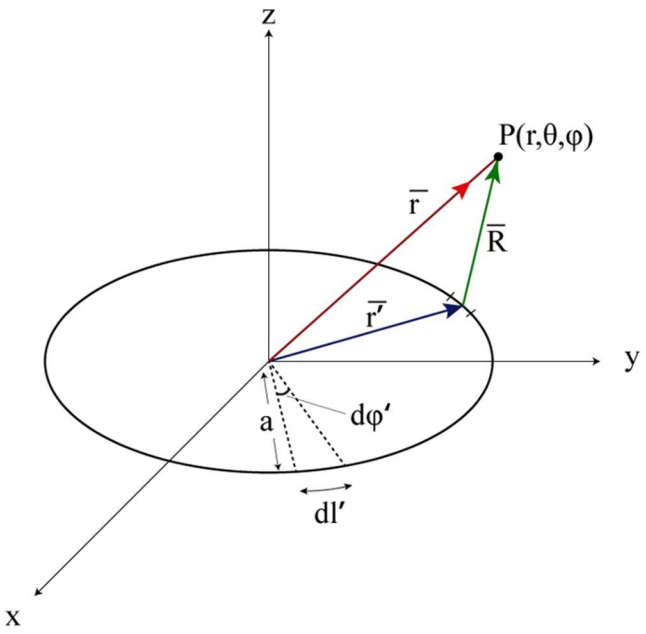

Figure 6.1 The inner loop antenna is comprised of a wire shaped in a circle with a radius of a. The source coordinates are denoted by (r',θ',φ'), whereas (r,θ,φ) refers to any observation point.

Inner Loop (Transmitter)

The inner loop is modelled first, as a thin wire shaped as a circle with a radius of *a*, as shown in fig. 6.1. For convenience, the circle is placed at the origin on the x-y plane. The coordinates of the inner loop are described using the spherical coordinate system $(\boldsymbol{r'}, \boldsymbol{\theta'}, \boldsymbol{\varphi'})$, whereas any observation point uses the coordinate system $(\boldsymbol{r}, \boldsymbol{\theta}, \boldsymbol{\varphi})$**.**

The current flow in the wire is a constant current I_o, and the phase varies along the azimuthal angle φ, comparable to the phase shift in phased array antennas. Therefore, the current distribution in the loop may be represented as $\boldsymbol{I} = I_o e^{-jl\varphi'} e^{-j\omega t} \widehat{\boldsymbol{a}_{\boldsymbol{\varphi}}}$**,** where I_o is the constant current amplitude, l is the OAM mode number, ω is the angular frequency, and t is the time. The

term $e^{-j\omega t}$ depicts the time variation of the signal, and the term $e^{-jl\varphi'}$ marks the phase shift in the signal and varies with the angle φ'. Consequently, for every 2π revolution of φ', the phase of the current undergoes an $l(2\pi)$ phase shift. Hence for *l*=1, there is a total phase shift of 2π in a complete revolution around the circle. For *l*=2, the total phase shift is 4π, and for *l*=3, it is 6π. Previous chapters have shown that such a phase shift variation in the signal in the azimuthal direction, causes the generation of OAM carrying electromagnetic waves. For the mathematical analysis of the fields generated by the current flow in the loop, the standard approach involves determining the vector potential **A,** and then using it to calculate the electric and magnetic fields.

To simplify the problem, it is assumed that the loop is made up of an infinite number of small segments, all of length *dl.* Then, the vector potential **A**(**r**), at an observation point P, can be written in the same way as for a linear dipole [97]:

$$\boldsymbol{A}(\boldsymbol{r}') = \frac{\mu}{4\pi}\int \frac{I(\boldsymbol{r}')e^{-ikR}}{R}dl' \quad (1)$$

Here, μ is the permeability of air, and k is the wave number provided by $k = \frac{2\pi}{\lambda}$. As indicated in fig. 6.1, $\boldsymbol{R} = \boldsymbol{r} - \boldsymbol{r}'$ and $dl' = ad\varphi'$, **r** is the vector from the origin to any point on the inner loop; $\boldsymbol{r}'$ is the vector from the origin to any observation point; and **R** is the vector from a point on the loop to any observation point. The infinitesimal dipole approximation [77] ($|r - r'| \approx r - a\sin\theta\cos(\varphi - \varphi')$ for phases, and $|r - r'| \approx r$ for amplitudes) can be used to simplify the expression in (1) as [77]:

$$\boldsymbol{A}(\boldsymbol{r}) = \frac{\mu I_o a}{4\pi}\int_0^{2\pi} \frac{e^{-j\omega t}e^{-il\varphi'}e^{-ik(r-a\sin\theta\cos(\varphi-\varphi'))}}{r}(-\hat{\boldsymbol{x}}\sin\varphi' + \hat{\boldsymbol{y}}\cos\varphi')d\varphi'$$

The integration over the azimuth angle from 0 to 2π combines the contribution of each small segment of the loop, and provides the complete vector potential of the entire loop.

Defining the difference $\varphi - \varphi' = \emptyset$ for simplifying the integration, the above equation may be re-written as follows

$$A(\boldsymbol{r}) = \frac{\mu I_o a}{4\pi} \int_0^{2\pi} \frac{e^{-j\omega t} e^{-il\varphi} e^{il\emptyset} e^{-ik(r - a\sin\theta \cos\ (\emptyset))}}{r} (-\hat{\boldsymbol{x}}\sin\varphi' + \hat{\boldsymbol{y}}\cos\varphi') d\emptyset$$

Bessel's first integral is given by [75] $J_n(z) = \frac{1}{2\pi i^n} \int_0^{2\pi} e^{-jn\theta} e^{-iz\cos\theta}\, d\theta$

Therefore, the integration in the above equation can be simplified as [75]

$$\int_0^{2\pi} e^{il\emptyset} e^{ka\sin\theta\cos(\emptyset)}\, d\emptyset = 2\pi i^n J_l(ka\sin\theta)$$

The results of the integration, in terms of spherical coordinates, are obtained from [77]:

$$\boldsymbol{A}(\boldsymbol{r}) = \frac{j^{-l}\mu a\ _o e^{-ikr} e^{-il\varphi}}{4r} [(\hat{\boldsymbol{r}}\sin\theta + \hat{\boldsymbol{\theta}}\cos\theta - \hat{\boldsymbol{\varphi}}j) J_{l-1}(ka\sin\theta) + (\hat{\boldsymbol{r}}\sin\theta + \hat{\boldsymbol{\theta}}\cos\theta - \hat{\boldsymbol{\varphi}}j) J_{l+1}(ka\sin\theta) \qquad (2)$$

Here, $J_n(ka\sin\theta)$ is a Bessel function of the first kind, and $ka\sin\theta$ is the variable of the Bessel function. The magnetic field **H** is derived from the vector potential using Maxwell's equation (3):

$$\boldsymbol{H} = \frac{1}{\mu}\nabla \times \boldsymbol{A} \qquad (\mathbf{3})$$

Due to the symmetry of the problem with respect to the z axis, the cylindrical components of the magnetic and electric fields are calculated. The resulting components of $\mathbf{H}(H_\rho, H_\varphi, H_\mathbf{z})$ are provided by [77],

$$H_\rho = -\frac{C}{2}\cos\theta\, e^{-i\omega t}e^{-ikr}e^{-il\varphi}\left\{\frac{k}{r}(J_{l-1}+J_{l+1})+\frac{j}{r^2 l}[l^2-(ka\sin\theta)^2](J_{l-1}+J_{l+1})\right\} \quad (4)$$

$$H_\varphi = \frac{C}{2}e^{-i\omega t}\cos\theta\, e^{-ikr}e^{-il}\ \ p[\frac{jk}{r}(J_{l-1}+J_{l+1})+\frac{l}{r^2}(J_{l-1}-J_{l+1})] \quad (5)$$

$$H_\mathbf{z} = \frac{C}{2}e^{-i\omega t}\sin\theta\, e^{-ikr}e^{-il\varphi}\left\{\frac{k}{r}(J_{l-1}-J_{l+1})-\frac{j}{r^2 l}(J_{l-1}+J_{l+1})[l^2+(ka)^2-(ka\sin\theta)^2]\right\} (6)$$

where C is defined as $C = -j^{-l}a\frac{I_o}{2}$, $r = \sqrt{\rho^2+z^2}$, and $\sin\theta = \frac{\rho}{\sqrt{\rho^2+z^2}}$ [77]. The electric field **E** is similarly derived from **H** using (7).

$$\boldsymbol{E} = \frac{1}{j\omega\varepsilon}\nabla\times\boldsymbol{H} \qquad (\mathbf{7})$$

The cylindrical field components of E are obtained as follows [77]:

$$E_{\boldsymbol{\rho}} = \frac{C}{2\omega\varepsilon}e^{-i\omega t}e^{-ikr}e^{-il\varphi}\left\{\frac{jk^2\cos^2\theta}{r}(J_{l-1}+J_{l+1})+\frac{k}{r^2}[l\cos 2\theta\,(J_{l-1}-J_{l+1})-\sin^2\theta(J_{l-1}+J_{l+1})]\right\} \quad (8)$$

$$E_\varphi = \frac{C}{2\omega\varepsilon}e^{-i\omega t}e^{-ikr}e^{-il\varphi}[\frac{k^2}{r}(J_{l-1}-J_{l+1})-\frac{jlk}{r^2}(J_{l-1}+J_{l+1})] \quad (9)$$

$$E_z = -\frac{C}{2\omega\varepsilon}\sin\theta\cos\theta\, e^{-i\omega t}e^{-ikr}e^{-il\varphi}\left\{\frac{jk^2}{r}(J_{l-1}+J_{l+1})+\frac{k}{r^2}[(J_{l-1}+J_{l+1})+2l(J_{l-1}-J_{l+1})]\right\} \quad (10)$$

The phase of the electric field for l=1 is plotted on a circular plane (fig. 6.2), 50m above the loop to verify that the signal generated by the loop antenna is, in fact, an OAM signal. The phase pattern is a rotating spiral phase front, as is expected for an OAM signal with a mode l=1.

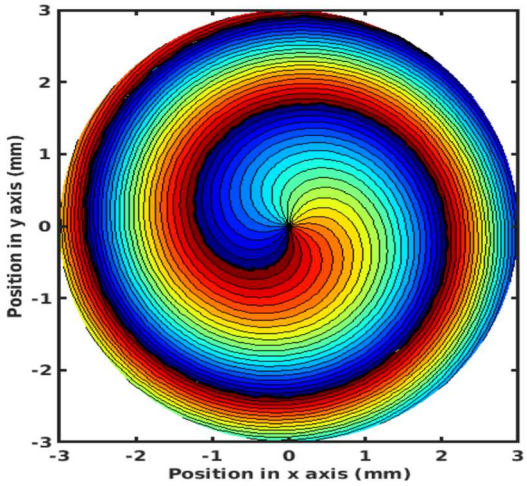

Figure 6.2 The phase pattern of the electric field generated by the loop antenna with a mode *l*=1

Outer Loop (Receiver)

To test the nested antenna design featured in fig. 5.1, an outer receiver antenna is modelled using another wire loop with a radius of r_1 and greater than a. The outer loop is placed in the field of the inner loop, on the same horizontal plane as the inner loop. The centers of both loops are at the origin. The AC current in the inner loop results in a time-varying term in the electric and magnetic fields. According to Faraday's law, the changing magnetic flux induces an electric current in any closed loop placed in the field. The changing magnetic field produced by the current in the inner loop can be determined at any point on the outer loop using equations (4)-(6). Due to the position of the outer loop, z=0 and $\theta = 90°$ can be substituted in the equations to determine the field distribution **H** on the outer loop. Faraday's law (11)[98] is applied to

determine the amount of voltage induced by the outer conductor, wherein B represents the magnetic flux density.

$$\nabla \times \boldsymbol{E} = -\frac{\partial B}{\partial t} \qquad (11)$$

Using Stoke's Theorem [98] (11), this relationship can be written as,

$$\oint \widetilde{\boldsymbol{E}} \cdot \widetilde{\boldsymbol{dl}} = -\int \frac{\partial}{\partial t} \widetilde{\boldsymbol{B}} \cdot \widetilde{\boldsymbol{dS}} \qquad (12)$$

In the above equation *dS* represents an infinitesimally small area of the outer loop, which can be defined as, $dS = \frac{r1^2 d\varphi}{2}$. The quantity on the left-hand side of the equation is the induced emf, measured in Volts. The right-hand side can be further expanded as

$$V = -\mu \frac{\partial}{\partial t} \int \left(H_\rho \widehat{\boldsymbol{a_\rho}} + H_\varphi \widehat{\boldsymbol{a_\varphi}} + H_z \widehat{\boldsymbol{a_z}}\right). \widehat{a_z} \frac{{r_1}^2 d\varphi}{2} \qquad (13)$$

The equation reduces to

$$V = -\mu \frac{\partial}{\partial t} \int H_z \frac{{r_1}^2 d\varphi}{2} \qquad (14)$$

Given the position of the outer loop, z=0 (therefore $\theta = \frac{\pi}{2}$ and r=ρ in spherical coordinates), and ρ=r_1 can be substituted in (6) so that the expression for H reduces to

$$H_{\boldsymbol{z}} = \frac{C}{2} e^{-i\omega t} e^{-ikr_1} e^{-il\varphi} \left\{ \frac{k}{r1} (J_{l-1} - J_{l+1}) - \frac{jl}{r1^2} (J_{l-1} + J_{l+1}) \right\} \qquad (15)$$

Therefore, (14) can be written as

$$V = -\mu \frac{\partial}{\partial t} \int e^{-i\omega t} \left(\frac{C}{2} e^{-ikr_1} e^{-il\varphi} \left\{ \frac{k}{r_1} (J_{l-1} - J_{l+1}) - \frac{jl}{{r_1}^2} (J_{l-1} + J_{l+1}) \right\} \frac{{r_1}^2 d\varphi}{2} \right)$$

Performing the time differentiation, and setting the limits of the integral from 0 to φ, allows one to determine the voltage at any point at an angle φ along the azimuth, using the following equation:

$$V = j\omega\mu \int_0^{\varphi} e^{-i\omega t}\left(\frac{C}{2} e^{-ikr_1} e^{-il\varphi} \left\{\frac{k}{r_1}(J_{l-1} - J_{l+1}) - \frac{jl}{{r_1}^2}(J_{l-1} + J_{l+1})\right\} \frac{{r_1}^2 d\varphi}{2}\right) \quad (16)$$

Ignoring the time variation, all terms in equation (16) are constant, except φ. Assuming the product of all the constant terms as a constant V_{o2}, the equation reduces to

$$V = V_{o2} e^{-i\omega t} \int_0^{\varphi} (e^{-il\varphi} d\varphi) \quad (17)$$

The expression for the induced voltage reveals a magnitude term that remains constant at all points on the outer loop. The magnitude V_{o2} is dependent on the position and radius of the outer loop, as well as the radius and mode of the inner loop. More importantly, (17) indicates the azimuthal dependence of the phase. The phase term $e^{-il\varphi}$ specifies that the phase of the signal increases by $l\varphi$ for every φ, under which circumstances, there would be a total phase shift of $l(2\pi)$ in one revolution around the loop. This implies that an OAM signal was induced in the outer loop.

Furthermore, due to the OAM nature of the receiver antenna, the outer loop imparts an additional phase shift to the signal as it travels through the loop. This phase shift is dependent on the OAM mode l_1 of the outer loop and varies in the φ direction. The signal at each point in the outer loop can then be added together to calculate the combined received output. Therefore, (17) becomes

$$V = V_{o2}e^{-i\omega t}\int_0^{2\pi}(e^{-il\varphi}e^{-il_1\varphi}d\varphi) = V_{o2}e^{-i\omega t}\int_0^{2\pi}(e^{-i(l+l_1)\varphi}d\varphi) \quad (18)$$

Under these circumstances, l_1 is the mode of the outer receiver loop and $-il_1\varphi$ is the phase shift at each point of the outer loop. The phase term $e^{-i(l+l_1)\varphi}$ means that the signal undergoes a phase shift of 2π, l+l_1 times in one revolution around the loop. Therefore, l+l_1 is the mode of the received signal (see Appendix B). The integration in (18) may be performed to determine the total voltage induced in the receiver antenna.

$$V = V_{o2}e^{-i\omega t}\left[\frac{e^{-i(l+l_1)2\pi}-1}{-i(l+l_1)}\right] \quad (19)$$

Note that the term $e^{-i(l+l_1)2\pi}$ is always equal to 1 for all integer values of l and l_1 (with the exception of l+l_1 =0), and results in an induced emf V=0. This is an important finding because V=0 for all values of l and l_1 except l=-l_1 means that the coupling between all non-matching OAM antennas is 0. This finding supports the theory, that OAM modes are orthogonal, and therefore the coupling between them must ideally and theoretically be zero [59], [99]–[103].

In the case of l+l_1 =0 i.e l=-l_1, (18) may be written as

$$V = V_{o2}e^{-i\omega t}\int_0^{2\pi}(e^0 d\varphi) = 2\pi V_{o2}e^{-i\omega t}$$

This output leads to the conclusion that an induced voltage exists only when l+l_1 =0, and therefore l=-l_1. This means that emf is induced in the outer antenna only when the inner and outer antennas are matched. When the mode of the transmitter and receiver antennas are matched, the phase shifts of the receiver completely cancel out the phases of the transmitted signals, resulting in an OAM mode 0 or a plane wave [104] (see Appendix B), and power is received at the receiver port. It is

important to note that the polarity of the OAM mode is determined with respect to the direction in which the radiation is propagated, i.e., whether the phase of the signal around the antenna increases in a clockwise or counter-clockwise direction. In the event that both antennas are on the same plane, the polarity of both OAM antennas is determined with respect to the positive z direction.

To summarize, the results (18) may be written as

$$V = \begin{cases} 2\pi V_{o2} e^{-i\omega t} & for\ l = -l_1 \\ 0 & for\ l \neq -l_1 \end{cases} \qquad (20)$$

The values of the various parameters in (16) can be set to obtain a value of V_{o2} and calculate V for $l = -l_1$. Setting a=34mm and r_1=60mm as in the nested patch arrays from chapter 5, $I_o = 1$, $\mu = 1.25 \times 10^6 m\ kg\ s^{-2} A^{-2}$, and $l = 1$. The value is normalized with respect to the constant magnitude. The values of the normalized crosstalk S_{12} between the local antennas are represented in the graph in fig. 6.3.

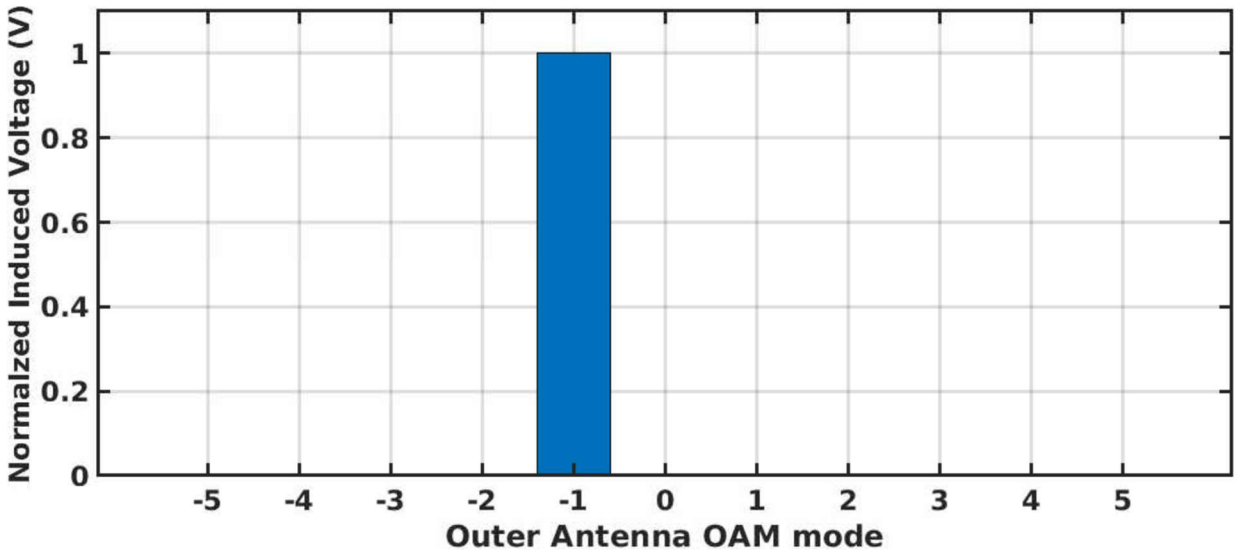

Figure 6.3 The voltage induced in the outer loop with the OAM mode of the receiver. Theoretically, power would be coupled to the receiver only if both OAM antennas have the same modes with opposite polarities

Fig. 6.3 shows an example of crosstalk values between the inner and outer OAM antennas for a transmitting antenna with mode l=1. The bar graph demonstrates that coupling between the inner and outer antennas occurs only if both antennas have the same OAM modes, but with opposite polarities l=-l_1, and is zero for all other OAM modes. This occurs due to the orthogonality of the OAM modes, and therefore the coupling between non-matching OAM modes is theoretically zero. This is an important concept and is the basis of this research. The derivation presented in this section is proof of the concept of orthogonality between the OAM modes, and moreover speaks to the advantage of using it in reducing crosstalk between local antennas. However, although the crosstalk between non-matching OAM modes is theoretically zero, previous chapters of this dissertation have demonstrated that, in practice, the crosstalk is not completely eliminated. The fact that OAM waves and phase shifts are not perfect, environmental effects, backward radiation, and noise—these are just some of the reasons that crosstalk between non-matching modes may be significant.

6.2 Simulation in HFSS

To verify the results of the derivation, a similar model was analyzed in HFSS. Two concentric waveguide loops were constructed to model the loop antennas. Previous studies have explored the use of travelling wave circular loop antennas (CLA) to generate OAM waves [35], [77], [78], [105]. Of these [78], also proposes a nested configuration of loop antennas for the purpose of multiplexing. However, there is not enough research on the isolation of CLA- based OAM antennas in a nested design. This section describes a nested CLA model based on the design demonstrated in [78]. The inner antenna is used as a transmitter with an OAM mode of l=+1, whereas the mode of the outer loop remains varied. To study the crosstalk between the inner and outer loops, the model is simulated in HFSS.

6.2.1 Waveguide Loop Antenna Design

The circular loop antenna with a radius *r* is made of a coaxial waveguide(fig. 6.4), excited by two ports that have an angular distance of λ/4 between them, where λ is the waveguide wavelength. The two signals that are fed to the ports are mutually orthogonal, and have an equal amplitude but a phase delay of ±90°, thereby ensuring a traveling wave current distribution [106]. As the signal propagates through the circular loop, it undergoes a phase shift that is dependent on the distance covered, which can be written as e^{-ikR}, where k is the wave number $\frac{2\pi}{\lambda}$ and λ is the effective wavelength in the waveguide. *R* is the circumferential distance covered, given by $r\varphi$. Therefore, the phase of the signal changes with the azimuth angle φ, and the circumference of the loop may be adjusted to cause the signal to undergo a total phase shift of $2\pi l$ in one revolution around the loop. Slots cut into the outer conductor of the OAM waves, allowing the waveguide to emanate electromagnetic radiation. The phase change in the current in the azimuth direction causes the electromagnetic waves emitted to assume helical phase fronts, and therefore carry orbital angular momentum. The mode of the OAM wave generated is dependent on the radius of the ring. The radius of the loop can be calculated by setting the phase shift over the circumference of the loop, to $2\pi l$. Since the circumference of the circle is $2\pi r$, the phase shift due to propagation over the complete circumference is $e^{-ik(2\pi r)}$. To generate an OAM signal with mode *l*, the radius of the ring can be determined by the following:

$$r = abs\left(\lambda.\frac{l}{2\pi}\right) \qquad (8)$$

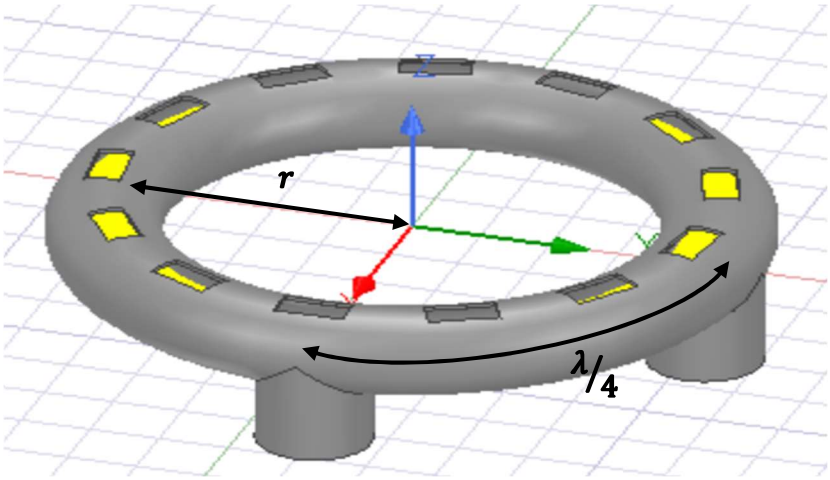

Figure 6.4 A slotted loop antenna used to generate an OAM signal

For a 5.64GHz signal, with λ=53mm, r is calculated as 8.5mm to generate a signal with an OAM mode of 1. The antenna used to generate a mode 1 signal, modelled in HFSS, is shown in fig. 6.5. The radii of the inner and outer conductors are a=2mm and b=3.3mm, respectively. The radius of the antenna to generate mode l=2 is calculated using (8) as r_1=16.9mm, and as 25.5mm for mode l=3. As the radius of the antenna increases, the distance between the slots increases; therefore, the number of slots may be likewise increased to obtain a more continuous waveform. The slots are cut with a 0.5 duty factor, and are each a length of 2mm. This means that individual loop antennas must be designed and modelled for each OAM mode. The polarity of the OAM modes can be reversed by changing the phase difference between the two ports from +90° to -90°.

The amplitude and phase pattern of the electric field generated by the antenna for l=1 is observed on a plane above the antenna in HFSS. The plots presented in fig. 6.5 show the donut-

shaped amplitude plot of a vortex beam, and the rotating spiral phase pattern characteristic of an OAM beam with a mode of 2.

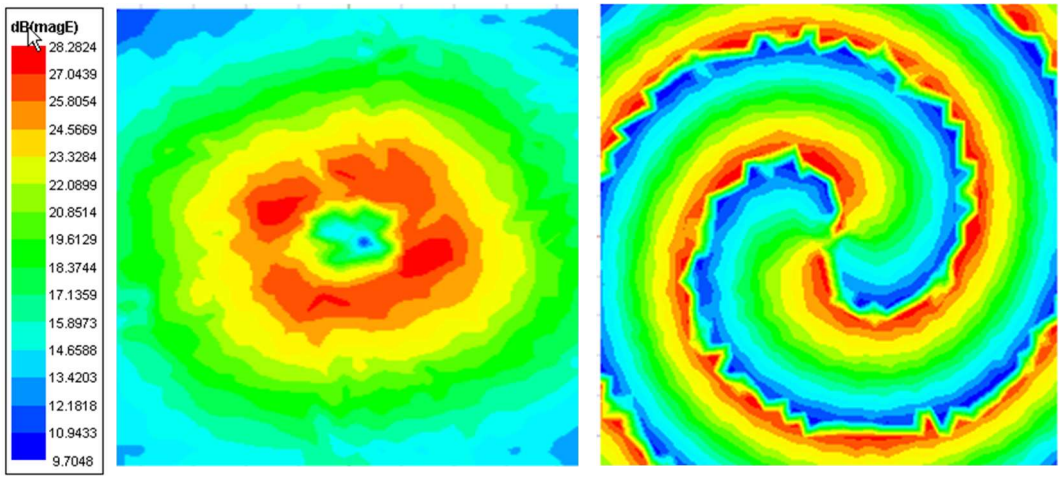

Figure 6.5 Amplitude and phase patterns of the electric field generated by the loop antenna with l=2 in HFSS

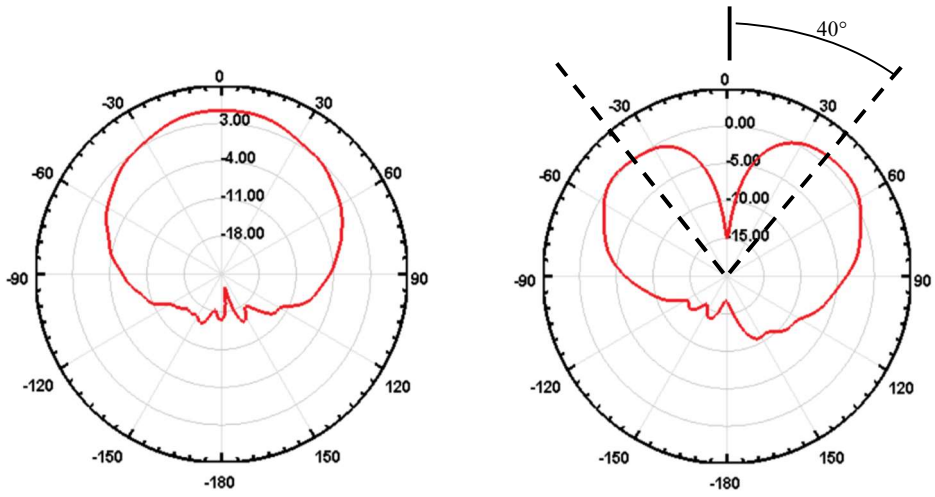

$l = 1$ $l = 2$

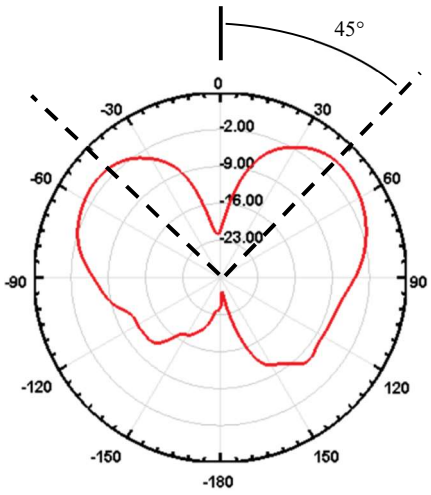
45°
0
30
60
90
120
150
-180
-120
-90
-60
-30
-2.00
-9.00
-16.00
-23.00

$l = 3$

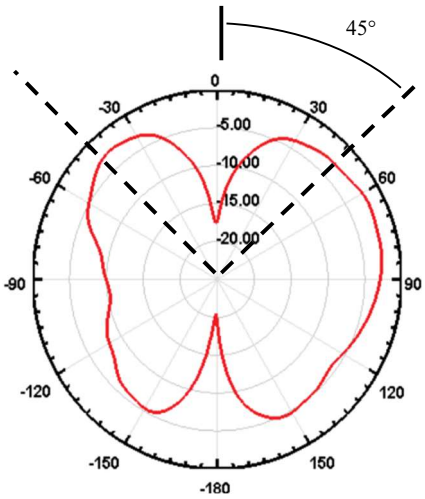
45°
0
30
60
90
120
150
-180
-120
-90
-60
-30
-5.00
-10.00
-15.00
-20.00

$l = 4$

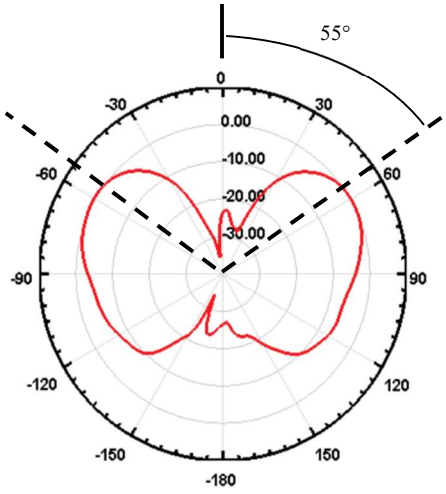
55°
0
30
60
90
120
150
-180
-120
-90
-60
-30
0.00
-10.00
-20.00
-30.00

$l = 5$

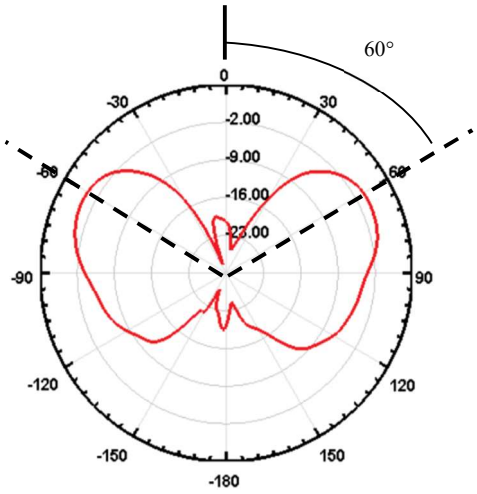
60°
0
30
60
90
120
150
-180
-120
-90
-30
-2.00
-9.00
-16.00
-23.00

$l = 6$

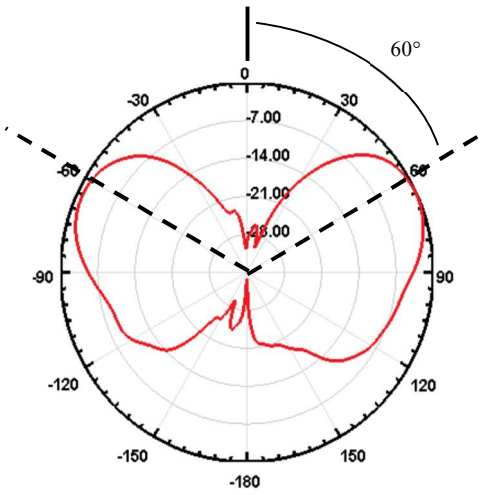

$l = 7$

Figure 6.6 Radiation patterns of antennas with OAM modes 1 to 7 in the φ=0 plane. The divergence angles of each radiation is marked.

The radiation patterns for the OAM antennas with modes ranging from 1 to 7 are also shown in fig. 6.6. What is most striking about the patterns is that the radiation pattern of mode 1 does not have a dip in the center. Presumably this null 0° is washed out by the diffraction of the two lobes. As was seen in section 6.1, the radiation generated by the loop antennas is a Bessel function. According to [78], the radiation pattern of mode 1 is not dipped in the center because the radiation is maximum in the axial direction when the order of the Bessel function is 1, as in the case of mode 1, and the radiation degrades as it travels. For higher order modes, the central dip increases as the mode number increases (-15dB for mode 2 and -28dB for mode 7), and the divergence angle also increases (40° for mode 2, and 60° for mode 7). Therefore, with this method of OAM generation, mode 1 is not a good choice, and will not be used for any of the studies included in this section. Further, it can be noted that the radiation patterns are not perfectly symmetrical and are particularly contorted on the right side. The reason for this is that

although the constant current is assumed around the loop antenna in theory, in practice, there is an inhomogeneous current distribution in the azimuthal direction around the loop [78] due to losses.

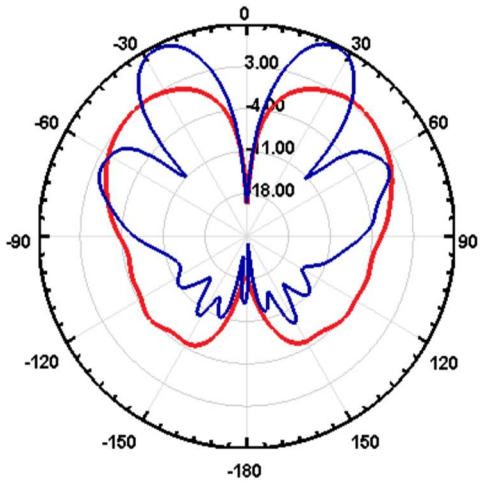

Figure 6.7 The radiation pattern of OAM mode 2 generated using the patch antenna array described in chapter 5 (blue), and that generated using loop antennas (red). Both patterns are plotted in the φ=0 plane.

Comparisons can be made between the OAM modes generated using patch array antennas, and those generated using loop antennas, by plotting the radiation pattern of both on the same figure. Fig. 6.7 shows the radiation pattern for OAM mode 2 generated by a phased array antenna (blue), and a loop antenna (red). One can observe that the radiation from the loop antennas does not feature side lobes. However, the gain of the radiation pattern generated by the loop antenna is lower (3dB) than the gain of the beam generated by the phased array (10dB). Moreover, the loop antenna has a higher back radiation (3dB) compared to the phased array (-11dB). The angle of divergence is also greater for the antenna generated by the loop antenna.

The differences in the radiation patterns will ultimately impact the way these antennas interact with other antennas.

6.2.2 Collimation Using Dish Antennas

It is important to note that the radiation patterns shown in fig. 6.5 also illustrate the angular direction in which the beams are propagating. OAM beams tend to diverge as they propagate, and the divergence is greater for higher order modes. As discussed in chapter 5, parabolic dish antennas may be employed to collimate the diverging OAM beams, to transmit them over long distances. The dish antennas can be redesigned for OAM loop antennas, as they were previously designed for array-based OAM antennas. From section 5.2, we learned that F/D is defined in terms of the curvature of the antenna by the following expression:

$$\frac{F}{D} = \frac{1}{4\tan\frac{\theta_o}{2}} \qquad (9)$$

Here, θ_o is the curvature of the dish , and the beam width is the angle (in degrees) on the radiation pattern of the dish, where the beam power has reduced to half of the maximum (i.e., 3dB). For a dish of diameter D with a beam of wavelength λ incident on it, the beam width is given by

$$Beam\ width\ \Psi = \frac{70\lambda}{D} \quad (10)$$

In section 5.2, it was concluded that it is more useful to design the dish for the highest order mode. Therefore, the dish will be designed for mode 7. From fig. 6.6, it can be observed that the beam divergence angle for mode 7 is 60°. If the array is placed at the focal point F of a

parabolic dish, then the beam radius after travelling a distance F is given by $d = F\tan 60 = 1.73F$. To ensure that the incident beam is not extending outside of the surface of the dish, the radius of the dish must be greater than the beam radius of the incident beam. Therefore, the dish diameter must satisfy $D > 2d = 3.46F$. And

$$\frac{F}{D} < 0.29 \qquad (11)$$

Taking the example of a parabolic dish with a beam width of Ψ =7.4, D can be calculated using (10) as D=0.5m. And from (4), selecting $\frac{F}{D} = 0.28$, the focal distance can be calculated as F=0.14m. Therefore, a dish with a diameter of D=0.5m, and a focal distance of F=0.14m, would be suitable for collimating mode 7.

Similarly, keeping the OAM antennas with other modes, at the same focal point F=0.14m, the diameter D of the dish can be calculated for each of these modes. For OAM mode l=2 of the outer array, the angle of divergence is 40 ° (see fig. 6.6). Therefore, the beam radius d, after traveling a horizontal distance F, is $d = F\tan 40 = 0.84F$. And to ensure that the beam does not diverge outside the dish, the diameter $D > 2d = 1.68F$. For F=0.14m (which was calculated for mode 7), D>0.23m. Therefore, a dish with a diameter of 0.5m would be suitable for use with a feed antenna generating mode 2. As all other modes have divergent angles ranging from 40° to 60°, the dish designed should also be suitable for use with them. Since mode 1 radiates mainly in the axial direction, its divergence will not be considered.

The loop antenna is used as a feed to the parabolic dish antenna designed, which will be called the East dish, $Dish_E$. The resulting collimated signal travels a distance to another parabolic dish called the West dish, $Dish_W$. $Dish_W$ converges the signal back to its original size, at its focal

point. A receiving loop antenna may be placed at the focal point of $Dish_W$ to collect the signal. The complete communication path is illustrated in fig. 6.8. To illustrate, the input feed is provided by a loop antenna of OAM mode 7. The signal received at the focal point of $Dish_W$, placed 1m away, is shown in fig. 6.9. The figure presents a distinct donut shape, signifying that the OAM signal has been successfully collimated and transmitted over a distance.

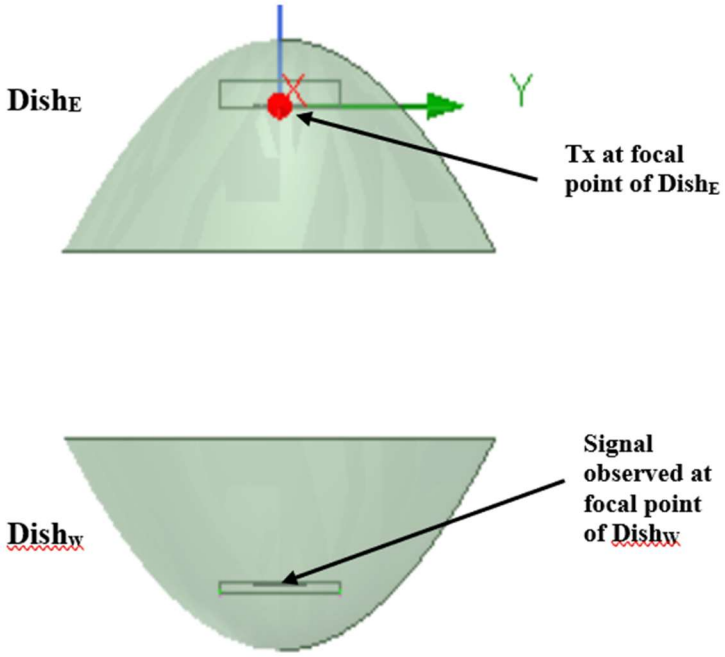

Figure 6.8 The signal transmitted by the East loop antenna is collimated by $Dish_E$ and transmitted to $Dish_W$ which converges it to its focal point. The transparency of the dish antennas has been increased to show the position of the feeding antenna and the observation point

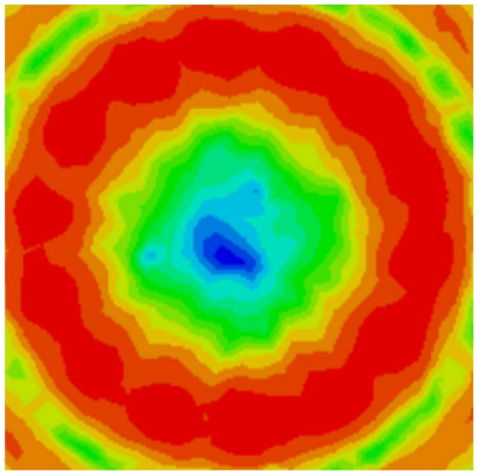

Figure 6.9 The signal received at the focal point of DishW when an OAM mode 7 is transmitted by the antenna on the East dish

A receiving loop antenna may be placed at the focal point of $Dish_W$ to create a complete communication path. A simulation is constructed in HFSS by creating the complete communication path and using a loop antenna with an OAM mode of 2 as the transmitter. The OAM modes of the receiver are varied from -7 to +7 (excluding mode 0, which cannot be generated with a loop antenna), and the power coupling between the transmitter and the receiver antennas is measured as $S12_{E\text{-}W}$. One may recall that the polarity of the OAM mode depends on the direction in which the phase of the signal increases while looking in the direction of propagation of the beam generated. In this case, the direction of propagation of both antennas is in the opposite direction.

The values of $S12_{E\text{-}W}$ are plotted in fig. 6.10, for each mode of the receiver. The plot demonstrates that the power coupling is highest (-73dB) when the receiver has the same OAM mode as the transmitter, i.e., mode l=+2. This is because matched OAM modes have the highest

coupling, and all non-matching OAM modes are orthogonal, as previously discussed. The coupling is lower than -80dB for all other receiver modes exhibiting lower coupling between non-matching modes. There is no remarkable trend identified in the variation of $S12_{E\text{-}W}$ values as the receiver mode changes. It should be noted, however, that the power of the received signal is also dependent on the distance between the East and West antennas, and therefore, the purpose of observing $S12_{E\text{-}W}$ is to determine the variation of the power coupling with the OAM mode at any fixed distance.

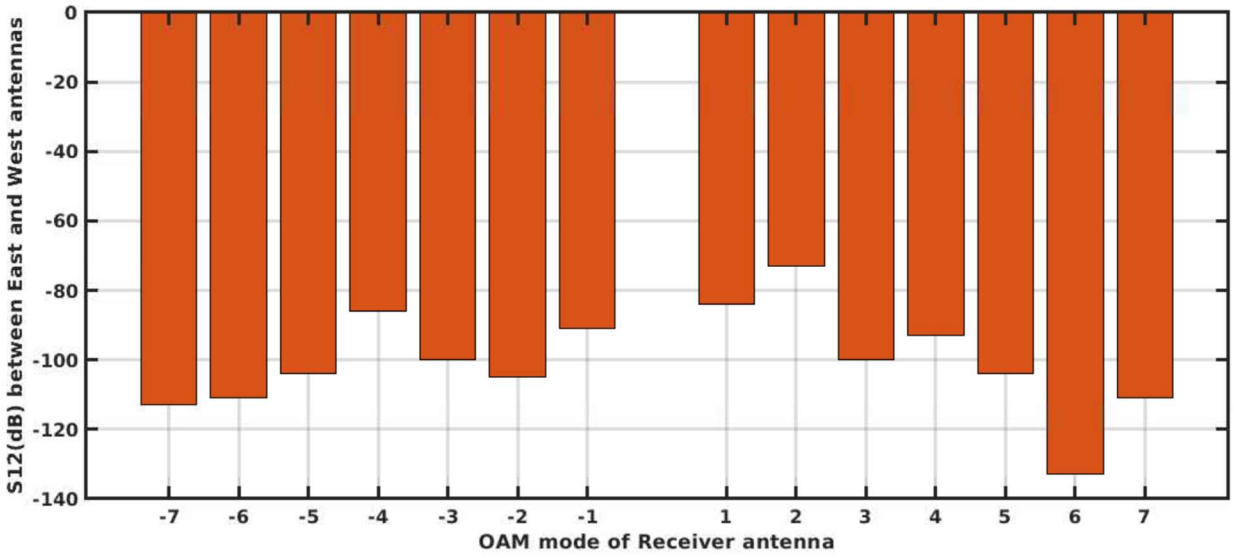

Figure 6.10 The power coupling $S12_{E\text{-}W}$ between the East and West antennas communicating over a distance, with the aid of parabolic dish antennas

A similar study was stimulated using patch array antennas, and was discussed in section 5.4. In this case, an OAM mode of 1 was used for the transmitter, and similar results were produced, with the highest coupling obtained for matching OAM modes. However, the $S12_{E\text{-}W}$ values were much higher in this case, with -21dB obtained for matching OAM modes, and less

than -42dB for non-matching modes. The lower coupling powers for loop antennas may be attributed to the lower gain of the loop antennas compared to phased array antennas, as was seen in fig. 6.7.

6.2.3 Nested Loop Design

Once it has been established that the loop antenna generates OAM, different antenna modes can be placed concentrically on a single plane to create a nested antenna design, as exemplified in fig. 6.11. For convenience, both loop antennas are placed at the origin, on the x-y plane. The inner loop is used as a transmitter, with the OAM mode fixed at l=2. By varying the radius of the loop and increasing the number of slots, the mode of the outer loop ranges from -7 to 7. In using this setup, it is not possible to determine the crosstalk that occurs when both the inner and outer antennas have the same modes, because loops with the same modes will have the same radius and cannot be placed concentrically. Similarly, it is not possible to generate a mode 0 using this method of OAM wave generation since a loop with a radius of 0 is not physically possible. For this reason, receiver modes of 2,-2, and 0 are excluded from the study.

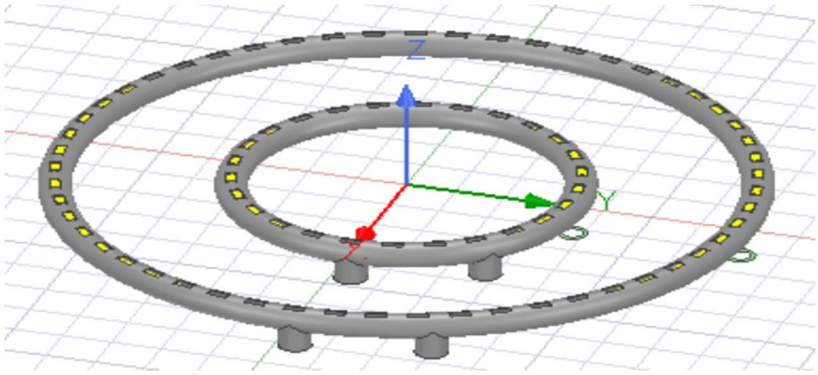

Figure 6.11 Loop antenna with mode 2 is used as a transmitter in the center, and the outer loop with mode 4 is used as a reciever. Both antennas are placed concentrically in a nested loop design

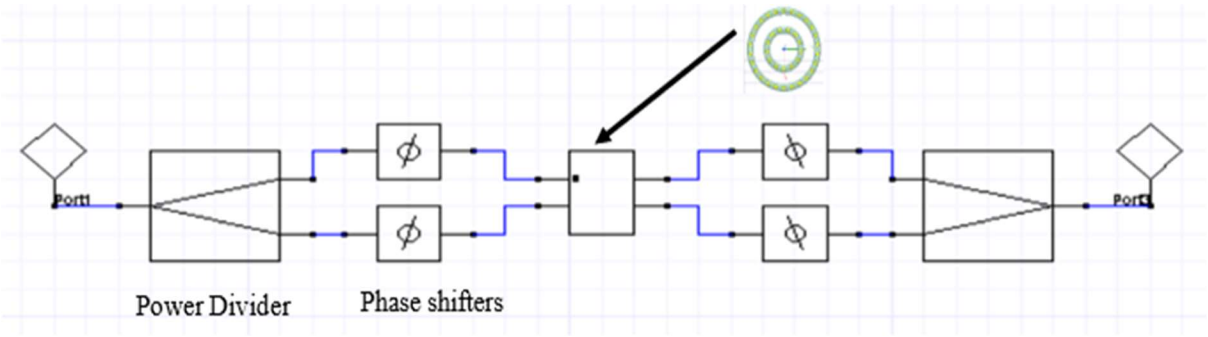

Figure 6.12 The schematic created in ANSYS Circuit consists of a power divider used for splitting the signal into 2 equal signals, each of which is then phase-shifted by the phase-shifters and connected to the ports in the loop antenna

A feeding network for the transmitter and receiver antennas is created in ANSYS Circuit, as shown in fig. 6.12. It consists of a two-way power divider/combiner that is used to split the signal sent to the transmitter ports, or combine the signal collected by the receiver ports. The signal in each branch undergoes a phase shift of 0 or 90°, which is created by the phase-shifters in the schematic. A component representing the HFSS model of the antennas' setup is dynamically linked to the HFSS file. The 2 pins on one side of the component representing the HFSS model are linked to the ports of the inner antenna, and the other 2 pins are linked to the outer receiver loop antenna.

The crosstalk coupling between the inner and outer loop was determined as $S12_{crosstalk}$ using ANSYS Circuit, for each mode of the receiver. In fig. 6.13, the values obtained for $S12_{crosstalk}$ are plotted against the receiver mode. The figure indicates a low crosstalk for all modes of the receiver array. The maximum crosstalk value of -89dB is obtained for mode l=-3.

All other crosstalk values are below this value. The crosstalk values, although existent, are insignificant, and are proof that OAM orthogonality can be used for crosstalk reduction. There is no remarkable trend seen in the crosstalk values. Although the crosstalk values for receiver mode l=+2 and l=-2 are not included, based on the results of section 6.2.2, the crosstalk value is expected to be maximum for receiver mode l=-2. The results of this study are in conformance with the mathematical derivation in section 6.1, which showed no crosstalk between non-matching OAM modes.

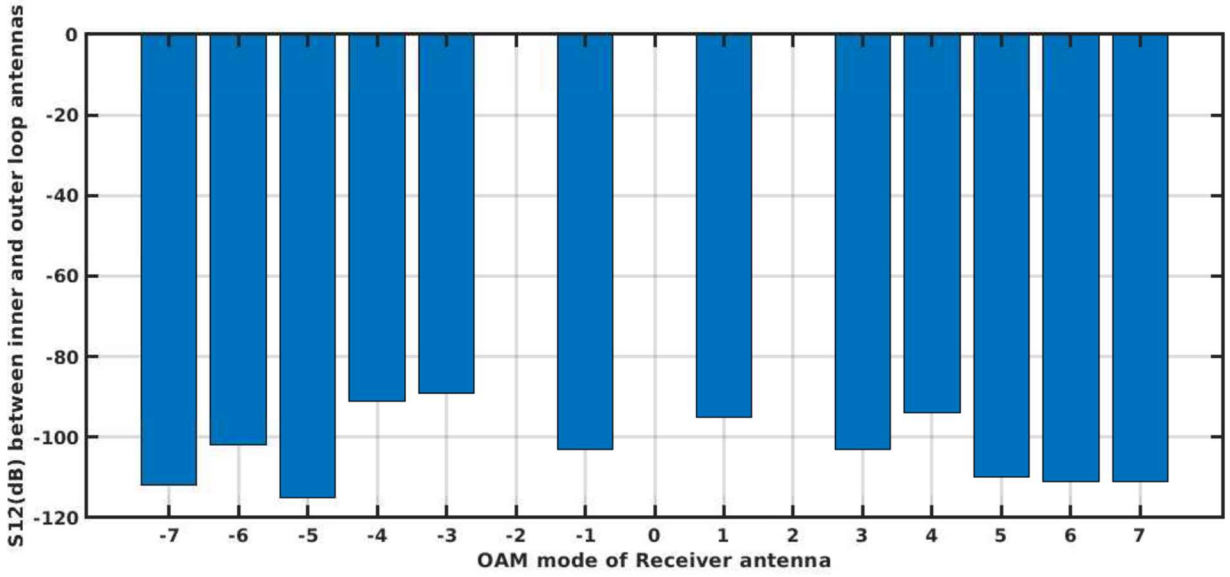

Figure 6.13 Crosstalk between the inner and outer loop antennas for varying modes of receiver OAM antennas, with the inner loop transmitting an OAM mode of 2

A similar study was carried out in section 5.3, but it used patch antenna arrays to create the nested OAM antenna design, instead of using the loop antennas to generate OAM. The

results for each are not based off identical data sets, though, because a mode of 0,2, and -2 could not be generated by the receiver loop antennas, and the maximum OAM mode that could be generated by the phased array antenna with the given number of array elements is 5. Moreover, the transmitter in section 5.3 was used to transmit an OAM mode l=1, whereas in this section, a transmitter with an OAM mode of l=+2 is used. However, an inspection of the available data indicates that the crosstalk that takes place between the inner and outer arrays is generally lower for loop-based OAM antennas for all non-matching modes. The much lower gain of the loop-based antenna, as illustrated in fig. 6.7, may be the reason for the lower crosstalk values, compared to phased array-based OAM antennas.

Another major difference in the crosstalk values of the two kinds of antennas is in their behavior with respect to odd and even modes. In the case of phased arrays, the crosstalk $S12_{local}$ is much higher for odd modes than for even modes. However, such a trend is not seen in the $S12_{local}$ values of the loop-based design. Since both methods generate OAM, it may be concluded that the difference in the crosstalk for odd and even modes in phased array-based design is not due to the nature of the signal generated, but is contributed by the physical structure of the antenna itself. Antenna elements in the phased arrays are in close proximity to one another and exhibit coupling between them. Additionally, the patch antennas of the outer array are also in the near field of the inner antenna, so there may be coupling between the inner and outer antenna elements, which could help explain the anomalous behavior of the odd and even modes. It should be kept in mind that, theoretically, the crosstalk between all non-matching OAM modes is essentially zero, as was seen in the derivation in section 6.1.

6.3 Conclusion

It has been observed theoretically and through numerical simulations that the OAM nature of waves affects the crosstalk between antennas placed in close proximity. This chapter serves as a conclusion to this dissertation, and presented a mathematical analysis of the crosstalk that occurs between two concentrically placed local OAM antennas. The first section of this chapter examined a wire loop carrying an electric current with a phase variance in the azimuth direction. The expressions for the field distribution near the loop were derived and graphed to show an OAM wave propagation. Further, the effect of the field on an outer wire loop was determined by deriving the voltage induced in the outer loop. It was proven, through mathematical analysis, that the coupling between the inner and outer OAM antennas occurs only if the antennas have the same mode, but different mode polarities. This isolation between the different modes of OAM is due to their orthogonality, and therefore, theoretically, and mathematically speaking, no voltage can be induced in the outer antenna by the crosstalk signal if the antennas do not satisfy $l=-l_1$.

Loop antennas were then modelled in HFSS using slotted coaxial waveguides. The antennas were designed to generate various OAM modes by changing their radii, and were placed concentrically to create a nested design. While the OAM mode of the inner antenna was fixed at $l=2$, the mode of the outer receiver antenna varied from -7 to +7 (excluding -2,+2 and 0), and the crosstalk between the two antennas could then be determined. Although it was not possible to determine the crosstalk when both antennas had the same OAM modes, it was shown that the crosstalk between non-matching modes of OAM is a low value (below -90dB) for all

modes of the receiver. Thus, the isolation of OAM modes due to their orthogonality is also demonstrated in the simulation.

CONCLUSION

OAM orthogonality has recently attracted much attention in wireless communication for its ability to transmit multiple signals simultaneously at the same frequency. Most of the research in this area, has been in this area has been primarily related to spatial multiplexing. This work shows that OAM orthogonality may be used to reduce the crosstalk between local transmitting and receiving antennas, thus unlike other studies that focus on the multiplexing of orthogonal OAM modes, this dissertation studied, for the first time, the crosstalk between OAM antennas, providing extra margin for full duplex link operation.

This study necessitated a design that allowed the OAM antennas to operate at a frequency of 5.64 GHz. The antennas were thus designed based on phased arrays of rectangular patches. The number of patches and the phase difference between adjacent patches was selected according to the number of the OAM mode to be generated. Chapter 2 provides a detailed description of the antenna design, fabrication and characterization process of the OAM antenna in practice and through simulations.

The OAM antenna was used in an experiment to determine the amount of crosstalk reduction that may be attributed to OAM orthogonality, and the variation that occurs with greater distance between adjacent OAM antennas. The experiment and results were described in chapter 4. It consisted of two OAM antennas connected to their feeding networks, which were comprised of phase-shifters and power-dividers. One of the antennas was configured to transmit an OAM mode of 1, and the other antenna was used as a receiver. The receiver mode varied between a mode of +1 and -1. The crosstalk values were noted in each case and the difference between the values is the differential crosstalk.

The differential crosstalk was obtained for various distances. The resulting data showed an oscillatory trend in differential crosstalk, with distance indicating the constructive and destructive addition of the signal phase that accompanies the receiver phase shifts as the signal phase shift changes with propagation distance. This is one of the major contributions of this study, as it provides insight into the nature of the crosstalk variation. The data may also help in selecting the optimal distance between the antennas for maximum isolation. The isolation measured through this experiment is based purely on OAM orthogonality, as all other factors, such as physical placement, are negated by the difference between the two crosstalk values. A maximum isolation of 2.6 dB was achieved experimentally.

Chapter 4 provided the details of the experiment simulated using HFSS. A moving average filter was used to remove the numerical noise from the weak crosstalk signals. The results of the simulated and practical experiments were compared and found to be in good agreement. An oscillatory trend was seen in the variation of differential crosstalk that occurs with distance, similar to that which was reported by the experimental results. The half-wavelength of the obtained sinusoid is approximately equal to the half-wavelength of a 5.64 GHz signal. A maximum isolation of 3.6 dB was achieved through simulations. Although the maximum isolation based on OAM orthogonality—obtained through both the experiment and simulation of the system—is only a small value, it confirms the hypothesis that OAM orthogonality does indeed create an added isolation. Moreover, it provides insight into how this effect is produced.

While chapter 3 and 4, proved the existence of, and highlighted the usefulness of OAM isolation due to OAM orthogonality at a theoretical level, chapter 5 proposes and analyses a practical antenna setup utilizing OAM orthogonality-based isolation that can be used in a full duplex system. The antenna setup is a nested antenna design, in which the OAM antennas are

placed concentrically. The radii of the patch antennas' inner and outer arrays are modified to accommodate both antennas on the same substrate. An OAM beam has the tendency to diverge as it propagates. Since OAM uses line of sight communication, the signal reaching the receiver must be the same as its original size. Therefore, to mitigate the problem of beam divergence, parabolic dish antennas are designed to collimate the signal. The collimated signal can travel over longer distances without diverging, and can be converged at the receiving end to its original transmitted size by an identical dish antenna. A receiver antenna is placed at the focal point of the receiving dish to collect the signal. An end-to-end communication link between the outer arrays of two antenna setups was simulated in HFSS. One of the antennas was configured to transmit an OAM mode of +1, whereas the other antenna was used as a receiver, with receiver modes ranging from -5 to +5. In all of the experiments simulated, the OAM mode of the antenna is determined with respect to the direction of propagation of the signal. In each case, the power and mode of the received signal was determined. The results showed that the received power is at its maximum when the receiver mode is the same as that of the transmitter, and a low power is received for other receiver modes, confirming the orthogonality of non-matching OAM modes.

Another study is simulated to determine the crosstalk power between the inner and outer antenna arrays in the nested antenna design. The inner array is used to transmit an OAM mode l=+1, and the mode of the receiver is varied between -5 to +5. The power coupling between the inner and outer arrays was observed as $S12_{local}$. The resulting data showed a high crosstalk value when the receiver had a mode of -1, and lower values for other modes. A maximum isolation of more than 60 dB was achieved using this antenna setup, with a receiver mode of -4. It was also observed that a higher power is received for odd modes compared to even modes. From this

finding, one can deduce that there is a higher orthogonality between even-odd OAM pairs. And a higher isolation can be achieved by selecting an even OAM mode for the receiver.

Chapter 6 concludes this dissertation, which provides the mathematical derivation and analysis of the crosstalk-induced voltage in a receiver antenna in the nested antenna design. The antennas were modelled by two wire loops placed concentrically. The current distribution in the inner loop was taken as $\boldsymbol{I} = I_o e^{-jl} \quad e^{-j\omega t}\widehat{\boldsymbol{a}_{\boldsymbol{\varphi}}}$, which means the magnitude of the current is constant and the phase is changing around the loop. Assuming the loop to be made up of a large number of infinitesimally small dipoles, the vector potential due to the loop at any observation point is calculated. The vector potential was then used to calculate the electric and magnetic fields generated by the inner loop. According to Faraday's law of Electromagnetic induction, voltage must be induced in a closed loop placed in the time-varying magnetic field of the inner loop. Because the outer loop in this experiment met the above conditions, the induced voltage was calculated using Faraday's law. It was found that the induced voltage is at its maximum when the inner and outer loop antennas have the same OAM modes, but is at zero when both loops have different OAM modes. This confirms the theory, which is the basis of this dissertation, that non-matching OAM modes are orthogonal, and there is no crosstalk between non-matching OAM modes.

The second half of chapter 6 introduces a coaxial waveguide antenna design for OAM generation to demonstrate the validity of the mathematical derivation. The waveguide antenna is designed in the form of a circular loop. Two ports provide the same input magnitude, but are 90° phase-shifted, to create a travelling wave effect. As the signal propagates in the loop, there is a phase-shift in the signal due to the distance of propagation. The radius of the loop is selected so as to create a total phase shift of $2\pi l$ in one complete revolution around the loop. Here l is the OAM

mode number. Therefore, to generate a mode 1 OAM beam, there is a 2π phase-shift in the signal, over one complete revolution around the loop. Slots are cuts in the outer layer of the coaxial waveguide antenna to allow the field to be radiated outwards.

As in chapter 5, for phased array-based OAM antennas, parabolic dish antennas are designed to collimate the beam generated by the loop antennas, and to transmit the beam over long distances from one antenna to another. In such a setup, the power coupling between a transmitting and receiving loop were studied at a distance of 1m. The resulting data showed that the power coupling between the same mode of OAM antennas is higher compared to non-matching modes, verifying the orthogonality of non-matching OAM modes.

The loop antennas were then placed concentrically in a nested design, to study the crosstalk between the two antennas for different modes of the outer receiver antenna. The inner antenna was used to transmit an OAM mode of 2. Since the radius of the loops determine the OAM mode generated, mode 0 could not be generated, as a loop with radius 0 is not physically possible. Also, receiver modes 2 and -2 could not be placed concentric to the transmitter antenna, which was also transmitting a mode of 2, as both antennas have the same radius. Therefore, modes 0, +2, and -2 were excluded from the study. The results showed crosstalk of less than -90dB between the inner and outer antennas, for all modes studied. This means there is a high isolation between non-matching OAM modes. Although matching OAM antenna modes could not be studied, it is expected that the crosstalk would be higher for receiver mode l=-2, as matching OAM modes are not orthogonal. The results of this study are in good agreement with the mathematical analysis in section 6.1. However, comparison with the results of the same study which was described in chapter 5, using phased array based OAM antenna shows that for the case of phased array a difference was seen in the crosstalk for odd and even OAM modes, which was not seen in the

results of loop based OAM antennas. This leads to the conclusion that the difference in behaviour with regard to odd and even OAM modes, shown by phased array-based OAM antennas, is supplied by the antenna structure, rather than by the OAM nature of the signal generated.

Future Directions

The primary aim of this dissertation is to promote the use of OAM orthogonality in full duplex systems as a direction for future research, and as a practical paradigm for full duplex systems. These initial findings are promising in both a theoretical and applied sense. Although the orthogonality between different OAM modes is a well-researched area, the role of orthogonality in creating isolation between local antennas was studied for the first time. The sinusoidal variation of the differential crosstalk with distance between the two antennas sheds light on the phase variation of the signal as it propagates over a distance, and the impact of this phase variation on the crosstalk value. This is an important finding and can lead to further research that may wish to take advantage of the phase variation that occurs with distance.

The dissertation proposed and analyzed a practical and compact nested antenna design, for use in full duplex systems. The design would also allow a single dish antenna to be used for both the inner and outer antennas. The high isolation between the inner and outer antennas, provides an added isolation between local antennas in a full duplex system, in addition to the isolation achieved through methods currently being used, such as digital signal processing and analog subtraction methods. A practical analysis and implementation of the full duplex system proposed would be a valuable contribution to the field of communication. The studies using the nested antennas design also suggest that high isolation may be achieved by other antenna topologies, as well. Moreover, since there is a difference observed in the results produced by

OAM antennas with different structures, it is proposed that more studies be carried out using other methods of OAM generation.

APPENDIX A

MATLAB code for Link Budget

This MATLAB code was used to plot the link budget shown in fig. 5.13. It consists of a plot of power of the signal as it propagates over a distance, which was calculated using equation (1) in chapter 5. The equation is evaluated in this code, and the power is plotted against distance. The code also plots the crosstalk value for receiver modes *l*=2 and *l*=3, by deducting the isolation due to OAM orthogonality and crosstalk coding methods (analog subtraction and digital signal processing) from the transmitter power leaking from the transmitter antenna to receiver antenna.

```
clear all
f=5.64*10^9;                % frequency of operation
lamb=(3*10^8)./f;
R=34*10^-3;
R=60*10^-3;                 % Radius of array
rr=R./lamb;

N=12;                        %number of patches
P1=(N.*4.*(pi.^2).*(rr.^2)).^2;       %initial power without the loss
                                      %term
p1=10.*log10(P1);

P2=(lamb./(4.*pi.*D)).^4;          %loss term
p2=10.*log10(P2);
LB=p1+p2+85;                  %power after losses (eq. from
                                 % paper)+transmit power
Pr1=LB(end)+30;                %received power at D=1000 + dish
antenna gain (30dB)
Pr1=cat(2,LB(end),Pr1);
figure
semilogx(D,LB,'blue','linewidth',4);   % plot link budget equation
 xlabel('D(m)','fontsize',12);
 ylabel('Pr(dBm)','fontsize',12);
grid on
 hold on

D=100;
P11=(N.*4.*(pi.^2).*(rr.^2)).^2;
p11=10.*log10(P1);
D=1:10:2000;
```

```
P22=(lamb./(4.*pi.*D)).^4;
p22=10.*log10(P22);
LB4=p11+p22+85;             %% link budget equation till D=100

semilogx(D,LB4,'blue','linewidth',4);  %%plot power equation till
                                       D=100
xlabel('D(m)','fontsize',12);
ylabel('Pr(dBm)','fontsize',12);
grid on
hold on
Pr2=LB4(end)+30;                %%add antenna gain (30dB) to the
                                      received power value at D=100
Pr2=cat(2,LB4(end),Pr2);
D=[2000,2000];
semilogx(D,Pr2,'blue','linewidth',4); %%to draw vertical line showing
                                %% power after adding dish gain at
                                %%D=100
hold on


P11=(N.*4.*(pi.^2).*(rr.^2)).^2;          %%Repeat for D till 300
p11=10.*log10(P1);
D=1:10:10000;

P22=(lamb./(4.*pi.*D)).^4;
p22=10.*log10(P22);
LB4=p11+p22+85;

semilogx(D,LB4,'blue','linewidth',4);
xlabel('D(m)','fontsize',12);
ylabel('Pr(dBm)','fontsize',12);
grid on
hold on
Pr2=LB4(end)+30
Pr2=cat(2,LB4(end),Pr2);
D=[10000,10000];
semilogx(D,Pr2,'blue','linewidth',4);
hold on

D=1:10:10000;

Pt=85-30;   %transmit power without gain
Pt1=Pt-60;       %%power for mode -2
Pt2=Pt1-90;        %% - crosstalk coding gain
 Ptg1=Pt-27;       %%power for mode 3
 Ptg2=Ptg1-90;     %% -after crosstalk coding gain for mode 3
D=[1,5];
P=[Pt,Pt];
semilogx(D,P,'red','linewidth',4);
hold on
```

```
grid on
xlim([1 10000]);
ylim([-150 80]);
yticks(-140:20:80);
xlabel('D(m)','fontsize',12);
 ylabel('Pr(dBm)','fontsize',12);
set(gca,'FontName','TimesNewRoman','FontWeight','bold','FontSize',12);
set(gca,'LineWidth',2);
set(gcf,'color','w');
xticks([1 10 100 1000 10000]);
D=[1,5,5,21];
P=[Pt,Pt,Pt1,Pt1];
semilogx(D,P,'red','linewidth',4);
Pg=[Pt,Pt,Ptg1,Ptg1];
semilogx(D,Pg,'green','linewidth',4);
hold on
D=[1,5,5,21,21];
P=[Pt,Pt,Pt1,Pt1,Pt2];
semilogx(D,P,'red','linewidth',4);
hold on
D=[1,4,4,20,20];
Pg=[Pt,Pt,Ptg1,Ptg1,Ptg2];
semilogx(D,Pg,'green','linewidth',4);
D=21:10:10000;
[r,c]=size(D)
 zz(1:c,1)=(Pt2);
 [r1,c1]=size(zz)
 semilogx(D,zz,'red','linewidth',4);
 hold on
D=21:10:10000;
[r,c]=size(D)
 zz(1:c,1)=(Ptg2);
 [r1,c1]=size(zz)
 semilogx(D,zz,'green','linewidth',4);
```

APPENDIX B
Power Coupling between Patch Antenna Arrays facing each other

The communication between two patch arrays facing each other, in the near field is investigated. When the distance between the OAM antennas is one wavelength, the OAM signal has not diverged significantly over this distance. Secondly, the phase shift in the signals due to propagation distance, would be zero over a distance λ. The outer array in the antenna system of fig. 5.1 can be used to transmit an OAM signal to a receiving outer array of an identical antenna system on the other end. The study of such an end-to-end communication link may be useful in understanding the working of the antenna arrays, and the behavior of crosstalk between the inner and outer arrays. The inner array would communicate similarly with the inner array on the other end, and is ignored in this investigation. Two quantities are measured from this setup:

i. Power of received signal

ii. Mode of received signal

Received power Measurement

In this part of the study, the mode of the receiver antenna is varied, and the received power is measured when an OAM mode l=+1 is transmitted. The experiment is simulated in HFSS, and the feeding networks are connected in ANSYS circuit as before. The antennae's structure and placement in HFSS are shown in fig. B.1. The schematic created in ANSYS Circuit is shown in fig. B.2.

The HFSS model of fig. B.1, is symbolized by a component in ANSYS circuit which is dynamically linked to the HFSS model. The outer arrays are connected to feeding networks. The phase shifters provide the required phase shift to the signals feeding each patch, to configure the desired OAM mode on the arrays. The S_{12} value between the transmitter and receiver ports is the power received and can be measured in ANSYS circuit. Keeping the transmitter mode fixed at

l=+1, the OAM mode of the receiver array is varied from *l*=-3 to *l*=+3. The S_{12} values are noted for each case.

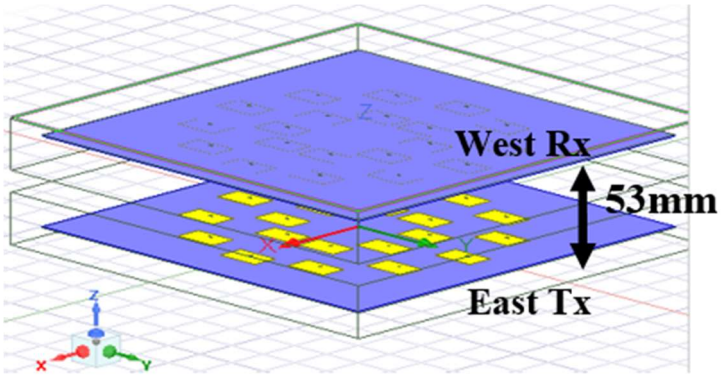

Figure B.1 End-to-end communication link created between the outer arrays of the two antenna systems placed 1λ apart

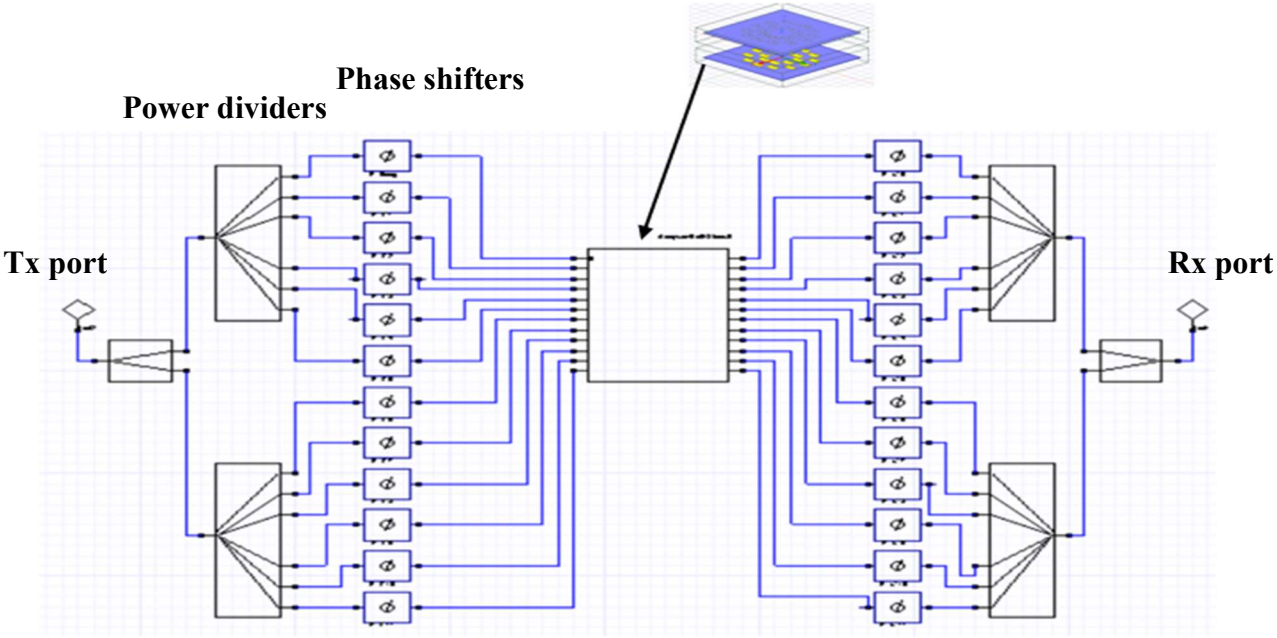

Figure B.2 Circuit schematic for measurement of S_{12} between East Tx and West Rx antennas

It is important to note that since both antennas are facing in the opposite directions, the direction of propagation is opposite for both. Therefore, the OAM mode polarity will be positive with respect to one direction of propagation, but negative with respect to the other. To avoid confusion, in these experiments, the OAM mode is defined with respect to the direction of propagation of the antenna of interest.

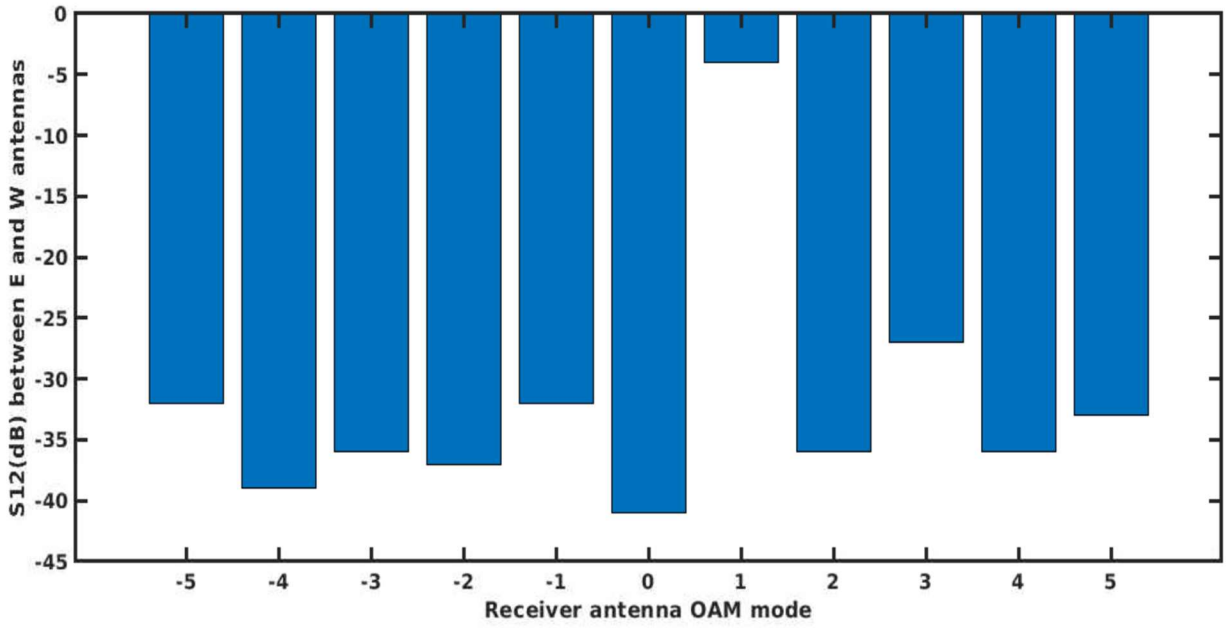

Figure B.3 S_{12} values for Tx mode l=+1 and varying modes of Rx antenna

The results for the S_{12} values are listed in table 1. The maximum signal power (-4.2 dB) is received by the antenna with the same OAM mode as the transmitter i.e., mode l=+1. This means that OAM antennas with the same mode can communicate effectively. For all other modes the value of S_{12} is lower due to the orthogonality of these modes with the transmitted mode l=+1. However, it must be noted that the power received by a receiver with mode l=+3 (i.e.

-27 dB) is higher than that for mode l=+2 (i.e. -37dB). This leads to the conclusion that the odd modes of the receiver have a higher reception of mode 1 signal compared to even modes. The lower crosstalk between the transmitted mode 1 and even receiver modes, leads to the prediction of a higher orthogonality between even-odd OAM mode pairs.

Mode of Received signal

The second part of the experiment is to observe the mode of the received signal in an end-to-end link between two outer arrays. It is expected that, when the transmitter and receiver arrays have the same OAM mode, an opposite phase delay is added to the signal received by each patch, causing the phase of the transmitted signal to add destructively to the phase added by the beam forming network of the receiver [57]. In the case where transmitter and receiver have opposite OAM modes (receiver has the same OAM mode, according to the change of propagation direction), the phase delays add constructively. Therefore, the mode of the received signal may be determined as l_{Tx}-l_{Rx}. A study is stimulated in HFSS to verify that the mode of the received signal is l_{Tx}-l_{Rx} when both antennas are facing each other.

The same HFSS model of fig. B.1 is used, and the feeding networks are created in ANSYS circuit as before. However, the output of the receiver antenna is fed into a separate patch array. The received signal being used to feed an antenna like this allows us to observe the field of the received signal. A component linked to the patch array is also placed in the schematic. The signal collected at the receiver patches is passed through the receiver phase shifts in ANSYS circuit, and fed to the patches of the patch array, as shown in the schematic of fig. B.4. Hence, the received signal is used as input to the patch array. The Electric field of the signal emitted by the array can then be calculated and observed in HFSS.

The East antenna is used to transmit an OAM mode *l*=+1. The West antenna is configured to receive OAM modes varied from *l*=-3 to *l*=+3, by altering the phase shift values in the receiver network. For each OAM mode of the receiver, the phase of the electric field of the signal generated by the patch array is observed in HFSS.

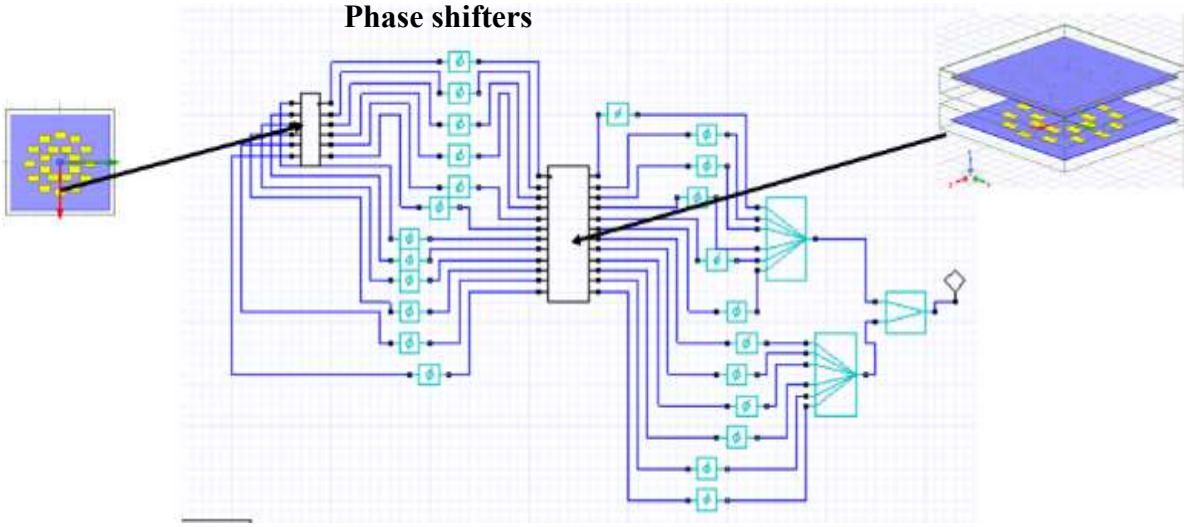

Figure B.4 Circuit schematic created to view the phase front of the received signal

Fig. B.5 shows the phase fronts of the waves resulting from an OAM mode *l*=+1 passing through the receiver antenna. The number of arms of the spiral in the phase front depict the mode number of the OAM. A transmitted mode *l*=+1, received by an OAM mode *l*=+1 receiver, results in a mode 0 (fig. B.5 (a)). This is in conformance with the results for received power. The receiver phase shifts cancel the transmitter phase shifts perfectly, which means both antennas can communicate effectively. However, all other modes are orthogonal to the transmitted mode 1. A receiving antenna with OAM mode *l*=-1, converts a transmitted *l*=+1 to mode 2, as can be seen by the 2 arms of the spiral in the phase front in fig. B.5 (b). Similarly, receiver mode l=+2 results in a mode 1 output (fig. B.5(c)), and a receiver mode *l*=-2 results in a mode 3 (fig. B.5(d)). The

results confirm the mode of the received signal may be determined as l_{Tx}-l_{Rx}, where the subtraction occurs due to the opposite direction of propagation of both antennas.

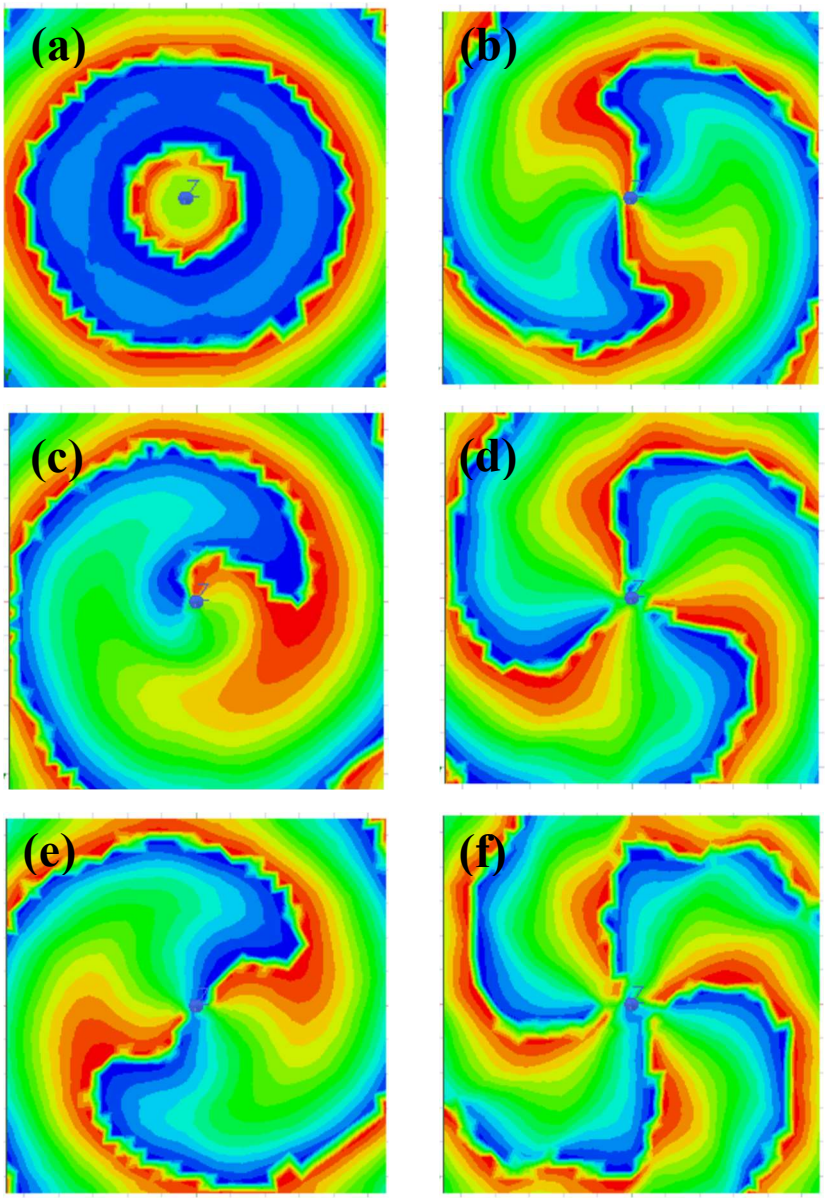

Figure B.5 The phase front of the signal received by the outer array when an OAM mode l=+1 is transmitted for receiver modes configured to (a) l=+1 (b) l=-1 (c) l=+2 (d) l=-2 (e) l=+3 (f) l=-3

APPENDIX C
Crosstalk between Nested Loops with Inner Loop mode *l*=1

In section 6.2.2 the nested loop design was studied. Since the OAM mode *l*=1 generated by a loop antenna does not have a distinct null in the center, an OAM mode *l*=1 was not used in the study to determine the crosstalk between the inner and outer loops. Instead an OAM mode *l*=2 was used as a transmitter. Here, the study is repeated by using an OAM mode *l*=1 as transmitter, to observe if it impacts the crosstalk values.

The setup of fig. 6.9 is recreated in HFSS, with the mode 2 loop antenna replaced with a mode 1 antenna. The schematic of fig. 6.10 is used. The mode of the inner transmitter is fixed at *l*=+1, and the mode of the outer receiver antenna is varied between -7 to +7. As discussed earlier, the mode *l*=0 can not be generated by the loop antenna as a loop of radius 0 is not physically possible. And modes *l*=+1 and *l*=-1 cannot be placed concentric to a mode *l*=1 transmitter antenna as they all have the same radius. Therefore, modes *l*=0, +1 and -1 are excluded from the study. The crosstalk signal $S12_{local}$ is determined for each receiver mode. The results are graphed for reference, in fig. C.1.

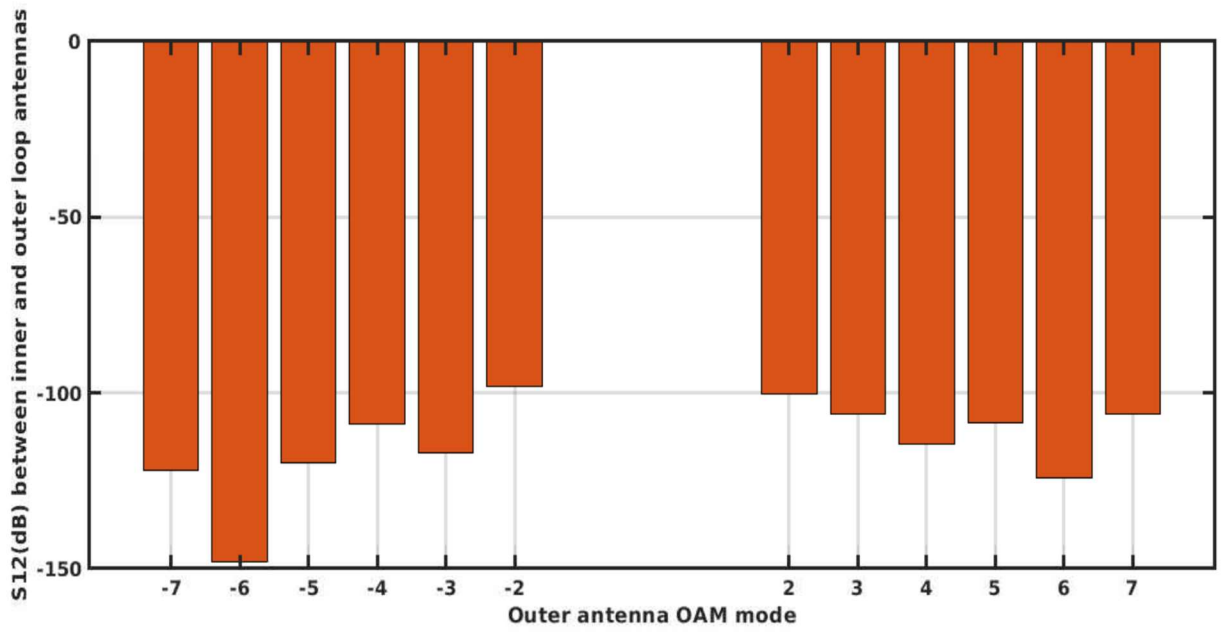

Figure C.1 Crosstalk between the inner and outer loop antennas for varying modes of receiver OAM antennas, with the inner loop transmitting an OAM mode of 1

BIBLIOGRAPHY

[1] Thomas Schwengler, in *Wireless and Cellular Communications*, Accessed: Jun. 29, 2022. [Online]. Available: https://morse.colorado.edu/~tlen5510/text/classwebch5.html

[2] J. I. Choi, M. Jain, K. Srinivasan, P. Levis, and S. Katti, "Achieving single channel, full duplex wireless communication," in *Proceedings of the sixteenth annual international conference on Mobile computing and networking - MobiCom '10*, Chicago, Illinois, USA, 2010, p. 1. doi: 10.1145/1859995.1859997.

[3] S. Gollakota and D. Katabi, "Zigzag decoding: combating hidden terminals in wireless networks," in *Proceedings of the ACM SIGCOMM 2008 conference on Data communication*, New York, NY, USA, Aug. 2008, pp. 159–170. doi: 10.1145/1402958.1402977.

[4] D. Halperin, T. Anderson, and D. Wetherall, "Taking the sting out of carrier sense: interference cancellation for wireless LANs," in *Proceedings of the 14th ACM international conference on Mobile computing and networking*, New York, NY, USA, Sep. 2008, pp. 339–350. doi: 10.1145/1409944.1409983.

[5] A. Sabharwal, P. Schniter, D. Guo, D. W. Bliss, S. Rangarajan, and R. Wichman, "In-Band Full-Duplex Wireless: Challenges and Opportunities," *IEEE J. Sel. Areas Commun.*, vol. 32, no. 9, pp. 1637–1652, Sep. 2014, doi: 10.1109/JSAC.2014.2330193.

[6] A. Gohil, H. Modi, and S. K. Patel, "5G technology of mobile communication: A survey," in *2013 International Conference on Intelligent Systems and Signal Processing (ISSP)*, Mar. 2013, pp. 288–292. doi: 10.1109/ISSP.2013.6526920.

[7] S. Katti, S. Gollakota, and D. Katabi, "Embracing Wireless Interference: Analog Network Coding," p. 12.

[8] B. Yang, Y. Dong, Z. Yu, and J. Zhou, "An RF self-interference cancellation circuit for the full-duplex wireless communications," in *2013 Proceedings of the International Symposium on Antennas & Propagation*, Oct. 2013, vol. 02, pp. 1048–1051.

[9] S. Member, E. Gebara, E. M. Tentzeris, S. Member, and J. Laskar, "Analysis and design of an interference canceller for collocated radios," *IEEE Trans. Microw. Theory Tech.*, vol. 53, pp. 3498–3508, 2005.

[10] B. Radunovic *et al.*, "Rethinking Indoor Wireless Mesh Design: Low Power, Low Frequency, Full-Duplex," in *2010 Fifth IEEE Workshop on Wireless Mesh Networks*, Jun. 2010, pp. 1–6. doi: 10.1109/WIMESH.2010.5507905.

[11] M. Duarte and A. Sabharwal, "Full-duplex wireless communications using off-the-shelf radios: Feasibility and first results," in *2010 Conference Record of the Forty Fourth Asilomar Conference on Signals, Systems and Computers*, Nov. 2010, pp. 1558–1562. doi: 10.1109/ACSSC.2010.5757799.

[12] M. Duarte *et al.*, "Design and Characterization of a Full-duplex Multi-antenna System for WiFi networks," *IEEE Trans. Veh. Technol.*, vol. 63, no. 3, pp. 1160–1177, Mar. 2014, doi: 10.1109/TVT.2013.2284712.

[13] Z. Zhang, X. Chai, K. Long, A. V. Vasilakos, and L. Hanzo, "Full duplex techniques for 5G networks: self-interference cancellation, protocol design, and relay selection," *IEEE Commun. Mag.*, vol. 5, no. 53, pp. 128–137, 2015, doi: 10.1109/MCOM.2015.7105651.

[14] P. Prasannakumar, M. Elmansouri, and D. Filipović, “Wideband dual-polarized bi-static simultaneous transmit and receive antenna system,” *2016 IEEE Int. Symp. Antennas Propag. APSURSI*, 2016, doi: 10.1109/APS.2016.7696634.
[15] M. Elmansouri, P. Valaleprasannakumar, E. Tianang, E. Etellisi, and D. Filipovic, “Single and dual-polarized wideband simultaneous transmit and receive antenna system,” in *2017 IEEE International Symposium on Antennas and Propagation & USNC/URSI National Radio Science Meeting*, Jul. 2017, pp. 1105–1106. doi: 10.1109/APUSNCURSINRSM.2017.8072595.
[16] E. Everett, A. Sahai, and A. Sabharwal, “Passive Self-Interference Suppression for Full-Duplex Infrastructure Nodes,” *IEEE Trans. Wirel. Commun.*, vol. 13, no. 2, pp. 680–694, Feb. 2014, doi: 10.1109/TWC.2013.010214.130226.
[17] E. Everett, A. Sahai, and A. Sabharwal, “Passive Self-Interference Suppression for Full-Duplex Infrastructure Nodes,” *IEEE Trans. Wirel. Commun.*, vol. 13, no. 2, pp. 680–694, Feb. 2014, doi: 10.1109/TWC.2013.010214.130226.
[18] M. A. Khojastepour, K. Sundaresan, S. Rangarajan, X. Zhang, and S. Barghi, “The case for antenna cancellation for scalable full-duplex wireless communications,” in *Proceedings of the 10th ACM Workshop on Hot Topics in Networks - HotNets ’11*, Cambridge, Massachusetts, 2011, pp. 1–6. doi: 10.1145/2070562.2070579.
[19] E. Aryafar, M. A. Khojastepour, K. Sundaresan, S. Rangarajan, and M. Chiang, “MIDU: enabling MIMO full duplex,” in *Proceedings of the 18th annual international conference on Mobile computing and networking - Mobicom ’12*, Istanbul, Turkey, 2012, p. 257. doi: 10.1145/2348543.2348576.
[20] H. Nawaz, A. Niazi, M. Basit, and M. Usman, “Single Layer, Differentially Driven, LHCP Antenna With Improved Isolation for Full Duplex Wireless Applications,” *IEEE Access*, vol. PP, pp. 1–1, Nov. 2019, doi: 10.1109/ACCESS.2019.2954947.
[21] “Multi-antenna near field cancellation duplexing for concurrent transmit and receive | IEEE Conference Publication | IEEE Xplore.” https://ieeexplore.ieee.org/document/5973400 (accessed Jul. 06, 2022).
[22] X. Wang, W. Che, W. Yang, W. Feng, and L. Gu, “Self-Interference Cancellation Antenna Using Auxiliary Port Reflection for Full-Duplex Application,” *IEEE Antennas Wirel. Propag. Lett.*, vol. 16, pp. 2873–2876, 2017, doi: 10.1109/LAWP.2017.2750698.
[23] Y. Chen, C. Ding, Y. Jia, and Y. Liu, “Antenna/Propagation Domain Self-Interference Cancellation (SIC) for In-Band Full-Duplex Wireless Communication Systems,” *Sensors*, vol. 22, no. 5, p. 1699, Feb. 2022, doi: 10.3390/s22051699.
[24] H. Nawaz and I. Tekin, “Three dual polarized 2.4GHz microstrip patch antennas for active antenna and in-band full duplex applications,” in *2016 16th Mediterranean Microwave Symposium (MMS)*, Nov. 2016, pp. 1–4. doi: 10.1109/MMS.2016.7803854.
[25] L. Sijia, J. Gao, X. Cao, Z. Zhang, and D. Zhang, “Broadband and High-Isolation Dual-Polarized Microstrip Antenna With Low Radar Cross Section,” *Antennas Wirel. Propag. Lett. IEEE*, vol. 13, pp. 1413–1416, Jan. 2014, doi: 10.1109/LAWP.2014.2339933.
[26] M. A. Islam and N. C. Karmakar, “A 4 × 4 dual polarized mm-wave ACMPA array for a universal mm-wave chipless RFID tag reader,” *IEEE Trans. Antennas Propag.*, vol. 63, no. 4, pp. 1633–1640, Apr. 2015, doi: 10.1109/TAP.2015.2398355.
[27] W. Wang, J. Wang, A. Liu, and Y. Tian, “A Novel Broadband and High-Isolation Dual-Polarized Microstrip Antenna Array Based on Quasi-Substrate Integrated Waveguide Technology,” *IEEE Trans. Antennas Propag.*, 2018, doi: 10.1109/TAP.2017.2777497.

[28] T. Dinc and H. Krishnaswamy, “A T/R antenna pair with polarization-based reconfigurable wideband self-interference cancellation for simultaneous transmit and receive,” in *2015 IEEE MTT-S International Microwave Symposium*, Phoenix, AZ, May 2015, pp. 1–4. doi: 10.1109/MWSYM.2015.7167135.
[29] Y.-M. Zhang and J.-L. Li, “Analyses and Full-Duplex Applications of Circularly Polarized OAM Arrays Using Sequentially Rotated Configuration,” *IEEE Trans. Antennas Propag.*, vol. 66, no. 12, pp. 7010–7020, Dec. 2018, doi: 10.1109/TAP.2018.2872169.
[30] J. Wang *et al.*, “Terabit free-space data transmission employing orbital angular momentum multiplexing,” Nature Photon,” *Nat. Photonics*, vol. 6, pp. 488–496, 2012.
[31] H. Huang *et al.*, “100 Tbit/s free-space data link enabled by three-dimensional multiplexing of orbital angular momentum, polarization, and wavelength,” *Opt. Lett.*, vol. 39, no. 2, pp. 197–200, Jan. 2014, doi: 10.1364/OL.39.000197.
[32] J. Wang and A. E. Willner, “Using Orbital Angular Momentum Modes for Optical Transmission,” in *Optical Fiber Communication Conference (2014), paper W4J.5*, Mar. 2014, p. W4J.5. doi: 10.1364/OFC.2014.W4J.5.
[33] Y. Yan *et al.*, “High-capacity millimetre-wave communications with orbital angular momentum multiplexing,” *Nat. Commun.*, vol. 5, no. 1, Art. no. 1, Sep. 2014, doi: 10.1038/ncomms5876.
[34] F. Tamburini, E. Mari, A. Sponselli, B. Thidé, A. Bianchini, and F. Romanato, “Encoding many channels on the same frequency through radio vorticity: first experimental test,” *New J. Phys.*, vol. 14, no. 3, p. 033001, Mar. 2012, doi: 10.1088/1367-2630/14/3/033001.
[35] X. Hui *et al.*, “Multiplexed Millimeter Wave Communication with Dual Orbital Angular Momentum (OAM) Mode Antennas,” *Sci. Rep.*, vol. 5, no. 1, Art. no. 1, May 2015, doi: 10.1038/srep10148.
[36] Z. Li, Y. Ohashi, and K. Kasai, “A dual-channel wireless communication system by multiplexing twisted radio wave,” in *2014 44th European Microwave Conference*, Oct. 2014, pp. 235–238. doi: 10.1109/EuMC.2014.6986413.
[37] Z. Zhang, Y. Yuan, J. Cang, H. Wu, and X. Zhang, “An Orbital Angular Momentum-Based In-Band Full-Duplex Communication System and Its Mode Selection,” *IEEE Commun. Lett.*, vol. 21, no. 5, pp. 1183–1186, May 2017, doi: 10.1109/LCOMM.2017.2660478.
[38] Solyman ASHRAFI (Plano, TX), “FULL DUPLEX USING OAM,” 20210344117, Nov. 04, 2021 Accessed: Jul. 09, 2022. [Online]. Available: https://patents.justia.com/patent/20210344117
[39] L. Allen, M. W. Beijersbergen, R. J. C. Spreeuw, and J. P. Woerdman, “Orbital angular momentum of light and the transformation of Laguerre-Gaussian laser modes,” *Phys. Rev. A*, vol. 45, no. 11, pp. 8185–8189, Jun. 1992, doi: 10.1103/PhysRevA.45.8185.
[40] M. W. Beijersbergen and L. Allen, “Astigmatic laser mode converters and transfer of orbital angular momentum,” *Opt. Commun.*, vol. 96, no. 1, p. 10, 1993.
[41] M. Krenn, M. Malik, M. Erhard, and A. Zeilinger, “Orbital angular momentum of photons and the entanglement of Laguerre–Gaussian modes,” *Philos. Trans. R. Soc. Math. Phys. Eng. Sci.*, vol. 375, no. 2087, p. 20150442, Feb. 2017, doi: 10.1098/rsta.2015.0442.
[42] O. C. Vicente and C. Caloz, “Bessel beams: a unified and extended perspective,” *Optica*, vol. 8, no. 4, pp. 451–457, Apr. 2021, doi: 10.1364/OPTICA.411887.
[43] A. Forbes, “Controlling light’s helicity at the source: orbital angular momentum states from lasers,” *Philos. Trans. R. Soc. Math. Phys. Eng. Sci.*, vol. 375, no. 2087, p. 20150436, Feb. 2017, doi: 10.1098/rsta.2015.0436.

[44] R. Oron, Y. Danziger, N. Davidson, A. A. Friesem, and E. Hasman, “Laser mode discrimination with intra-cavity spiral phase elements,” *Opt. Commun.*, vol. 169, no. 1–6, pp. 115–121, Oct. 1999, doi: 10.1016/S0030-4018(99)00389-2.
[45] A. M. Yao and M. J. Padgett, “Orbital angular momentum: origins, behavior and applications,” *Adv. Opt. Photonics*, vol. 3, no. 2, pp. 161–204, Jun. 2011, doi: 10.1364/AOP.3.000161.
[46] B. Thidé *et al.*, “Utilization of Photon Orbital Angular Momentum in the Low-Frequency Radio Domain,” *Phys. Rev. Lett.*, vol. 99, no. 8, p. 087701, Aug. 2007, doi: 10.1103/PhysRevLett.99.087701.
[47] M. J. Padgett, “Orbital angular momentum 25 years on [Invited],” *Opt. Express*, vol. 25, no. 10, pp. 11265–11274, May 2017, doi: 10.1364/OE.25.011265.
[48] S. M. Mohammadi *et al.*, “Orbital Angular Momentum in Radio—A System Study,” *IEEE Trans. Antennas Propag.*, vol. 58, no. 2, pp. 565–572, Feb. 2010, doi: 10.1109/TAP.2009.2037701.
[49] R. Chen, H. Zhou, M. Moretti, X. Wang, and J. Li, “Orbital Angular Momentum Waves: Generation, Detection, and Emerging Applications,” *IEEE Commun. Surv. Tutor.*, vol. 22, no. 2, pp. 840–868, 2020, doi: 10.1109/COMST.2019.2952453.
[50] I. V. Basistiy, V. Yu. Bazhenov, M. S. Soskin, and M. V. Vasnetsov, “Optics of light beams with screw dislocations,” *Opt. Commun.*, vol. 103, pp. 422–428, Dec. 1993, doi: 10.1016/0030-4018(93)90168-5.
[51] N. R. Heckenberg, R. McDuff, C. P. Smith, and A. G. White, “Generation of optical phase singularities by computer-generated holograms,” *Opt. Lett.*, vol. 17, no. 3, pp. 221–223, Feb. 1992, doi: 10.1364/OL.17.000221.
[52] M. Padgett and L. Allen, “Light with a twist in its tail,” *Contemp. Phys.*, vol. 41, no. 5, pp. 275–285, Sep. 2000, doi: 10.1080/001075100750012777.
[53] S. Franke-Arnold, L. Allen, and M. Padgett, “Advances in optical angular momentum,” *Laser Photonics Rev.*, vol. 2, no. 4, pp. 299–313, 2008, doi: 10.1002/lpor.200810007.
[54] A. Forbes, A. Dudley, and M. McLaren, “Creation and detection of optical modes with spatial light modulators,” *Adv. Opt. Photonics*, vol. 8, no. 2, pp. 200–227, Jun. 2016, doi: 10.1364/AOP.8.000200.
[55] Y. Yu *et al.*, “Design of PCF Supporting 86 OAM Modes with High Mode Quality and Low Nonlinear Coefficient,” *Photonics*, vol. 9, no. 4, Art. no. 4, Apr. 2022, doi: 10.3390/photonics9040266.
[56] F. Tamburini *et al.*, “Tripling the capacity of a point-to-point radio link by using electromagnetic vortices,” *Radio Sci.*, vol. 50, no. 6, pp. 501–508, 2015, doi: 10.1002/2015RS005662.
[57] F. Spinello *et al.*, “Experimental near field OAM-based communication with circular patch array,” *ArXiv150706889 Phys.*, Jul. 2015, Accessed: Apr. 13, 2022. [Online]. Available: http://arxiv.org/abs/1507.06889
[58] Y. Ren *et al.*, “Line-of-Sight Millimeter-Wave Communications Using Orbital Angular Momentum Multiplexing Combined With Conventional Spatial Multiplexing,” *IEEE Trans. Wirel. Commun.*, vol. 16, no. 5, pp. 3151–3161, May 2017, doi: 10.1109/TWC.2017.2675885.
[59] W. Cheng, W. Zhang, H. Jing, S. Gao, and H. Zhang, “Orbital Angular Momentum for Wireless Communications,” *ArXiv180407442 Eess*, Apr. 2018, Accessed: Apr. 21, 2022. [Online]. Available: http://arxiv.org/abs/1804.07442

[60] M. Jian, Y. Chen, and G. Yu, “Improving Multiple-User Capacity through Downlink NOMA in OAM Systems,” in *2021 IEEE International Conference on Communications Workshops (ICC Workshops)*, Jun. 2021, pp. 1–6. doi: 10.1109/ICCWorkshops50388.2021.9473665.
[61] H. Jing, W. Cheng, Z. Li, and H. Zhang, “Concentric UCAs based low-order radio vortex wireless communications with co-mode interference,” in *2017 IEEE/CIC International Conference on Communications in China (ICCC)*, Oct. 2017, pp. 1–6. doi: 10.1109/ICCChina.2017.8330361.
[62] J. Trinder, “Parabolic Reflector,” Jul. 28, 2005 Accessed: Apr. 24, 2022. [Online]. Available: https://patentscope.wipo.int/search/en/detail.jsf?docId=WO2005069443
[63] P. Schemmel, G. Pisano, and B. Maffei, “Modular spiral phase plate design for orbital angular momentum generation at millimetre wavelengths,” *Opt. Express*, vol. 22, no. 12, pp. 14712–14726, Jun. 2014, doi: 10.1364/OE.22.014712.
[64] X. Gao *et al.*, “Generating, multiplexing/demultiplexing and receiving the orbital angular momentum of radio frequency signals using an optical true time delay unit,” *J. Opt.*, vol. 15, p. 105401, Oct. 2013, doi: 10.1088/2040-8978/15/10/105401.
[65] F. E. Mahmouli and S. Walker, “Orbital angular momentum generation in a 60GHz wireless radio channel,” *2012 20th Telecommun. Forum TELFOR*, 2012, doi: 10.1109/TELFOR.2012.6419210.
[66] F. E. Mahmouli and S. D. Walker, “4-Gbps Uncompressed Video Transmission over a 60-GHz Orbital Angular Momentum Wireless Channel,” *IEEE Wirel. Commun. Lett.*, vol. 2, no. 2, pp. 223–226, Apr. 2013, doi: 10.1109/WCL.2013.012513.120686.
[67] N. Aflakian, T. P. LaFave, K. O. Kenneth, S. Ashrafi, and D. L. MacFarlane, “Design, fabrication, and demonstration of a dielectric vortex waveguide in the sub-terahertz region,” *Appl. Opt.*, vol. 56, no. 25, pp. 7123–7129, Sep. 2017, doi: 10.1364/AO.56.007123.
[68] Y. Yan *et al.*, “Demonstration of 8-mode 32-Gbit/s millimeter-wave free-space communication link using 4 orbital-angular-momentum modes on 2 polarizations,” in *2014 IEEE International Conference on Communications (ICC)*, Jun. 2014, pp. 4850–4855. doi: 10.1109/ICC.2014.6884088.
[69] H. Yao *et al.*, “Patch Antenna Array for the Generation of Millimeter-Wave Hermite–Gaussian Beams,” *IEEE Antennas Wirel. Propag. Lett.*, vol. 15, pp. 1947–1950, 2016, doi: 10.1109/LAWP.2016.2544808.
[70] S. Sakpal *et al.*, “Stability of Ince-Gaussian beams in elliptical core few-mode fibers,” *Opt. Lett.*, vol. 43, no. 11, pp. 2656–2659, Jun. 2018, doi: 10.1364/OL.43.002656.
[71] P.-Y. Feng, S.-W. Qu, and S. Yang, “OAM-Generating Transmitarray Antenna With Circular Phased Array Antenna Feed,” *IEEE Trans. Antennas Propag.*, vol. 68, no. 6, pp. 4540–4548, Jun. 2020, doi: 10.1109/TAP.2020.2972393.
[72] Q. Bai, A. Tennant, and B. Allen, “Experimental circular phased array for generating OAM radio beams,” *Electron. Lett.*, vol. 50, no. 20, pp. 1414–1415, 2014, doi: 10.1049/el.2014.2860.
[73] X. Bai, X. Liang, R. Jin, and J. Geng, “Generation of OAM radio waves with three polarizations using circular horn antenna array,” in *2015 9th European Conference on Antennas and Propagation (EuCAP)*, Apr. 2015, pp. 1–4.
[74] R. Gaffoglio, A. Cagliero, A. D. Vita, and B. Sacco, “OAM multiple transmission using uniform circular arrays: Numerical modeling and experimental verification with two digital

television signals," *Radio Sci.*, vol. 51, no. 6, pp. 645–658, 2016, doi: 10.1002/2015RS005862.
[75] L. Fang, "Study of Orbital Angular Momentum Radio Beams Based on Uniform Circular Antenna Array," Ph.D., The University of Texas at Dallas, United States -- Texas. Accessed: Oct. 11, 2022. [Online]. Available: https://www.proquest.com/docview/2474852154/abstract/772B703385B245ACPQ/1
[76] M. Lin, Y. Gao, P. Liu, and J. Liu, "Theoretical Analyses and Design of Circular Array to Generate Orbital Angular Momentum," *IEEE Trans. Antennas Propag.*, vol. PP, pp. 1–1, May 2017, doi: 10.1109/TAP.2017.2700160.
[77] S. Zheng, X. Hui, X. Jin, H. Chi, and X. Zhang, "Transmission Characteristics of a Twisted Radio Wave Based on Circular Traveling-Wave Antenna," *IEEE Trans. Antennas Propag.*, vol. 63, no. 4, pp. 1530–1536, Apr. 2015, doi: 10.1109/TAP.2015.2393885.
[78] F. Mao, T. Li, Y. Shao, M. Huang, and N. Dong, "Generation of radio beams carrying OAM basing on coaxial waveguide," in *2016 Progress in Electromagnetic Research Symposium (PIERS)*, Aug. 2016, pp. 1267–1270. doi: 10.1109/PIERS.2016.7734635.
[79] Constantine Balanis, "Microstrip antennas," in *Antenna Theory: Analysis and Design, 4th Edition | Wiley*, Accessed: Apr. 24, 2022. [Online]. Available: https://www.wiley.com/en-us/Antenna+Theory%3A+Analysis+and+Design%2C+4th+Edition-p-9781118642061
[80] I. J. Bahl and P. Bhartia, *Microstrip antennas*. Dedham,MA: Artech House, 1980.
[81] K. Carver and J. Mink, "Microstrip antenna technology," *IEEE Trans. Antennas Propag.*, vol. 29, no. 1, pp. 2–24, Jan. 1981, doi: 10.1109/TAP.1981.1142523.
[82] P. Katehi and N. Alexopoulos, "On the modeling of electromagnetically coupled microstrip antennas–The printed strip dipole," *IEEE Trans. Antennas Propag.*, vol. 32, no. 11, pp. 1179–1186, Nov. 1984, doi: 10.1109/TAP.1984.1143235.
[83] J. R. James, J. R. James, and P. S. Hall, *Handbook of Microstrip Antennas*. IET, 1989.
[84] D. M. Pozar, "Microstrip antennas," *Proc. IEEE*, vol. 80, no. 1, pp. 79–91, Jan. 1992, doi: 10.1109/5.119568.
[85] H. Oltman and D. Huebner, "Electromagnetically coupled microstrip dipoles," *IEEE Trans. Antennas Propag.*, vol. 29, no. 1, pp. 151–157, Jan. 1981, doi: 10.1109/TAP.1981.1142526.
[86] D. M. Pozar, "Microstrip antenna aperture-coupled to a microstripline," *Electron. Lett.*, vol. 21, no. 2, pp. 49–50, Jan. 1985.
[87] G. Gronau and I. Wolff, "Aperture-coupling of a rectangular microstrip resonator," *Electron. Lett.*, vol. 22, no. 10, pp. 554–556, May 1986, doi: 10.1049/el:19860378.
[88] M. V. Schneider, "Microstrip lines for microwave integrated circuits," *Bell Syst. Tech. J.*, vol. 48, no. 5, pp. 1421–1444, May 1969, doi: 10.1002/j.1538-7305.1969.tb04274.x.
[89] H. A. Wheeler, "Transmission-Line Properties of Parallel Strips Separated by a Dielectric Sheet," *IEEE Trans. Microw. Theory Tech.*, vol. 13, no. 2, pp. 172–185, Mar. 1965, doi: 10.1109/TMTT.1965.1125962.
[90] E. O. Hammerstad, "Equations for Microstrip Circuit Design," in *1975 5th European Microwave Conference*, Sep. 1975, pp. 268–272. doi: 10.1109/EUMA.1975.332206.
[91] O. Edfors and A. J. Johansson, "Is Orbital Angular Momentum (OAM) Based Radio Communication an Unexploited Area?," *IEEE Trans. Antennas Propag.*, vol. 60, no. 2, pp. 1126–1131, Feb. 2012, doi: 10.1109/TAP.2011.2173142.
[92] S. M. Mohammadi *et al.*, "Orbital angular momentum in radio: Measurement methods," *Radio Sci.*, vol. 45, no. 04, pp. 1–14, Aug. 2010, doi: 10.1029/2009RS004299.

[93] C. Deng, W. Chen, Z. Zhang, Y. Li, and Z. Feng, "Generation of OAM Radio Waves Using Circular Vivaldi Antenna Array," *Int. J. Antennas Propag.*, vol. 2013, pp. 1–7, 2013, doi: 10.1155/2013/847859.
[94] B. Kaufman, J. Lilleberg, and B. Aazhang, "Analog Baseband Cancellation for Full-Duplex: An Experiment Driven Analysis," Dec. 2013.
[95] V. Tapio, H. Alves, and M. Juntti, "Joint analog and digital self-interference cancellation and full-duplex system performance," in *2017 IEEE International Conference on Acoustics, Speech and Signal Processing (ICASSP)*, Mar. 2017, pp. 6553–6557. doi: 10.1109/ICASSP.2017.7953419.
[96] D. K. Nguyen, O. Pascal, J. Sokoloff, A. Chabory, B. Palacin, and N. Capet, "Antenna gain and link budget for waves carrying orbital angular momentum," *Radio Sci.*, vol. 50, no. 11, pp. 1165–1175, Nov. 2015, doi: 10.1002/2015RS005772.
[97] C. A. Balanis, *Antenna theory: analysis and design*, 3rd ed. Hoboken, NJ: John Wiley, 2005.
[98] Constantine A. Balanis, *Advanced Engineering Electromagnetics 2nd Ed. 2012*, 2nd ed. Wiley, 2012. Accessed: Oct. 22, 2022. [Online]. Available: http://archive.org/details/WileyAdvancedEngineeringElectromagnetics2ndEd.2012_201508
[99] W. Cheng, W. Zhang, H. Jing, S. Gao, and H. Zhang, "Orbital Angular Momentum for Wireless Communications," *IEEE Wirel. Commun.*, vol. 26, no. 1, pp. 100–107, Feb. 2019, doi: 10.1109/MWC.2017.1700370.
[100] H.-C. Kim and Y. H. Lee, "Hermite–Gaussian and Laguerre–Gaussian beams beyond the paraxial approximation," *Opt. Commun.*, vol. 169, no. 1, pp. 9–16, Oct. 1999, doi: 10.1016/S0030-4018(99)00411-3.
[101] A. E. Willner, K. Pang, H. Song, K. Zou, and H. Zhou, "Orbital angular momentum of light for communications," *Appl. Phys. Rev.*, vol. 8, no. 4, p. 041312, Dec. 2021, doi: 10.1063/5.0054885.
[102] A. E. Willner *et al.*, "Optical communications using orbital angular momentum beams," *Adv. Opt. Photonics*, vol. 7, no. 1, pp. 66–106, Mar. 2015, doi: 10.1364/AOP.7.000066.
[103] U. Tariq, H. Shahoei, G. Yang, and and D. L. MacFarlane, "Orbital Angular Momentum Orthogonality Based Crosstalk Reduction," *Prog. Electromagn. Res. Lett.*, vol. 98, pp. 17–24, 2021, doi: 10.2528/PIERL21022501.
[104] U. Tariq and D. L. Macfarlane, "Orbital Angular Momentum based Isolation in Concentrically placed Antennas," in *2022 IEEE Texas Symposium on Wireless and Microwave Circuits and Systems (WMCS)*, Apr. 2022, pp. 1–5. doi: 10.1109/WMCS55582.2022.9866144.
[105] Z. Zhang, S. Zheng, X. Jin, H. Chi, and X. Zhang, "Generation of Plane Spiral OAM Waves Using Traveling-Wave Circular Slot Antenna," *IEEE Antennas Wirel. Propag. Lett.*, vol. 16, pp. 8–11, 2017, doi: 10.1109/LAWP.2016.2552227.
[106] G. Fikioris, R. W. P. King, and T. T. Wu, "Novel surface-wave antenna," *IEE Proc. - Microw. Antennas Propag.*, vol. 143, no. 1, p. 1, 1996.